A Scanning Cavity Microscope

Matthias Mader

München 2018

A Scanning Cavity Microscope

Matthias Mader

Dissertation
an der Fakultät für Physik
der Ludwig-Maximilians-Universität
München

vorgelegt von
Matthias Mader
aus München

München, den 07.08.2018

Erstgutachter: Prof. Dr. Theodor W. Hänsch
Zweitgutachter: Prof. Dr. David Hunger
Tag der mündlichen Prüfung: 27.09.2018

Zusammenfassung

Nano ist überall! Nanoskalige Systeme sind allgegenwärtig, wie in farbigen Gläsern, neuartigen Solarzellen oder in Lebewesen. Für ein umfassendes Verständnis des Nanokosmos ist es unabdingbar, Nanoteilchen einzeln zu untersuchen, um einen tiefen und faszinierenden Einblick in eine Welt, die dem Betrachter auf dem ersten Blick verborgen ist, zu erlangen.

Optische Spektroskopie von einzelnen Nanosystemen liefert grundlegende Erkenntnisse von deren physikalischen und chemischen Eigenschaften. Quantitative Messungen von Extinktion und Dispersion an einzelnen Teilchen sind sehr schwierig, gleichzeitig sind solche Messungen sehr wünschenswert, da sich die Teilchen in Form, Größe oder Zusammensetzung unterscheiden können.

Diese Arbeit zeigt eine Methode zur gleichzeitigen Messung von Extinktion und Dispersion einzelner Nanopartikel mit Ortsauflösung. Tausende Umläufe von Licht in einem optischen Resonator verstärken die Wechselwirkung von Licht mit Materie und ermöglichen sehr sensitive Messungen an einzelnen Teilchen.

Die Mode eines Fabry-Pérot Resonators mit einer Finesse von bis zu 85 000 wird als Rastersonde verwendet, um die Extinktion von Nanoteilchen im Resonator zu bestimmen. Der Resonator ist aus einer mikrobearbeiteten und hochreflektiv beschichteten Glasfaser und einem makroskopischen Planspiegel, der gleichzeitig als Probenhalter dient, aufgebaut. Transversales Verschieben von Faser und Planspiegel zueinander liefert Ortsauflösung.

Zur Messung der Verschiebung der Resonanzfrequenz aufgrund eines Teilchens im Resonator werden Transversalmoden höherer Ordnung genutzt. Die Kombination beider Messungen erlaubt es, die komplexe Polarisierbarkeit, die die optischen Eigenschaften eines Nanoteilchens im Rayleigh-Grenzfall vollständig beschreibt, zu bestimmen.

In dieser Arbeit werden Extinktions-, Dispersions- und Polarisierbarkeitsmessungen an Goldnanoteilchen verschiedener Form und Größe gezeigt. Verglichen mit beugungsbegrenzter Mikrokopie liefert die Rasterresonatormikroskopie um mehr als 3200fach stärkere Messsignale, die zu einer Sensitivität für Extinktionsmessungen von $1.7\,\mathrm{nm}^2$ und zu Frequenzverschiebungen aufgrund von Dispersion von weniger als 200 MHz, was der Verschiebung durch eine Glaskugel mit einem Durchmesser von 31.6 nm entspricht, führen.

Darüber hinaus werden höhere Transversalmoden dazu verwendet, um die Ortsauflösung zu erhöhen. Durch die Kombination von Extinktionskarten, die mit der Grundmode und den darauf folgenden, höheren Transversalmoden aufgenommen wurden, ist eine signifikante Erhöhung der Ortsauflösung, gegebenenfalls sogar jenseits der Beugungsgrenze, möglich.

Das Rasterresonatormikroskop ist zunächst für die Untersuchung von Nanoteilchen in einer trockenen Umgebung konzipiert worden. Viele Nanosysteme,

darunter biologische Proben, zeigen ihre einzigartigen Eigenschaften jedoch erst in einer wässrigen Umgebung. Um den Untersuchungsbereich dorthin auszuweiten, wurde ein faserbasierter Resonator hoher Finesse mit einer mikrofluidischen Zelle kombiniert. Mit diesem System können nicht nur die Extinktion oder Dispersion von Teilchen gemessen, sondern auch Teilchen gefangen werden, um beispielsweise deren Reaktionsdynamik zu beobachten. In dieser Arbeit wird demonstriert, dass es möglich ist, einen Fabry-Pérot Resonator hoher Finesse in einer wässrigen Umgebung zu betreiben und es werden erste Messsignale von Teilchen, die den Resonator passieren, als auch vom Resonator gefangen werden, gezeigt.

Dieses System, das optische Detektion mit einem kontrollierten Flüssigkeitsstrom vereint, öffnet Möglichkeiten für neuartige Experimente mit einzelnen, unmarkierten Nanosystemen.

Abstract

Nano is everywhere! All around us, there are nanoscaled systems such as in coloured glass, novel solar cells or in living beings. For a detailed understanding of the nanocosmos, studying it at a single particle level is indispensable, leading to deep and intriguing insights into a world that is at a first glance hidden to the eye.

Optical spectroscopy of nanosystems at the single particle level provides profound insight into their physical and chemical properties. Retrieving quantitative signals for extinction as well as dispersion at this level is very challenging. At the same time it is desirable to investigate individual particles as they may vary in size, shape or composition.

This work presents a spatially resolved method for simultaneous extinction and dispersion measurements of single nanoparticles. Harnessing thousands of round trips of light within an optical microresonator, the interaction of light with the particle gets enhanced and very sensitive quantitative measurements become possible.

The cavity mode of a Fabry-Pérot cavity with a finesse up to 85 000 is used as a scanning probe to assess the extinction of nanoobjects placed into the cavity. The resonator consists of a micro-machined and high-reflectively coated end-facet of an optical fibre and a macroscopic plane mirror that serves as a sampleholder and that can be scanned transversally with respect to the fibre, allowing for spatially resolved measurements.

Higher order transverse cavity modes are exploited to retrieve the cavity's resonance frequency shift due to a particle inside. Combining both measurements allows to quantify the complex polarizability, which fully determines the particle's optical properties at the Rayleigh limit.

Extinction, dispersion and polarizability measurements of gold nanoparticles of various size and shape are presented in this work. Compared to diffraction limited microscopy, scanning cavity microscopy reaches a signal enhancement by a factor of more than 3200 resulting in a sensitivity for extinction of $1.7\,\mathrm{nm}^2$ and for frequency shifts due to dispersion below 200 MHz which corresponds to the shift due to a glass sphere with a diameter of 31.6 nm.

Furthermore, the higher order cavity modes are used to increase the spatial resolution of the scanning cavity microscope. By combining extinction maps taken with the fundamental and subsequent higher order modes, a significant increase in resolution potentially beyond the diffraction limit is demonstrated.

The scanning cavity microscope is dedicated to investigate nanoparticles in a dry environment. Many nanosystems, especially biological samples, show their unique properties only in an aqueous environment. To extend the field of investigation to these nanosystems a fibre-based high-finesse microcavity has been

combined with a microfluidic cell. This system would not only allow to measure the extinction or dispersion of a particle, but also to trap it to monitor e.g. reaction dynamics. In this work, the feasibility of bringing a high-finesse Fabry-Pérot cavity to an aqueous environment is demonstrated and first signals of trapping glass nanoparticles with the cavity mode as well as of particle transitions through the mode are shown.

This combined system of optical detection and fluid control opens the perspective for novel experiments with label-free individual nanosystems.

Contents

Chapter 1

Introduction

1.1 Nano is Everywhere

Nano-scaled systems play a major role in everyday life: Although the systems are at a first glance invisible, they determine how things look and feel or how life is organized. Already in ancient times, nanoscaled metal particles were used to colour glass [1, 2] and ceramics [3]. Today, specifically designed nanoparticles are used in a wide range of applications: The brilliance or special surface effects of paints rely on pigments at the nanoscale [4], many cosmetics contain nanoparticles to optimize their physical properties and to add special features like sun protection by titanium dioxide particles [5]. In medicine, especially in cancer treatment, nanoparticles play an important role in tumour marking, analysis, and therapy [6]. Novel light sources rely on nanoscaled semiconductor crystals [7], while nanostructuring of surfaces allows for novel solar cells [8] or even artificial photosynthesis devices [9].

Besides this variety of technical applications of nanoparticles, also life itself is based on nano-scaled systems: the basic building blocks of any living being, proteins, have a size at the nanometre scale [10].

Due to the omnipresence of nanosystems, it is mandatory to investigate them as they show intriguing physical, chemical, and biological properties. For many applications it is sufficient to study ensembles of nanoparticles, that are accessible by classical methods like microscopy or spectroscopy. Investigating ensembles of particles comes on the cost of averaging e.g. over the particle morphology or composition; or the ensemble survey might be affected by strongly size-dependent effects like Rayleigh scattering, which scales with the 6^{th} power of the particle radius. For not only observing effects occurring in nanosystems, but for understanding what really happens at the nanoscale, a survey of individual nanosystems is indispensable.

1.2 Detecting and Characterizing Nanosystems

To detect and to study single nanoparticles, a vast number of methods has been developed. These methods reach from diverse electron microscopy techniques over mechanical methods like atomic force microscopy to optical methods, where

the interaction of light with nanoparticles in the near field as well as in the far field is exploited.

This work introduces a novel method to detect and to characterize the optical properties of individual nanoparticles with spatial resolution by strongly enhancing the interaction of light and matter with an optical microresonator, in which the particle resides.

Besides this microresonator-based method for optically detecting non-fluorescing nanoparticles in the wide field, many other optical wide-field techniques dedicated to measure diverse features of particles came up over the last century. In the following, a selection of such methods is introduced to give a framework for the method of scanning cavity microscopy presented in this work.

Darkfield Microscopy

The first approach to detect and to observe individual nanoparticles was the ultramicroscope by Siedentopf and Zsigmondy: they investigated the scattered light of gold nanoparticles embedded in ruby-glass by illuminating the glass perpendicular to the optical axis of the microscope [11]. The sensitive detection of the scattered light by the nanoparticles gets possible, as background light from the illumination in the observation channel is strongly suppressed by the geometry of the illumination and observation optics. Till today, this method, further developed to darkfield and light sheet microscopy, is used to detect the light scattered by predominantly metallic nanoparticles. By spectroscopy of the scattered light it is possible to study effects influencing the plasmonic properties of individual particles [12].

Interference of Scattered Light

The direct observation of light scattered by nanoparticles with darkfield microscopy reaches its limit, when the scattering cross sections gets too small, as it is the case for very small particles (e.g. below 20 nm for gold nanospheres) or for particles with a refractive index close to that of the surrounding medium like biomolecules. The observed scattering signal I_{obs} can be enhanced by interfering the scattered field of the particle E_{scat} with the reflected probe light E_{ref}: $I_{obs} \propto |E_{obs}|^2 = |E_{ref} + E_{scat}|^2 = |E_{ref}|^2 + |E_{scat}|^2 + 2\,|E_{ref} E_{scat}|$. The last summand scales with the input field, and can be large although the amplitude of the scattered field might be low. Thus it is possible to enhance the scattering signal at the cost of high background (first summand). With this interference of scattered light method (iSCAT) it is possible to detect gold particles with a diameter of a few nanometres [13]. As this method is based on wide field microscopy, it allows to observe an extensive area with a single image.

The possible high photon flux in combination with ultrafast image detectors, advanced particle localisation and background subtraction techniques allows the tracking of individual proteins on a lipid membrane in real time with frame rates up to 500 kHz over minutes [14–16].

Extinction Measurements

While the scattering-based particle detection schemes offer very sensitive localisation of objects, in general they do not allow for a quantitative measurement

of the amount of light scattered by the particle and they cannot characterize its absorption.

Measuring the extinction of a particle, i.e. the amount of light taken out of a light beam by the particle by scattering and absorption, is in principle very simple: The particle is placed into to a sufficiently small beam of light and by comparing its power with and without the particle inside, the extinction can be deduced.

For nanoscaled objects this is more challenging: The particle is at least one order of magnitude smaller than the tightest focus achievable. Thus the change of transmitted power with and without particle in the focus is very small and advanced measurement schemes are required.

By comparing the probe and a reference beam on a balanced photodetector, it is even possible to detect single molecules with an extinction cross section of $0.1\,\mathrm{nm}^2$ [17, 18].

Modulating the position of a nanoparticle sample with respect to the probe light focus allows to reduce laser noise and fluctuations by lock-in detection. With this method, it is possible to do extinction spectroscopy on individual gold nanoparticles down to extinction cross sections of $50\,\mathrm{nm}^2$ while investigating e.g. the effects of the particle shape on the extinction properties [19–22].

In contrast to the methods above, where the extinction, i.e. scattering and absorption, of the particle has been measured, the pure absorption especially of metal nanoparticles can be accessed by photothermal absorption spectroscopy. Therefore, the (metal) particle is illuminated with light close to its plasmon resonance. The light gets absorbed by the particle and thus its local environment is heated up leading to a slight change of the refractive index. This index change can either be detected interferometrically with light far off the plasmon resonance [23] or by heterodyning exploiting frequency mixing at the particle that is heated with pulsed light [24, 25].

Signal Enhancement by Multiple Interactions

The sensitivity of optical methods to characterize nanoparticles can be further enhanced by increasing the number of interactions of the probe light with the particle. At each passage of the light at the sample, the amplitude or the phase of the light gets slightly modified. After several round trips, small changes can accumulate to detectable signals.

In principle, this approach is straight forward: The sample is placed in between two (semitransparent) mirrors and, if required, imaging optics such that the image of the particle is reflected onto itself when it circulates. This is possible in the wide field, for optical [26, 27] as well as for electron microscopy [28], where a whole microscope image cycles between two mirrors and thus its contrast gets enhanced at each passage at the sample. As it is challenging to reproduce a microscope image at each round trip, this approach is limited to a few round trips.

If instead of a wide field image only a single light mode circulates between two mirrors, the number of round trips can be easily increased. Such a cycling light mode is well known as an optical resonator or cavity. Thus the cavity mode can be used as a probe to measure the optical properties of a particle brought to it. Cavities allow to investigate the extinction of a particle, which takes light

out of the resonator, as well as its dispersion as the particle adds phase to the cycling light field and thus changes the resonance frequency of the cavity.

To get a high detection sensitivity, the mode has to be confined to a small volume. Using whispering gallery mode resonators, based on a light wave travelling on the circumference of a spherical, cylindrical or toroidal microstructure of an optically transparent material, this is routinely achieved. These resonators allow for ultra sensitive detection of the dispersion due to particles passing the mode [29, 30]. By local enhancement of the cavity field by plasmonic nanostructures, even individual ions get visible [31].

While whispering gallery mode resonators have very high quality factors ($\approx 10^{10}$), in general the particle detection relies on stochastically passing particles with uncontrolled position to the resonator mode in a liquid environment. To detect and investigate dry particles, attached to a surface, other resonator designs are required, that allow not only for particle detection but also localisation by scanning the cavity mode with respect to the sample.

Moving the resonator mode with respect to the sample in a well controlled way can be realized with a Fabry-Pérot resonator. This type of optical resonators is set up of two (curved) mirrors, with a light mode circulating in between. By moving one mirror with respect to the other, it becomes possible to overlap the mode with a particle that is placed onto one of the mirrors.

For high spatial resolution and sensitivity, the mode waist has to be as small as possible. This requires at least one mirror with a very small radius of curvature, smaller than achievable with conventional mirror polishing methods.

1.3 Scanning Cavity Microscopy

In this work, a scanning cavity setup is used, consisting of a plane mirror, at the same time serving as sample holder and a mirror applied to the micromachined endfacet of an optical fibre [32, 33]. These fibre-based mirrors have radii of curvature in the range of 10 µm to 100 µm, resulting in mode waists at the plane mirror of 1 µm to 3 µm. By scanning the fibre with respect to the plane mirror carrying the samples, the optical properties of the plane mirror surface and thus of the samples can be sampled pixelwise by the cavity mode. The basic concept of this scanning cavity microscopy scheme is illustrated in figure 1.1.

To achieve the best sensitivity taking advantage of a high number of round trips of the cavity mode, very high-reflective dielectric mirrors with ultra low losses are used in the experiments achieving a cavity finesse up to 85 000.

For measuring the optical properties of the particles on the mirror surface, the cavity is illuminated with a laser of fixed wavelength. As scanning the plane mirror with respect to the fibre over larger distances is incompatible to a setup, that is mechanically stable at the picometre-scale, which would be required to stay on resonance, the resonator length is scanned at each pixel to establish resonance.

Due to imperfect mode-matching of the fibre and cavity mode, it is easy to excite, besides the fundamental mode, several higher order transversal modes as shown in the transmission spectrum of a resonator depicted in figure 1.2. Due to a slight ellipticity of the micromirror fabricated to the fibre, the degeneracy of the higher order transverse modes is lifted and each mode again splits up into two orthogonally polarized and slightly frequency shifted resonances [34].

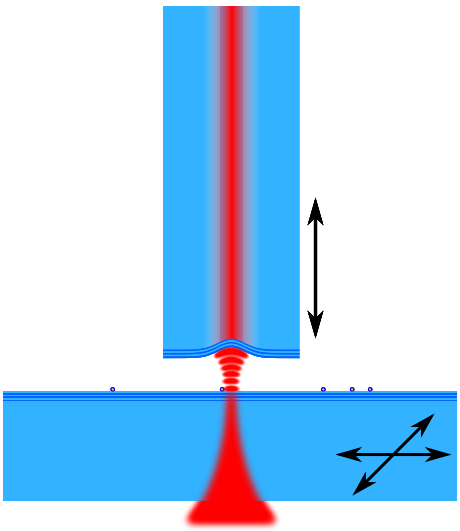

Figure 1.1: Principle of a scanning cavity microscope. The mode of a Fabry-Pérot cavity, consisting of a plane mirror and a curved mirror fabricated to the end-facet of an optical fibre, is used to characterize the optical properties of nanoparticles placed onto the plane mirror. By raster-scanning the plane mirror with respect to the fibre, spatial resolution is obtained.

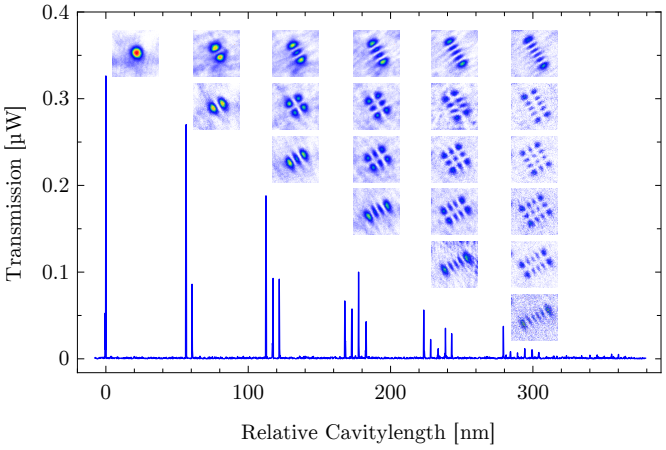

Figure 1.2: Transmission spectrum of a microcavity when scanning its length over a free spectral range. In addition to the transmission signal, the point spread functions of each mode are shown.

This splitting allows to address each mode individually and to do polarization dependent measurements.

From the amplitude and the linewidth of each resonance the cavity losses and thus the extinction due to a particle inside the resonator is determined.

By comparing the spacing between the 2nd order higher transverse modes, it is possible to measure the resonance frequency shift of the unstabilized cavity due to a particle inside and thus the dispersion of the particle: While the cloverleaf-shaped TEM11 mode has no electrical field in the centre, the other two have an electircal field there. If a particle is placed in the centre of the modes, the TEM11 mode stays unaffected while the outer two modes are shifted, allowing for a precise measurement of the dispersion due to the particle.

Repeating these measurement at each pixel of the field of interest leads to spatially resolved maps of extinction and dispersion of the mirror surface and thus of the samples plaed to it as shown in figure 1.3.

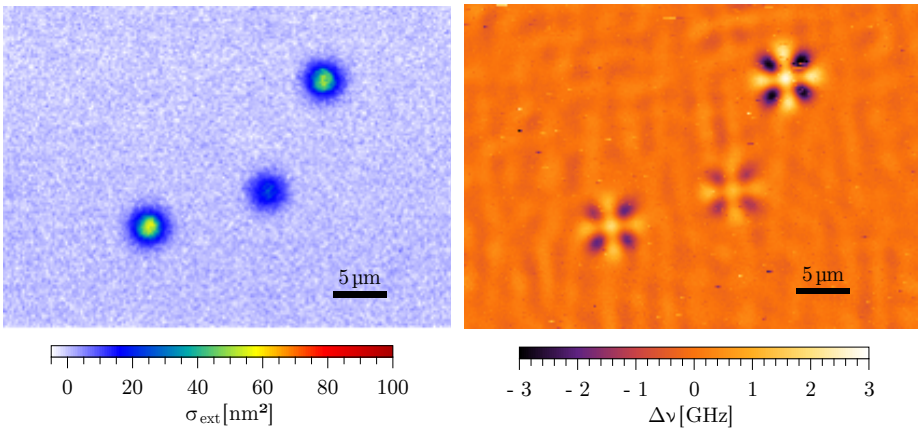

(a) Extinction. (b) Dispersion.

Figure 1.3: Extinction and dispersion map of a mirror carrying gold nanospheres with a diameter of 50 nm. The background of both measurements has been subtracted. Data points of the dispersion measurement, where the measurement failed have been replaced by the mean of the surrounding pixels.

Combining extinction maps taken with different transverse modes allows to increase the spatial resolution towards the diffraction limit. In special cases, it is even possible to overcome this limit. This method, inspired by mode squeezing in quantum mechanics, has been implemented for the first time in this work.

From the extinction- and the dispersion measurement, the polarizability of the nanoparticles under investigation can be calculated. This complex and in general tensorial quantity fully describes the optical properties of a particle in the Rayleigh limit.

To the knowledge of the author, no other experiment so far has been able to quantitatively measure the polarizability of individual nanoparticles. A comparable experiment to measure dispersion and extinction of gold particles , which was not dedicated to quantitative measurements, based on a scanning cavity with a mirror fabricated to the cantilever of an atomic force microscope has been realized nearly simultaneously to this work [35].

1.4 Scope of this Work

This work presents experiments enabling quantitative measurements of the polarizability of individual nanoparticles using a scanning cavity microscope for the first time. The capabilities of this microscope are demonstrated with measurements of the extinction, dispersion, birefringence and polarizability of various gold nanoparticles.

The work is organized in the following way:

Physical Principles At first, the basic physical concepts of the interaction of light with nanomatter, namely scattering and absorption are introduced. Especially effects of the particle size and its environment are discussed. Furthermore, the underlying physics of optical resonators is introduced. In a last step, this chapter unites particles and resonators and studies the effects of a particle on the resonator.

Setup Next, the setup of the scanning cavity microscope is introduced. The CO_2 laser-based fabrication of the fibre-based cavity mirrors is shown. The optical, mechanical and electronic setup is described. To control and coordinate the pixelwise measurement procedure, an advanced experiment control is required, which is introduced at the end of this chapter.

Measurements In this chapter, measurements using gold nanoparticles, including spheres of different diameter and rods, are shown. Gold particles have been used as a testbed to demonstrate the feasibility of quantitative measurements of extinction, polarization dependent extinction, and frequency shifts as well as dispersion resulting in the measurement of the polarizability of individual gold spheres. Furthermore, a novel scheme to enhance the spatial resolution in microscopy using a linear combination of higher order transverse cavity modes is demonstrated.

Towards an Underwater Cavity To investigate nanosystems in an aqueous environment, a proof of concept experiment joining a high-finesse optical microcavity and a microfluidic channel has been set up. This chapter shows the experimental approach as well as first measurements underlining the possibility of detecting and trapping individual glass nanospheres in water.

Chapter 2

Physical Principles of Cavity Microscopy

2.1 Absorption and Scattering of Light by Small Particles

The way we notice our environment by eye is shaped by scattering and absorption of light: Most of the colour impressions we get from the surrounding are caused by diverse absorption and scattering properties of different media. While e.g. the leafs of a tree scatter green light, which make them looking green and absorb red and blue light, which is used for photosynthesis, the trunk of a tree often looks dark brownish as it absorbs most of the incident light due to its rough surface.

Not only the look of macroscopic objects is determined by scattering and absorption of light, but also the optical properties of small objects with a size comparable or below the wavelength of light are predominately defined by scattering and absorption. Due to their small size, those particles often show very different optical properties than the corresponding bulk materials: for example gold particles strongly scatter green light thus colloidal solutions of them appear red in transmission in contrast to the golden shine of the bulk material.

To understand and describe these special properties of nanoparticles, investigated in this work using a scanning cavity microscope, the interaction of small particles with light is discussed in the following section.

Starting with very fundamental principles of light matter interaction, this work gives an overview of basic results of scattering theory. It introduces Rayleigh scattering for particles much smaller than the wavelength and Mie-scattering for arbitrarily sized spherical particles. It will end with various results of special cases relevant for this work like ellipsoidal particles or particles on surfaces and mirrors.

Especially the first part of the discussion will follow the comprehensive books by van de Hulst [36] and Quinten [37].

2.1.1 Scattering, Absorption, Extinction

When a beam of light hits an arbitrarily sized particle, it gets either scattered or absorbed. Both processes take light out of the beam and thus attenuate it. Absorption is related to an energy transfer transforming the photon energy to e.g. thermal energy. Elastic scattering redirects the light out of the incident beam without changing its wavelength. Inelastic scattering takes or adds a portion of the light's energy converting it to or from internal energy and changes the wavelength of the scattered light. Furthermore, the light can get absorbed and re-emitted, usually at a longer wavelengths, this process is called fluorescence. In the scope of this work, only elastic scattering and absorption play an important role and are discussed in the following.

Observing the attenuated light beam does not allow for distinguishing between both processes, absorption and scattering. Both effects together are called *extinction*.

$$Scattering + Absorption = Extinction \tag{2.1}$$

To quantify the strength of a scatterer or absorber, a cross section σ is assigned to the particle associating loss of light out of a beam with a geometric area in a beam, blocking a part of the light.

Sometimes the extinction- absorption- or scattering cross section is compared with the geometric cross section of the particle. The resulting quantity Q is called efficiency factor.

2.1.2 Scattering Theory

Light Matter Interaction

When matter is placed into an electrical field, the objects gets polarized as the atomic or molecular charges gets displaced by the electric force. The ease of displacement of the charges depends on the material, the internal structure and the geometry of the particle. The respective quantity to describe this is called polarizability. For arbitrarily shaped particles, the polarizability is a complex tensor. Section 2.1.3 gives relations between the polarizability tensor and material constants for differently shaped objects.

When the driving field oscillates, the induced polarization will follow the external field, act as a driven damped oscillator and emit electromagnetic waves. The properties of the oscillator are mainly determined by the internal electronic structure of the material. Resonances of the oscillator correspond to strong scattering and absorption at characteristic wavelengths. For metal particles, the effect of resonances of free electrons is shown in section 2.1.4.

If the wavelength of the driving field is much larger than the particle, the oscillating charges within the particle can be treated as a dipole, as Lord Rayleigh did, and as it will be discussed after an introduction of basic principals of scattering. When the particle gets larger, the dipole approximation does not hold any more, and a full description of the problem solving Maxwell's equations using a multipole expansion of the field inside the particle and of the radiated field is necessary. This was introduced by Gustav Mie and will be discussed subsequently. The transition between both approaches is investigated at the end of this chapter.

Basic Principals of Elastic Scattering

The following introduces a basic ansatz to describe elastic scattering and absorption.

For simplicity, the incoming wave is considered to be plane:

$$u_{in} = \mathrm{e}^{-ikz+i\omega t} \tag{2.2}$$

This wave gets disturbed by a scatterer, described by a complex amplitude function $S(\theta, \varphi)$ setting the amplitude and the phase of the outgoing wave. S can be decomposed to

$$S(\theta, \varphi) = s \cdot \mathrm{e}^{i\sigma} \tag{2.3}$$

with an amplitude function $s(\theta, \varphi)$ and a phase function $\sigma(\theta, \varphi)$.

Applying S to the incoming wave, leads to the scattered field. This field, at least at large distance from the scatterer, is a spherical wave, inversely proportional to the distance r.

$$u_{sc} = S(\theta, \varphi) \frac{\mathrm{e}^{-ikr+i\omega t}}{ikr} \tag{2.4}$$

The factor i is introduced for convenience, the faktor k makes S to be a pure number. Rewriting this equation in terms of the incoming wave leads to

$$u_{sc} = S(\theta, \varphi) \frac{\mathrm{e}^{-ikr+ikz}}{ikr} u_{in}. \tag{2.5}$$

To calculate the extinction cross section, the incoming and outgoing intensity in forward direction are compared. For forward scattering $\theta = 0$, thus $S(\theta, \varphi)$ simplifies to $S(0)$. Observing the outgoing field at points O close to the z-axis and far away from the particle, the coordinates of O simplifies to

$$r = z + \frac{x^2 + y^2}{2z}. \tag{2.6}$$

The total field at O can be written as

$$u_{in} + u_{sc} = u_{in} \left(1 + \frac{S(0)}{ikz}\right) \mathrm{e}^{-ik\left(x^2+y^2\right)/2z}. \tag{2.7}$$

showing that extinction is not only blocking intensity but represents a complex interference problem. Taking the absolute square leads to the intensity at a point O

$$\left|u_{in} + u_{sc}\right|^2 = 1 + \frac{2}{kz} \Re \left(1 + \frac{S(0)}{ikz}\right) \mathrm{e}^{-ik\left(x^2+y^2\right)/2z}. \tag{2.8}$$

Integration over all points O in an x-y plane far away from the scatterer gives a general expression for the extinction cross section.

$$\sigma_{ext} = \frac{4\pi}{k^2} \Re \left(S(0)\right) \tag{2.9}$$

Calculating the extinction of a certain particle is just a question of finding a proper function for S. This can be a quite challenging task and very often only approximate solutions can be found, as it will be shown in the next sections.

Rayleigh Scattering

For very small particles, the scattering problem can be solved by treating the particle as an induced dipole. The scattered light corresponds to the emitted field of the dipole, absorption comes with damping of the oscillator.

This solution, introduced by Lord Rayleigh, requires that the driving field can be approximated as constant within the particle. Thus the particle has to be small compared to the incident wavelength:

$$\left|\frac{n_{particle}}{n_{medium}}\right| \frac{2\pi r}{\lambda} \ll 1 \tag{2.10}$$

with the particle radius r, the wavelength λ, and the complex refractive index n of the particle and the surrounding medium. This relation is called Rayleigh approximation.

To get the scattering and absorption cross section of a particle, such a very small particle is placed into an electric field $\mathbf{E}$. The particle gets polarized and the respective dipole moment is given by

$$\mathbf{p} = \alpha \mathbf{E} \tag{2.11}$$

with the polarizability α. In general $\mathbf{E}$ and $\mathbf{p}$ are vectorial quantities and α is a tensor. For simplicity, the discussion will restricted to homogeneous particles where the tensor reduces to a scalar.

When the electrical field starts to oscillate with frequency ω, the dipole moment follows the field, as the particle is assumed to be very small compared the wavelength of the field so it can be seen as constant within the particle. The dipole moment is then

$$p(t) = \alpha(\omega) \mathrm{E}_0 \mathrm{e}^{i\omega t} \tag{2.12}$$

From electromagnetic theory it is well known, that such an oscillating dipole emits an electromagnetic wave. The emitted field at a point far away from the dipole is given by

$$E = \frac{k^2 p \sin\phi}{4\pi\epsilon_0 r} \mathrm{e}^{-ikr} \tag{2.13}$$

with wave vector k and ϕ the angle between the dipole axis and the position vector r.

The time-averaged radiated intensity of the dipole is given by

$$I = \frac{1}{2}\epsilon_0 c_0 \left|E(r)\right|^2 . \tag{2.14}$$

Integrating over a large sphere around the dipole leads to the total radiated power

$$W_{rad} = \int_0^{2\pi}\int_0^{\pi} \mathrm{d}\theta\, \mathrm{d}\phi\, r^2 \sin\phi\, \frac{1}{2}\epsilon_0 c_0 \left|\frac{k^2 p \sin\phi}{4\pi\epsilon_0 r}\mathrm{e}^{-ikr}\right|^2 \tag{2.15}$$

$$= \frac{c_0}{12\pi\epsilon_0} k^4 \left|p\right|^2 . \tag{2.16}$$

Normalization with the incident intensity $I_0 = \frac{1}{2}\epsilon_0 c_0 \left|E_0\right|^2$ gives the scattering cross section

$$\sigma_{sca} = \frac{k^4}{6\pi\epsilon_0^2} \left|\alpha\right|^2 . \tag{2.17}$$

The scattering cross section can be deduced from the general result for the extinction cross section (equation 2.9)[1]. For the scattering amplitude $S(0)$ in forward direction follows from equation 2.7 and equation 2.13

$$S(0) = ik^3\alpha. \tag{2.18}$$

Inserting $S(0)$ into equation 2.9 leads to

$$\sigma_{abs} = \frac{k}{\epsilon_0}\Im(\alpha). \tag{2.19}$$

In this result, scattering is missing, although the equation 2.9 should give the extinction cross section. This is due to the neglected radiation reaction of the dipole causing a small phase lag between p and $E(r)$ even for non-absorbing particles. The scattering cross section is calculated as shown above by integrating the scattered intensity over all directions. In order to give correct results for the extinction cross section, the scattering amplitude function is modified to

$$S(0) = ik^3\alpha + \frac{2}{3}k^6\alpha^2 \tag{2.20}$$

Mie Scattering

For larger particles, ($\left|\frac{n_{particle}}{n_{medium}}\right| \frac{2\pi r}{\lambda} \gtrsim 1$), where the assumption of a constant field inside the particle does not hold any more, the Mie theory for scattering takes over. In order to understand the varying colour of colloidal gold nanospheres of different size, Gustav Mie developed a rigorous theory for scattering of light at a sphere in 1908 [38]. Mie calculated the extinction and scattering of a massive sphere in an homogeneous medium by solving Maxwell's equations. To do so, he set up a boundary problem and did a multipole expansion of the emitted field of the sphere. A detailed discussion of the derivation of Mie scattering can be found by Mie himself [38] or e.g. by Born [39], van de Hulst [36] or Quinten [37] from where the results in this section are taken.

In the scope of this work, the most important result of Mie's scattering theory is the extinction- and scattering cross section of a spherical nanoparticle. The extinction cross section is given by

$$\sigma_{ext} = \frac{2\pi}{k_M^2}\sum_{n=1}^{\infty}(2n+1)\,\Re\left(a_n + b_n\right), \tag{2.21}$$

the scattering cross section is

$$\sigma_{sca} = \frac{2\pi}{k_M^2}\sum_{n=1}^{\infty}(2n+1)\left(|a_n|^2 + |b_n|^2\right), \tag{2.22}$$

with $k_M = {}^{2\pi n_m}/\lambda$ the wave vector of the surrounding medium and the scattering coefficients

$$a_n = \frac{\Psi_n(x)\Psi_n'(mx) - m\Psi_n'(x)\Psi_n(mx)}{\xi(x)\Psi_n'(mx) - m\xi_n'(x)\Psi_n(mx)} \tag{2.23}$$

$$b_n = \frac{m\Psi_n(x)\Psi_n'(mx) - \Psi_n'(x)\Psi_n(mx)}{m\xi_n(x)\Psi_n'(mx) - \xi_n'(x)\Psi_n(mx)}. \tag{2.24}$$

[1]The following derivation follows the shirt-sleeved approach by van de Hulst [36, p. 66]

The prime denotes a derivative with respect to the argument. The relative complex refractive index is $m = {}^{n_p}/_{n_m}$ using the sign convention $n = n + ik$, the Riccati-Bessel function $\Psi_n(x) = xj_n(x)$ and the Riccati-Hankel function of first kind $\xi_n(x) = xh_n^{(1)}$. x is a size parameter defined as $x = k_M r$ where r is the particle radius and k_M the wave vector in the surrounding medium.

The multipole expansion of the oscillating charges within the particle leads to a modified emission pattern. The scattering intensity perpendicular to the scattering plane spanned up by the wave vector of the incoming wave and the dipole axis is

$$i_{per}(\theta) = \left| \sum_{n=1}^{\infty} \frac{2n+1}{n(n+1)} \left[a_n \pi_n(\theta) + b_n \tau_n(\theta) \right] \right|^2 \tag{2.25}$$

and the scattering intensity parallel to the scattering plane

$$i_{par}(\theta) = \left| \sum_{n=1}^{\infty} \frac{2n+1}{n(n+1)} \left[a_n \tau_n(\theta) + b_n \pi_n(\theta) \right] \right|^2 \tag{2.26}$$

with $\tau_n(\theta) = \frac{\partial}{\partial \theta} P_{n1}$ and $\pi_n(\theta) = {}^{P_{n1}}/_{\sin\theta}$ where P_{n1} are associated Legendre polynomials for $m = 1$. Figure 2.1 shows examples for radiation pattern of differently sized gold nanospheres. While for very small particles a dipole-like pattern appears, for larger particles, the pattern gets more and more modified and the scattering in forward direction gets enhanced.

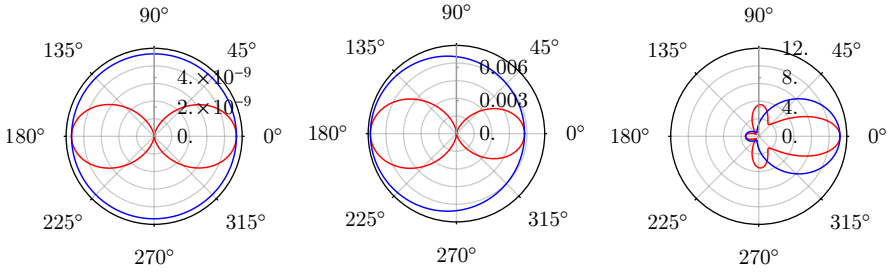

(a) 10 nm gold sphere. (b) 100 nm gold sphere. (c) 500 nm gold sphere.

Figure 2.1: Scattering intensities of gold spheres with different diameters parallel (blue) and perpendicular (red) to the incoming wave in dependence of the angle. The incoming wave with a wavelength of 780 nm propagates from left to right.

The infinite sums in the formulas for the cross sections are not very handy for numerical calculations. The following expressions give a rule of thumb for the required number n_{max} of summands using the size parameter $x = k_M R$ with the particle radius R.

$$n_{max} = \begin{cases} \text{integer}\left(x + 4\,x^{\frac{1}{3}} + 1\right) & x \leq 8 \\ \text{integer}\left(x + 4.05\,x^{\frac{1}{3}} + 2\right) & 8 < x < 4200 \\ \text{integer}\left(x + 4\,x^{\frac{1}{3}} + 2\right) & 4200 \leq x \end{cases} \tag{2.27}$$

From Rayleigh-scattering to Mie-scattering

The central assumption behind Rayleigh's treatment of the scattering problem is a uniform electrical driving field inside the particle such that it behaves like a point dipole. For particles of finite size, this assumption breaks down. At the same time, the Rayleigh approach gives much more handy results than the complete solution by Mie. In particular, Rayleigh gives compact analytical solutions even for non-spherical particles. So it is worth to investigate, up to which particle size the Rayleigh solution gives a good approximation to the results of Mie scattering.

A common threshold for the particle size for which Rayleigh scattering gives good results is

$$\left|\frac{n_p(\lambda)}{n_m(\lambda)}\right| \frac{2\pi\, r_p}{\lambda} \ll 1 \tag{2.28}$$

with $n_p(\lambda)$ the complex refractive index of a particle of radius r_p and $n_m\lambda$ the complex refrective index of the surrounding medium. Figure 2.2 shows a comparison between scattering and extinction cross sections for gold spheres at a wavelength of 780 nm calculated either with Rayleigh- or Mie formalism. The indicated Rayleigh criterion for the particle size shows, that for particles smaller than this radius, Rayleigh scattering gives good results while for larger particles a substantial error is made.

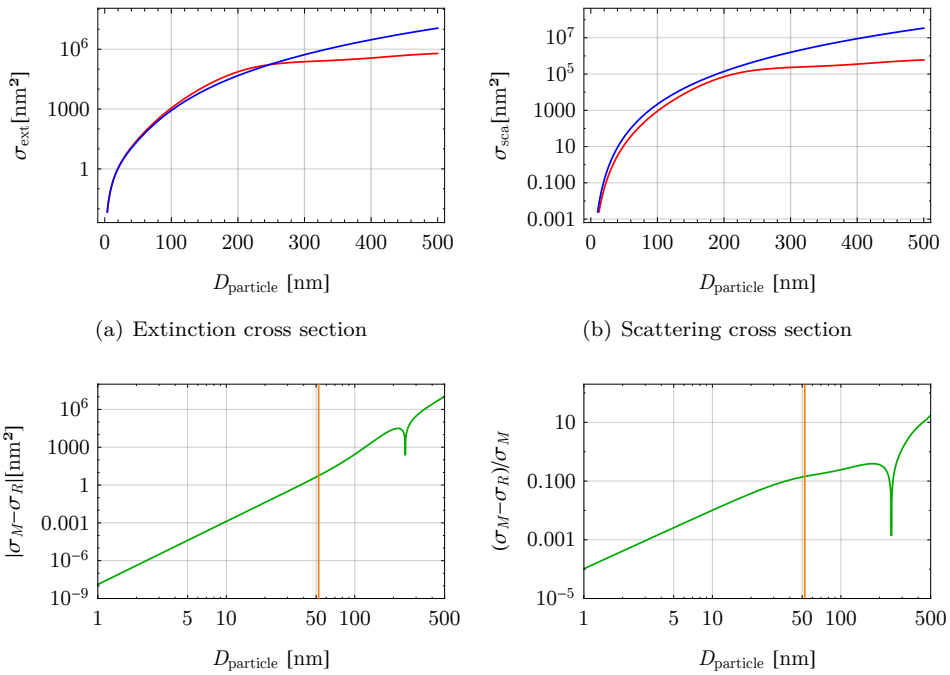

(a) Extinction cross section

(b) Scattering cross section

(c) Absolute difference of extinction cross sections

(d) Relative difference of extinction cross sections

Figure 2.2: Comparison of the results of Mie- (red) and Rayleigh (blue) scattering. The Rayleigh criterion for the particle size is indicated by an orange line.

2.1.3 Polarizabilty Tensor

The polarizability relates the geometry of the particle, its internal structure and its material to a complex tensorial quantity. This tensor sets, as discussed above, the optical properties of the object, which are in general not isotropic. For differently polarized light, the particle shows different optical properties. This leads to effects like birefringence or polarization dependent absorption due to the particle.

Only for homogeneous spheroids, an analytic description of the tensor exists. For all other structures, approximations or numerical descriptions are necessary [37, 40, 41].

As nanospheres and ellipsoids play a central role within this work, the results for the polarizability tensor are given in the following:

The elements α_i of the polarizability tensor of a homogeneous spheroidal particle are given by

$$\alpha_i = \epsilon_0 V_p \frac{\epsilon_3 - \epsilon_1}{\epsilon_1 + L_i\,(\epsilon_3 - \epsilon_1)} \tag{2.29}$$

with the spheroid volume $V_p = {}^{4\pi}/_{3}\, a_1 a_2 a_3$ with half axes a_1, a_2 and a_3, the geometry factors L_i, obeying the condition $L_1 + L_2 + L_3 = 1$ and relative dielectric numbers of the surrounding medium ϵ_1 and the particle ϵ_3 (see figure 2.6).

Spheres For homogeneous spheres, all three elements of the tensor are equal, the geometry factor $L_i = {}^{1}/_{3}$. The polarizability is then

$$\alpha = 4\pi r^3 \epsilon_0 \frac{\epsilon_3 - \epsilon_1}{\epsilon_3 + 2\epsilon_1} \tag{2.30}$$

Ellipsoids For ellipsoids with arbitrary half axis a_1, a_2 and a_3, the geometry factor can by calculated by

$$L_j = \int_0^\infty \mathrm{d}s \frac{a_1 a_2 a_3}{2(s + a_j^2)\sqrt{(s + a_1^2)(s + a_2^2)(s + a_3^2)}} \tag{2.31}$$

For special geometries, the geometry factor can be simplified and given analytically. The values for L_2 and L_3 follow from symmetry and the condition $L_1 + L_2 + L_3 = 1$.

Prolate Spheroids $a_1 > a_2$, $a_2 = a_3$

$$L_1 = \frac{1 - e^2}{e^2}\left(-1 + \frac{1}{2e}\ln\frac{1+e}{1-e}\right) \tag{2.32}$$

with $e^2 = 1 - ({}^{a_2^2}/_{a_1^2})$.

Oblate Spheroids $a_1 < a_2$, $a_2 = a_3$

$$L_1 = \frac{1 + f^2}{f^2}\left(1 - \frac{1}{f}\arctan f\right) \tag{2.33}$$

with $f^2 = ({}^{a_2^2}/_{a_1^2}) - 1$

Flat elliptical disks $a_1 \ll a_2$ and $a_1 \ll a_3$

$$L_1 = 1,\ L_2 = L_3 = 0 \tag{2.34}$$

Long elliptical cylinders $a_1 \gg a_2$ and $a_1 \gg a_3$

$$L_1 = 0,\ L_2 = \frac{c}{b+c},\ L_3 = \frac{b}{b+c} \tag{2.35}$$

2.1.4 Metal Nanoparticles

In the the scope of this work, mostly gold nanoparticles are used. Compared to *general* nanoparticle, discussed so far, metal particles show very characteristic properties important for the following discussions on the influence of the particle's environment and the particle size.

The electrical and thus the optical properties of metals can be described by the Drude model [42] and its extensions by Sommerfeld. A comprehensive introduction can be found in any solid state physics text book, like that by Ashcroft and Mermin [43]. Drude assumes a mobile electron gas, the conduction electrons, and fixed ions.

When a metal is exposed to an oscillating electrical field, the free conduction electrons follow the field while feeling a restoring force due to the fixed ions and a damping force due to scattering. This damped harmonic oscillator is a major contribution to the dielectric function of the metal [37]

$$\epsilon(\omega) = 1 - \underbrace{\frac{\omega_P^2}{\omega^2 + i\omega\gamma_{fe}}}_{\text{Free electrons}} + \underbrace{\sum_j \frac{\omega_{P,j}^2}{\omega_j^2 - \omega^2 - i\omega\gamma}}_{\text{Contributions of further oscillators}} \tag{2.36}$$

with plasma frequency $\omega_P^2 = \frac{Ne_0^2}{Vm_{eff}\epsilon_0}$ and damping constant $\gamma_{fe} = 1/\tau$.

At metallic surfaces or small metal particles, the oscillating polarisation of the electron gas with respect to the ions is called *surface plasmon polariton*. For its n^{th}resonance frequency ω_n at small particles (quasi static approximation) follows from the Mie coefficients (equations 2.24) as a resonance condition

$$\epsilon(\omega) = \frac{n+1}{n}\epsilon_1. \tag{2.37}$$

Together with the Drude part of equation 2.36 this leads to

$$\omega_n = \frac{\omega_P}{\sqrt{1 + \frac{n+1}{n}\epsilon_1}} \tag{2.38}$$

where n indicates the order of the resonance and ϵ_1 is the dielectric function of the surrounding medium [37]. The width Γ of the so called plasmon resonance is

$$\Gamma = \frac{2\Im[\epsilon(\omega)]}{\sqrt{\left(\frac{\partial\Re[\epsilon(\omega)]}{\partial\omega}\right) + \left(\frac{\partial\Im[\epsilon(\omega)]}{\partial\omega}\right)}} \tag{2.39}$$

taken at the plasmon resonance $\omega = \omega_n$ [44].

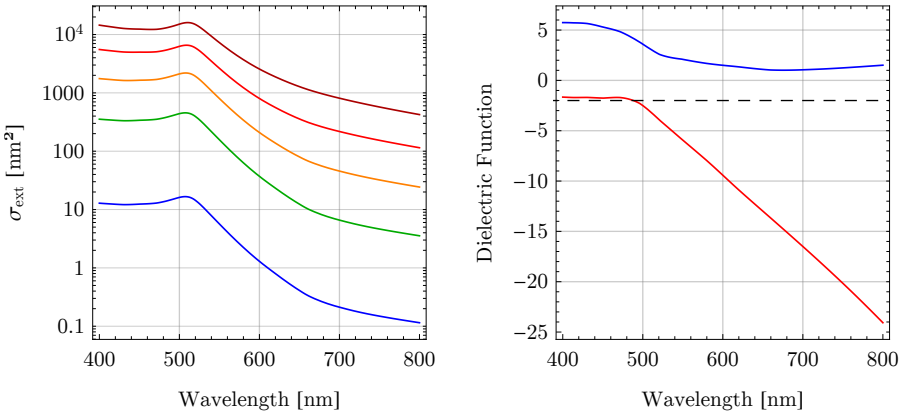

(a) Extinction cross section of a gold sphere with diameter 10 nm, 30 nm, 50 nm, 70 nm and 90 nm

(b) Dielectric function of gold [45]: $\Re[\epsilon(\omega)]$ (red), $\Im[\epsilon(\omega)]$ (blue). Resonance condition $\epsilon(\omega) = 2\epsilon_1$ (dashed)

Figure 2.3: Extinction cross section and dielectric function of gold in the visible wavelength range.

Figure 2.3 shows the extinction cross section for a gold nanosphere for different sizes and the dielectric function $\epsilon(\omega)$ of gold. The position of plasmon resonance is size independent located at a wavelength where $\epsilon(\omega) = 2\epsilon_1$. As $\epsilon(\omega)$ is a complex number, the plasmon resonance is slightly shifted to the position of $\Re[\epsilon(\omega)] = 2\epsilon_1$.

For ellipsoidal particles, plasmon resonances corresponding to each axis appear. Compared to a sphere of same volume, the resonance associated with the long axis shifts to the red while the short axes resonance is shifted to the blue. The criterion for first order plasmon resonances is

$$\Re[\epsilon(\omega)] = \frac{1 - L_j}{L_j}\epsilon_3 \tag{2.40}$$

while $\Im[\epsilon(\omega)] \approx 0$. Figure 2.4 shows the splitting of the plasmon resonances of aluminium ellipsoids of different aspect ratios. To illustrate the effect, aluminium particles are used, as they show a much more pronounced plasmon resonance than gold particles.

2.1.5 Effects due to Small Particle Size

The description of scattering and absorption by Mie and its approximation by Rayleigh assume perfect boundaries of the particles. For very small, especially metallic particle this assumption does not hold any more and corrections due to the size have to be introduced.

As introduced in the previous section, metals can be described as ions surrounded by a gas of free electrons. Those electrons behave like a kinetic gas, they move on straight trajectories until they are scattered e.g. at an ion. The average time between two successive scattering events is called scattering- or relaxation time τ. The velocity of electrons participating at conductivity is close

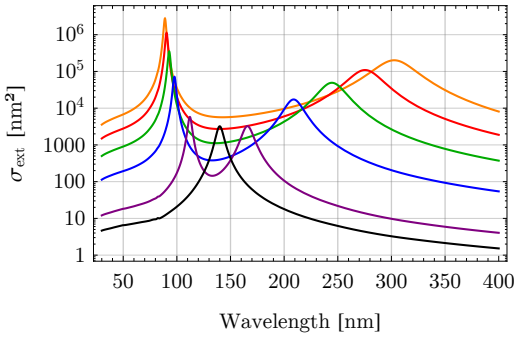

Figure 2.4: Extinction spectra of aluminium ellipsoids for unpolarized light. Two main axes are kept constant at 10 nm, the third axis varies from 20 nm to 100 nm in steps of 20 nm (colour). For comparison, the extinction of a sphere with the same volume as the smallest ellipsoid is plotted (black).

to the Fermi-velocity v_F. Thus the free path length of a conduction electron is $l_\infty = v_F \cdot \tau$.

If the particle size becomes comparable to the the free path length, for metals some 10 nm, scattering of the electron at the surface gets a relevant contribution to the relaxation time.

For nanoparticles, when surface scattering gets into play, the damping constant gets modified depending on the particle radius r:

$$\gamma_{fe}(r) = \gamma_{fe,bulk} + g\frac{v_F}{r} \tag{2.41}$$

with a dimensionless proportionality factor g in the order of 1 [46]. The dielectric function 2.36 is adjusted by replacing the Drude part:

$$\epsilon(\omega) = \epsilon(\omega)_{bulk} + \frac{\omega_P^2}{\omega^2 + i\gamma_{fe,bulk}\,\omega} - \frac{\omega_P^2}{\omega^2 + i\gamma_{fe}(r)\,\omega}. \tag{2.42}$$

This leads to an increased imaginary part of the dielectric function and thus to higher absorption of a particle. Figure 2.5 shows the modified dielectric function for a 20 nm gold nanosphere.

2.1.6 Particle on a Surface

Up to now, only particles embedded in a homogeneous medium were discussed. When a particle is placed onto a surface, the surface strongly influences the scattering and absorption properties of the particle. In the first part of this section, the influence of a dielectric surface on the polarizability will be introduced, in the second part, the effect of a reflecting dielectric mirror stack on the emission probability of a dipole and thus the scattering rate will be discussed.

Dielectric Surfaces

The influence of the presence of a surface in the vicinity of a nanoparticle was e.g. investigated by Wind et.al. [47, 48] using a multipole expansion analogues

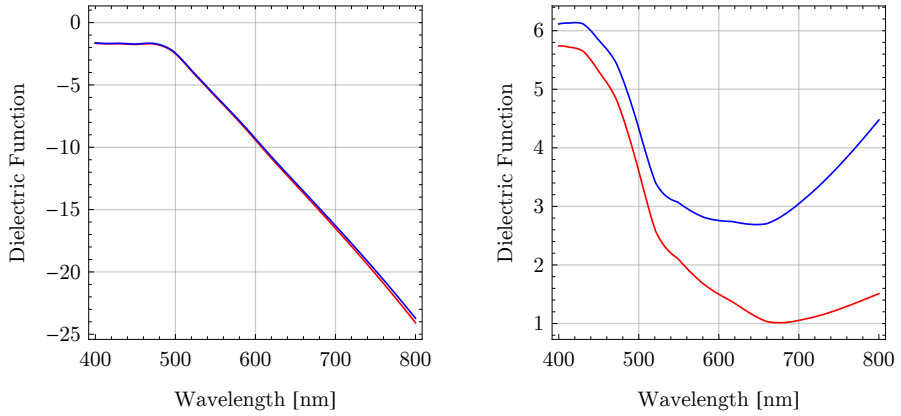

(a) $\Re[\epsilon(\omega)]$ (b) $\Im[\epsilon(\omega)]$

Figure 2.5: Real and imaginary part of the dielectric function of gold for bulk [45] (red) and for small particles (blue) with $g = 1.5$ and particle diameter 20 nm

to the method used by Mie. For a dielectric or metallic sphere far away from its plasmon resonance, they give a solution of the problem in dipole approximation.

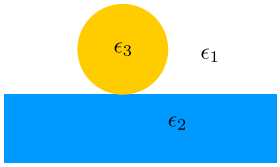

Figure 2.6: Particle on a surface: optical constants of the surface, the particle and the environment.

The polarizability of a sphere with a dielectric constant ϵ_3 on a surface with dielectric constant ϵ_2 in an environment with ϵ_1 (see figure 2.6) gets modified according to an extended geometry factor:

$$\alpha = \epsilon_0 V_p \frac{\epsilon_3 - \epsilon_1}{\epsilon_1 + L_s (\epsilon_3 - \epsilon_1)}^2 \tag{2.43}$$

with the extended geometry factor L_s. For a dipole orthogonal to the surface

$$L_\perp = \frac{1}{3}\left[1 - \frac{1}{4}\frac{\epsilon_2 - \epsilon_1}{\epsilon_2 + \epsilon_1}\right]. \tag{2.44}$$

For a dipole parallel to the surface

$$L_\parallel = \frac{1}{3}\left[1 - \frac{1}{8}\frac{\epsilon_2 - \epsilon_1}{\epsilon_2 + \epsilon_1}\right]. \tag{2.45}$$

[2]In the original publication [47], an additional factor ϵ_1 is added in the numerator. This is inconsistent with the results for a sphere in free space. As long as the environment is vacuum or air, this factor doesn't stand out as it is (close to) 1.

The extinction of metallic particle gets red-shifted with increasing contrast of the refractive index of the supporting medium and the environment. Figure 2.7 shows the effect of a fused silica surface on the extinction cross section of a gold nanosphere.

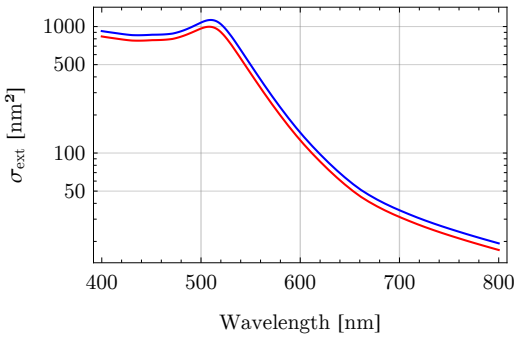

Figure 2.7: Extinction cross section σ_{ext} of a 40 nm gold sphere on a fused silica surface (blue) compared to the cross section of a similar particle in vacuum (red).

Reflecting Multilayer Surfaces

When a dipole is placed close to a reflecting surface, its emission pattern[3] can get influenced as the reflected electro-magnetic waves can interfere with the directly emitted waves, thus having the potential to change the emission properties substantially. To study the influence of a reflecting surface on the dipole, Novotny and Hecht [49] use an ansatz based on a Green's function to get the energy dissipation rate of the dipole.

For the energy dissipation rate of a dipole normalized to the free space emission rate parallel to the surface, aligned along one coordinate axis, Novotny and Hecht obtain

$$\frac{P}{P_0} = \frac{3}{4}\int_0^\infty \mathrm{d}s\, \Re\left[\frac{s}{s_z}\left(r^s - s_z^2 r^p\right)\mathrm{e}^{2\mathrm{i}k_1 z_0 s_z}\right] \tag{2.46}$$

where s is the radial component of the wave vector of the emitted wave normalized to the total wave vector k_1, s_z is the normalized normal component of the wave vector. From geometric consideration follows $s_z = \sqrt{1-s^2}$. r^s and r^p are the complex reflectivities for orthogonal and parallel polarized light. z_0 denotes the distance of the dipole to the surface.

The complex reflectivity of a multilayer Bragg-mirror is calculated using a matrix formalism, e.g. described by Furman and Tikhonravov [50].

To investigate the effect of a Bragg-mirror to a dipole on top, a stack of 15 pairs of $\lambda/4$ thick layers of SiO_2 and TaO_5 on a fused silica substrate, as used in the experiments described in this work is considered. In contrast to standard Bragg-mirrors, the last layer is a low diffracting SiO_2 layer, slightly thinner than

[3]The emission of the dipole can be due to scattered light but also e.g. an electronic transition of an atom.

$\lambda/4$, serving as a spacer in order to bring the particle, and thus the corresponding dipole, laying on this layer to the maximum of the reflected field.

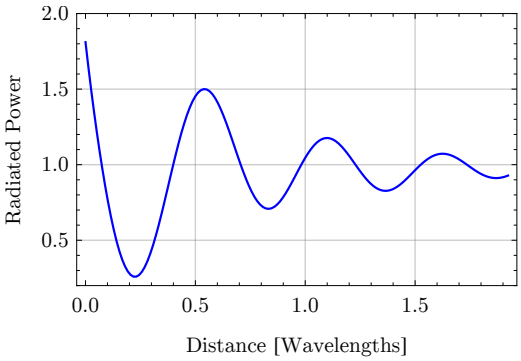

(a) Normalized emission rate of a dipole depending on its distance to a Bragg mirror with 15 layer pairs and a $\lambda/4$ thick spacer layer.

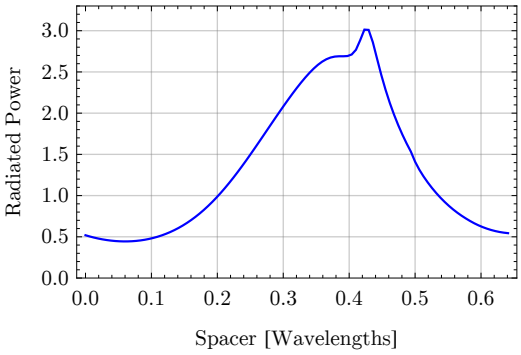

(b) Normalized emission rate of a dipole 20 nm over a Bragg mirror with 15 layer pairs depending on the spacer layer thickness.

Figure 2.8: Normalized energy dissipation rate of a dipole close to a multilayer surface.

In figure 2.8, the normalized emission rate of such a dipole in the vicinity of a Bragg-mirror is shown in dependence of its distance to the mirror surface and to the thickness of the spacer layer. Both parameters have large impact on the radiated power of the dipole and it can be strongly reduced as well as enhanced by a proper choice of both dimensions.

For the nanoparticles used in the described experiments, the dipole is assumed to be in the centre of the particle. For particles of a radius, and thus a distance of the dipole to the mirror surface around $\lambda/20$, the effect of a Bragg-mirror with a $\lambda/4$ thick spacer layer on the scattering cross section of a particle is comparable to that of the surface as discussed before.

By proper design of the mirror and especially the spacer layer, it would be possible to double the scattering rate of a nanoparticle.

Up to now, scattering and absorption of light at nanoparticles has been discussed. It has been shown, that for a proper description, many more or less subtle effects have to be considered: at first the choice of the right model is crucial: for particles much smaller than the wavelength, Rayleigh's theory using an induced dipole gives simple and correct results. For larger particles the extensive treatment by Mie using a multipole expansion is necessary to characterize the particle's interaction with light. It has been shown, that the environment of the particle influences the scattering and absorption tremendously. The effect of a particle in the vicinity of a mirror has been discussed just above. What happens, if a second mirror is added, forming an optical cavity will be shown in the next section.

2.2 Optical Resonators

To retrieve spectroscopic signals from individual nanoparticles, the very weak interaction of the particle with light has to be enhanced. One way to do so, are multiple interactions of the light with the object. Therefore the light has to cycle around for many times and interacts at each round trip with the particle. Such devices, allowing light to be stored and to cycle around, are called resonators. The most simple optical resonator, the Fabry-Pérot[4] resonator, is made of two plane parallel mirrors between which the light is reflected back and forth for many times.

This section introduces the basic theory of Fabry-Pérot-type resonators which will be extended to spherical and elliptical mirror resonators. Throughout the section a special focus is set to the impact of (nano-) matter inside the cavity.

The first part of the discussion follows the author's master thesis [52], which has been inspired by the book of Saleh and Teich [53].

2.2.1 Plane-Mirror Resonator

Resonances of an Ideal Cavity

Consider a plane wave

$$u(z,t) = u_0 \mathrm{e}^{i\omega t - ikz} \tag{2.47}$$

with frequency ω and wave vector $k = \omega/c$ aligned along the z-axis travelling between two infinitely large and perfectly reflecting plane parallel mirrors of distance d as depicted in figure 2.9.

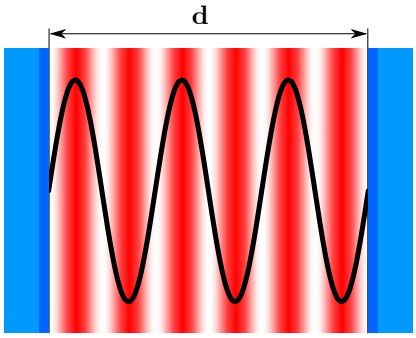

Figure 2.9: A plane wave in an idealistic Fabry-Pérot cavity: the electric field (black curve) and the respective intensity distribution (red) have nodes at the mirror surfaces.

When this wave travels from mirror 1 to mirror 2 and back, it accumulates a phase φ of

$$\varphi = 2dk. \tag{2.48}$$

If the refractive index inside the cavity is smaller than that of the mirror, the wave gets phase shifted by π at each reflection.

[4]There is some ambiguity on the spelling: Alfred Pérot spelled himself with accent in scientific publications, in his birth certificate, he's spelled without [51].

The wave is self-reproduced if the accumulated phase per round-trip is a multiple of 2π.

$$q \cdot 2\pi = 2dk = 2d\frac{\omega}{c} \qquad q \in \mathbb{N} \tag{2.49}$$

The phase shift of 2π due to the reflections is not considered here without loss of generality.

This condition leads to resonance frequencies

$$\omega_q = q\frac{\pi c}{d} \tag{2.50}$$

$$\nu_q = q\frac{c}{2d}. \tag{2.51}$$

In the wavelength representation this result gets more pictorial: the nodes of a standing wave are at the mirrors, so the resonator length has to be a half-integer multiple of the wavelength:

$$d = q\frac{\lambda_q}{2}. \tag{2.52}$$

A commonly used quantity to describe the size of a resonator is the spacing between to subsequent resonance frequencies, the *free spectral range*

$$\nu_F = \frac{c}{2d}. \tag{2.53}$$

Transmission and Reflection

So far, only light inside the resonator was taken into account without considering how light could enter or leave the cavity. In the following, transmission and reflection of a resonator with imperfect mirrors and a lossy medium inside will be discussed.

The resonator is set up of two mirrors with reflectivity for the electric field r_1 (r_2), transmission t_1 (t_2) and losses l_1 (l_2). For the intensity, the reflectivity R_i is given by $R_i = r_i^2$, the transmission $T_i = t_i^2$ and for the losses $L_i = l_i^2$. Energy conservation yields $R_i + T_i + L_i = 1$.

Inside the cavity, there is some absorbing material inducing a loss l to the electrical field and $L = l^2$ to the intensity of a wave travelling through this medium.

Figure 2.10 shows such a cavity together with the impinging field $u_{in}(r,t)$ and the transmitted field components $u_0(r,t)$, $u_1(r,t)$...

A fraction of an incoming plane wave $u_{in}(r,t)$ enters the cavity by transmission through the first mirror. Than the light bounces back an forth, at each mirror, a (small) portion of the light gets absorbed and transmitted. The light leaking through the first mirror builds up the reflected field while the light exiting at the second mirror is the transmitted field of the cavity.

The field directly transmitted through both mirrors is

$$u_0(r,t) = u_{in}(r,t)t_1 v t_2 \mathrm{e}^{i\varphi}, \tag{2.54}$$

where $\varphi = dk$ is the accumulated phase and $v = \sqrt{1-L}$ the transmission of the field of the lossy intra cavity medium. For the subsequent round trips the

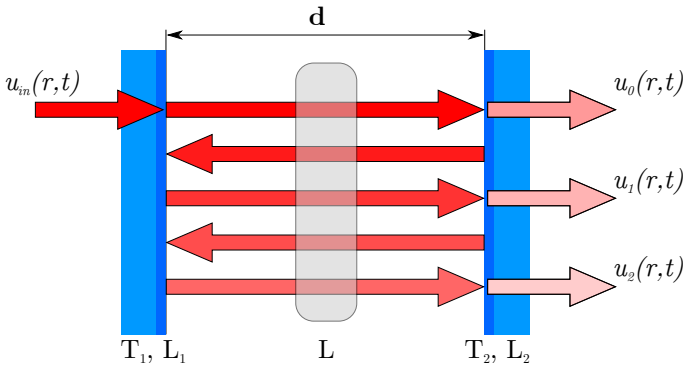

Figure 2.10: Fabry-Pérot cavity with losses. The transmitted field is composed of several components. The Intensity of the colouring illustrates the field amplitude.

transmitted fields are

$$\begin{aligned} u_1(r,t) &= u_{in}(r,t)t_1t_2v^3r_1r_2\mathrm{e}^{3i\varphi} \\ u_2(r,t) &= u_{in}(r,t)t_1t_2v^5r_1^2r_2^2\mathrm{e}^{5i\varphi} \\ u_2(r,t) &= u_{in}(r,t)t_1t_2v^7r_1^3r_2^3\mathrm{e}^{7i\varphi} \end{aligned} \tag{2.55}$$

and so forth. Summation over all $u_i(r,t)$ leads to the total transmitted field

$$\begin{aligned} u_t(r,t) &= \sum_{n=0}^{\infty} u_i(r,t) \\ &= u_{in}(r,t)t_1t_2v\,\mathrm{e}^{i\varphi}\sum_{n=0}^{\infty}\left(v^2r_1r_2\mathrm{e}^{2i\varphi}\right)^n \\ &= u_{in}(r,t)t_1t_2v\frac{1}{\mathrm{e}^{-i\varphi}-v^2r_1r_2\mathrm{e}^{i\varphi}} \end{aligned} \tag{2.56}$$

The measured quantity is not the electric field but the intensity. Normalizing the transmitted intensity by the input intenisty yields the transmission of the cavity

$$\begin{aligned} T_{cav} &= \frac{|u_t(r,t)|^2}{|u_{in}(r,t)|^2} \\ &= \frac{T_1T_2(1-L)}{(1-(1-L)\sqrt{R_1R_2})^2+4(1-L)\sqrt{R_1R_2}\sin^2\varphi}. \end{aligned} \tag{2.57}$$

For mirrors with low losses and low transmission ($R_i \approx 1$) this expression can be simplified to

$$T_{cav} \approx \frac{4T_1T_2}{(2L+L_1+L_2+T_1+T_2)^2+16(\varphi_0-\delta\varphi)^2} \tag{2.58}$$

where φ_0 is a multiple of π and $\delta\varphi$ a small variation around φ_0.

Rearranging this equation leads to the common expression for the transmission of the cavity including a Lorentz-shaped resonance:

$$T_{cav} = \frac{4T_1T_2}{(2L+L_1+L_2+T_1+T_2)^2} \cdot \frac{\frac{1}{4}\left(\frac{2L+L_1+L_2+T_1+T_2}{2}\right)^2}{\frac{1}{4}\left(\frac{2L+L_1+L_2+T_1+T_2}{2}\right)^2 + (\varphi_0 - \delta\varphi)^2} \quad (2.59)$$

In this equation, the first factor can be identified as the maximum transmission of a cavity

$$T_{cav,max} = \frac{4T_1T_2}{(2L+L_1+L_2+T_1+T_2)^2}. \quad (2.60)$$

The line width of a Lorentz-peak in phase-units is

$$\Delta\phi = \frac{2L+L_1+L_2+T_1+T_2}{2}. \quad (2.61)$$

While the phase is not directly accessible, the line width in units of frequency can directly be measured. The line width reads as

$$\Delta\nu = \frac{c}{2\pi d}\,\frac{2L+L_1+L_2+T_1+T_2}{2}. \quad (2.62)$$

In units of frequency, the line width depends on the resonator length. To get a measure for the narrowness of a resonance independent of the resonator geometry, the line width is compared to the free spectral range

$$\mathcal{F} = \frac{\nu_F}{\Delta\nu} \quad (2.63)$$

$$= \frac{2\pi}{2L+L_1+L_2+T_1+T_2}. \quad (2.64)$$

$\mathcal{F}$ is called *finesse*.

Another figure of merit for the losses of a resonator is the quality factor. It describes the ratio of the total stored energy to the energy lost per cycle.

$$Q = \frac{\nu_q}{\Delta\nu} \quad (2.65)$$

$$= \frac{2d}{\lambda}\mathcal{F} \quad (2.66)$$

Q depends on the size of the resonator. It is more common in the context of solid state physics than in quantum physics.

Reflection

The reflected portion of light can be calculated as above, summing over the field leaking out of mirror one [52]. From such a calculus or from energy conservation follows

$$R_{cav} = 1 - T_{cav}. \quad (2.67)$$

Power Enhancement

Due to the cycling light field inside the cavity, the power inside the resonator is enhanced compared to the input power.

The maximum power of an antinode of the standing wave in the resonator is

$$\begin{aligned} P_{cav} &= \frac{T_1 4(4-2(L+L_2+T_2))}{(2L+L_1+L_2+T_1+T_2)^2} P_{in} \\ &\approx 4T_1 \left(\frac{\mathcal{F}}{\pi}\right)^2 P_{in}. \end{aligned} \tag{2.68}$$

Temporal averaging over one period of the oscillation of the light field reduces the intracavity power by a factor of 2. Spatial averaging along the cavity mode lowers the power inside the resonator by an other factor of 2. The approximation is again only valid for small losses.

2.2.2 Curved Mirror Resonator

Confining light in between two flat mirrors as discussed so far is challenging: any tiny misalignment of the two mirrors leads to a displacement of the reflected beam and for not infinitely large mirrors, the beam will escape. The same holds for a non planar wave, a wave that is not perfectly orthogonally coupled to the resonator or a wave diffracted at the edges of a finite mirror.

To confine light to the resonator, the light has to be refocused at each round trip. This can be achieved by spherical mirrors. Within the paraxial approximation, they send light parallel to the optical axis to their focal point and vice versa.

This section will start with a short report on stability of spherical mirror resonators, motivate Hermite-Gaussian beams as eigenmodes and give results for the resonance frequencies. Finally the discussion of spherical mirror cavities will be expanded to elliptical mirror resonators.

Ray Confinement and Stability

To investigate resonator configurations allowing for stable confinement of light, ray-optics is used as a starting point. Stable confinement requires, that the travelling beam reproduces it self latest after some round trips. The propagation of a beam of light through the cavity can be analysed with help of beam transfer matrices [54], [53] leading to a relation between the resonator length and the radii of curvature of the mirrors determining stable configurations

$$0 \leq \left(1-\frac{d}{R_1}\right)\left(1-\frac{d}{R_2}\right) \leq 1^5. \tag{2.69}$$

By introducing the stability parameters g_1 and g_2, this expresseion can be reformulated

$$0 \leq g_1\, g_2 \leq 1. \tag{2.70}$$

[5] Here the sign convention by Kogelnik and Li [54] is used, where the distance and radii of concave mirrors are positive.

If the inequality is fulfilled, the resonator is called stable. In figure 2.11, stable configurations of resonators are illustrated. The stability diagrams shows in the green shaded area values of g_1 and g_2 fulfilling the inequality and examples for common resonator configurations.

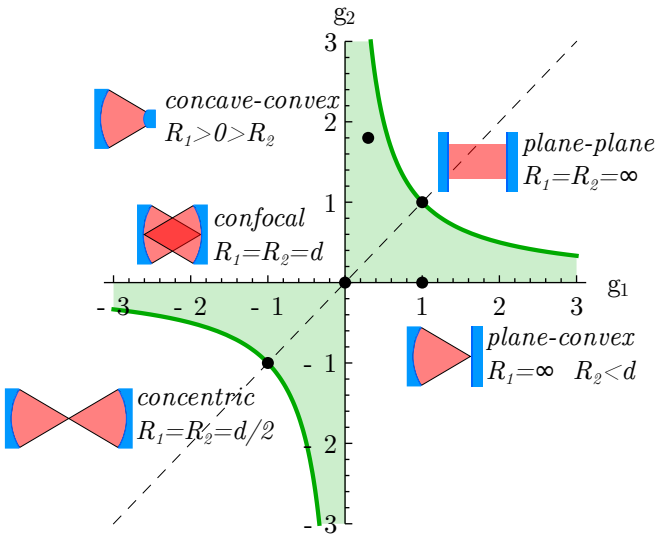

Figure 2.11: Stability diagram for curved-mirror resonators. Stable resonators lie in the green shaded area. Resonators on the dashed line are symmetric.

By simple means of ray-optics it is already possible to find stable resonator configurations. But with ray-optics, it is not possible to find information about the field distribution within the resonator or the resonance frequencies.

Gaussian Modes as Eigenmodes

Gaussian Beams Gaussian beams are solutions of the paraxial Helmholtz equation for spatially limited electromagnetic waves. In contrast to plane waves which obey a uniform intensity distribution and flat wave fronts, Gaussian beams have a gaussian intensity distribution and curved wave fronts leading to a converging or diverging beam. Figure 2.12 shows a schematic sketch of a Gaussian beam. The electrical field is given by

$$u(r,z) = u_0 \frac{w_0}{w(z)} \mathrm{e}^{-\frac{r^2}{w(z)^2}} \mathrm{e}^{-ikz - ik\frac{r^2}{2R(z)} + i\zeta(z)}. \tag{2.71}$$

At its focus at $z = 0$, the beam has a waist w_0 of

$$w(0) = \sqrt{\frac{\lambda z_0}{\pi}} \tag{2.72}$$

the waist evolves depending on the distance to the focus z

$$w(z) = w_0 \sqrt{1 + \left(\frac{z}{z_0}\right)^2}. \tag{2.73}$$

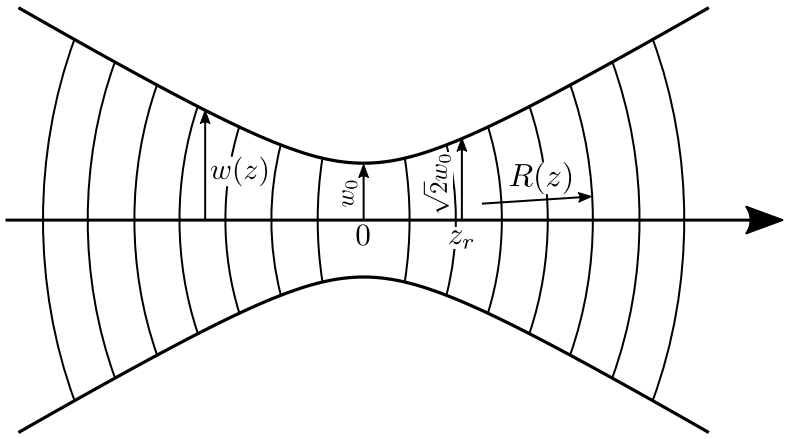

Figure 2.12: Sketch of a Gaussian beam with its characteristic quantities.

At the focus at $z = 0$ the beam has its tightest waist and diverges for larger distances. The waist has increased by a factor of $\sqrt{2}$ at a distance of z_0 from the focus, the Rayleigh length

$$z_0 = \frac{\pi w_0^2}{\lambda}. \tag{2.74}$$

According to equation 2.71 the phase along a Gaussian beam is

$$\varphi = kz - \zeta(z) + \frac{kr^2}{2R(z)}. \tag{2.75}$$

The phase along the beam from $z = -\infty$ to $z = \infty$ is additionally delayed by π. This effect is called Gouyeffect and described by the Gouy-phase

$$\zeta(z) = \arctan \frac{z}{z_0}. \tag{2.76}$$

From equation 2.71 also follows, that points of equal phase lay on curved surfaces, thus a Gaussian beam has curved wave fronts. The radius of curvature is given by

$$R(z) = z\left(1 + \left(\frac{z_0}{z}\right)^2\right). \tag{2.77}$$

At the focus $z = 0$, the radius is infinity, thus the wave is plane. At the Rayleigh length, the radius hat its minimum.

Gaussian Mode as an Eigenmodes of a Resonator By solving the Helmholtz equation with suitable boundary conditions or by the heuristic argument that a beam having curved wave fronts can reproduce itself when it circulates between two spherical mirrors, it can be shown that Gaussian modes are eigenmodes of a spherical mirror resonator.

For resonance, the light has to accumulate a multiple of 2π per round trip. The phase per round trip of a Gaussian beam, circulating between two mirrors

at positions z_1 and z_2 on the optical axis ($r = 0$) is given by

$$\begin{aligned}\Delta\varphi =& 2\left(\varphi(0, z_2) - \varphi(0, z_1)\right) && (2.78)\\ =& 2\left(k\left[z_2 - z_1\right] - \left[\zeta(z_2) - \zeta(z_1)\right]\right) && (2.79)\\ =& 2\left(kd - \Delta\zeta\right) && (2.80)\end{aligned}$$

By substituting $k = \frac{2\pi\nu}{c}$ and solving the equation $\Delta\varphi = q \cdot 2\pi$ for ν follows

$$\nu_q = \frac{c}{2d}\left(q + \frac{\Delta\zeta}{\pi}\right). \tag{2.81}$$

By introducing the free spectral range $\nu_F = \frac{c}{2d}$, which stays unchanged compared to the plane mirror resonator, the resonance frequency of a spherical mirror resonator is modified to

$$\nu_q = \nu_F\left(q + \frac{\Delta\zeta}{\pi}\right). \tag{2.82}$$

Hermite-Gauss-Modes Not only the Gaussian mode is a solution of the Helmholtz equation and thus an eigenmode of a spherical mirror resonator, also Hermite-Gaussian modes are solutions and eigenmodes. The Gaussian field distribution is modified by a Hermite polynomial along the two orthogonal radial axes

$$\begin{aligned}u_{l,m}(x, y, z) = u_0 \frac{w_0}{w(z)}\sqrt{\frac{1}{2^l l!}}\, H_l\left(\frac{\sqrt{2}x}{w(z)}\right) \mathrm{e}^{-\frac{x^2}{w(z)^2}} \sqrt{\frac{1}{2^m m!}}\, H_m\left(\frac{\sqrt{2}y}{w(z)}\right) \mathrm{e}^{-\frac{y^2}{w(z)^2}}\\ \cdot \mathrm{e}^{-ikz - ik\frac{x^2+y^2}{2R(z)} + i(l+m+1)\zeta(z)}\end{aligned} \tag{2.83}$$

The field is normalized to constant power. Figure 2.13 shows intensity patterns of various Hermite-Gaussian modes.

The phase of a Hermite-Gaussian beam (c.f. equation 2.83) depends also on the mode order resulting in resonance frequencies depending on the longitudinal mode order q as well as on the transversal orders l and m

$$\nu_{q,l,m} = \nu_F\left[q + (l + m + 1)\frac{\Delta\zeta}{\pi}\right]. \tag{2.84}$$

For spherical symmetrical mirrors, the resonance frequencies for equal values of $l+m$ are degenerate leading to modes that could also be described by Laguerre-Gaussian modes.

Very small radii of curvature of the cavity mirrors lead to a significant contribution of the Gouy-phase. This phase shifts the cavity lengths, at which the cavity is on resonance for a fixed wavelength of the probe light slightly away from the $\lambda/2$ spaced lengths introduced in the beginning of this section.

For resonators with a numerical aperture close to 1, the paraxial approximation doesn't hold any more, as transversal components of the wave vector cannot be neglected any more and a full vectorial treatment is necessary.

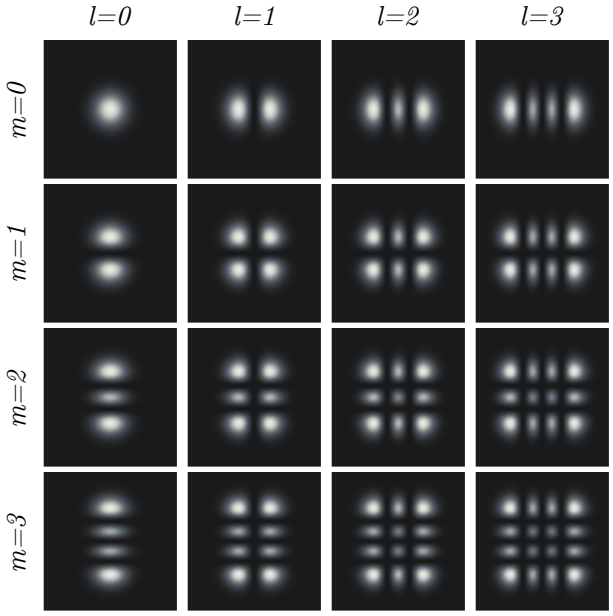

Figure 2.13: Intensity pattern of different Hermite-Gauss modes.

Elliptical Mirror Cavities

Up to now, optical resonators with spherical mirrors have been discussed. The assumption of spherical mirrors does not only simplify the understanding of such cavities, in many cases it is a good description of real cavities. For fiber based cavities this assumption usually does not hold any more. Here, the mirrors on the fibers are at least slightly elliptic leading to new properties of the resonator: the degeneracy of higher order modes is lifted and the mirror gets birefringent.

Resonance Frequency of Higher Order Modes The Gouy phase of a Gaussian mode depends on the radius of curvature of the cavity mirrors. For elliptical mirrors, this phases slightly differs for the two half axes of the elliptical mode leading to a lift of degeneracy of the higher order mode resonances. By separating the Gouy phase for both half axes, the resonance frequency can be written as

$$\nu_{q,l,m} = \nu_F \left[q + \left(l + \frac{1}{2} \right) \frac{\Delta\zeta_x}{\pi} + \left(m + \frac{1}{2} \right) \frac{\Delta\zeta_y}{\pi} \right]. \tag{2.85}$$

For a plane-concave cavity, mainly discussed in this work

$$\Delta\zeta_i = \arctan \sqrt{\frac{d}{r_i - d}} \tag{2.86}$$

where d is the cavity length and r_i the radius of curvature of a half axis of the curved mirror.

Birefringence of the Mirror Besides the splitting of higher order modes of same order, ellipticity of the cavity mirrors leads to a further splitting of each resonance into two orthogonally polarized lines where the polarization is oriented along the ellipsoids half axis. For dielectric mirrors, this could be attributed to stress-induced birefringence of the coating [55, 56]. A major contribution to the birefringence of an elliptical mirror comes from the geometry itself. By expanding the scalar theory for the eigenmodes of a resonator to a vector theory, Uphoff et. al. [34] find a phase shift between the two orthogonally polarized modes of a plane-concave cavity of

$$\Delta\varphi = \frac{1}{k}\frac{r_x - r_y}{r_x r_y} \tag{2.87}$$

with k the wave vector and r_x and r_y the radii of curvature along both half axes. This results in a frequency shift between both modes of

$$\Delta\nu = \frac{\nu_F}{2\pi k}\frac{r_x - r_y}{r_x r_y}. \tag{2.88}$$

For mirrors with an ellipticity of 0.9 as used in this work, the splitting is around several linewidths of the resonator.

Modematching

The basic properties of a plane parallel Fabry-Pérot resonator were derived assuming an incoming infinitely large plane wave that passes over to an infinitely extended standing plane wave inside the resonator. For a non-idealistic case, the coupling between resonator mode and the in- or out coupling mode is set by the overlap of the two modes.

The power coupling efficiency ϵ of two modes $\Psi_1(x, y, z)$ and $\Psi_2(x, y, z)$ at position z_o is defined as

$$\epsilon = |\langle\Psi_1|\Psi_2\rangle|^2 = \left|\iint_{-\infty}^{\infty} \mathrm{d}x\,\mathrm{d}y\ \Psi_1(x, y, z_o)\Psi_2(x, y, z_o)\right|^2 \tag{2.89}$$

Joyce and DeLoach [57] give practical solutions for the misalignment of two Gaussian modes. A more detailed but less handy study on the effects of imperfect mode matching has been done by Anderson [58]. For fibre-based cavities, the mode matching has been investigated by Gallego and co-workers. [59].

Due to imperfect mode matching as it is the case for fibre-based Fabry-Pérot resonators discussed in this work, it is possible to couple into many cavity modes simultaneously. In the scope of this work, the coupling to higher order cavity modes is very advantageous as these modes can be exploited for resolution enhancement or dispersion measurements.

Mode Mixing

Up to now, cavities with perfectly spherical or plane mirrors have been discussed to derive and to describe their basic properties. The modes of these resonators obtained by solving the paraxial Helmholtz equation have been individual Hermite-Gauss modes that are orthogonal to each other.

The geometry of the fibre-based resonators used for the experiments described in this work significantly deviates from this idealistic geometry: the concave mirrors fabricated to the end facet of an optical fibre by laser ablation have more a Gaussian than a spherical profile of a size not much larger than the fundamental cavity mode. The plane mirrors are at large length scales in the millimetre range as well as at short length scales, comparable to the mode size of the resonator of 2 µm to 3 µm not flat: they have a slightly wavy surface and the coating might not be perfectly homogeneous.

Thus the eigenmodes of the fibre-based resonators are no individual Hermite-Gaussian modes any more. Still, there are stable eigenmodes of the resonator that can be described as a superposition of Hermite-Gaussian modes. For small mode waists the mirror geometry resembles a spherical profile quite well, these modes are close to the known Hermite-Gauss modes. The deviations of the mirror profile from a perfect sphere lead to an admixture of further higher order Hermite-Gaussian modes and a slightly modified mode structure.

While low order transversal modes are barely influenced by the shape and size of the Gaussian mirror profile, the increasing size of higher order modes leads to a growing impact of the profile: the non-spherical profile adds more and more higher Hermite-Gaussian modes to each eigenmode of the resonator. The finite size of the mirror structure leads to large additional losses of these modes, predominately due to diffraction.

For certain cavity lengths it happens, that two modes of different longitudinal and transversal order have very close resonance frequencies as it is depicted in figure 2.14. If two very close resonances carry components of same Hermite-

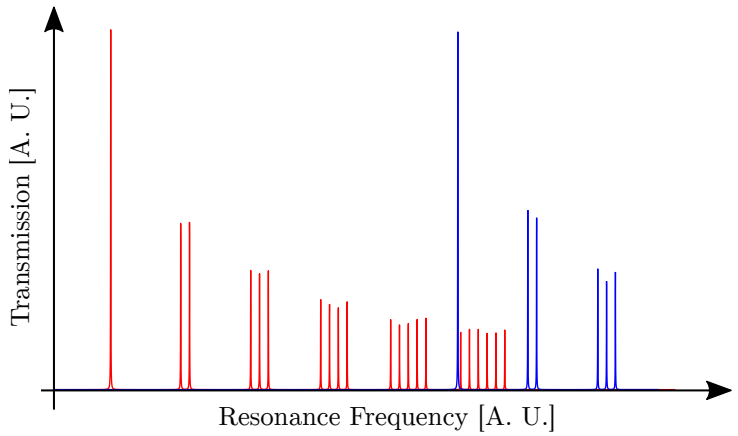

Figure 2.14: Principle of mode mixing. When the resonance frequency of a higher-order transversal mode (red) is close to the resonance frequency of a mode of the subsequent longitudinal order (blue), mode mixing can occur.

Gaussian mode order, they can couple to each other leading in general to a redistribution of light from the lower transversal order mode to the more lossy higher order transversal mode thus inducing increased losses in the former mode. Furthermore, the energy transfer to higher transversal mode components leads to a distortion of the regular Hermite-Gaussian mode function.

The two modes coupling to each other avoid crossing, thus the resonance frequencies of both are shifted when coming close to each other.

As for longer cavities the density of modes per cavity length grows, the coupling of modes gets more and more probable. At a certain point, the coupling dominates and the usable length of the cavity is reduced. The length range, the resonator is usable strongly depends on the mirror geometry, especially the ratio of structure size and cavity mode waist at the mirror. The larger the mirror compared to the mode, the more robust the cavity.

The effects of mode mixing including numerical calculations for predicting stable cavity length depending on the actual mirror geometry have been extensively studied by Benedikter [60, 61] for plane-concave cavities as used in this work and by Podoliak [62] for symmetrical cavities.

The coupling of modes can be triggered by very small distortions e.g. on the plane mirror surface. This leads on the one hand to large scale mostly worm-like structures as shown in figure 4.3 or on the other hand to small scale periodic modulations of the background e.g. of extinction measurements as depicted in figure 4.5(b).

In the scope of this work, mode mixing has been tried to be avoided by choosing suitable cavity lengths and angular alignment as it disturbs the scanning cavity microscope imaging. For future experiments, mixing due to nanostructures could be exploited to detect nonabsorbing but dispersing objects with very high sensitivity.

2.2.3 Particles in a Cavity

Up to now, the interaction of a nanoparticle with light and optical resonators were investigated individually. In scanning cavity microscopy, the enormous enhancement of interaction of light with nanoparticles placed inside an optical resonator is exploited. This section discusses the interplay of nanoparticles with resonators. As the particles are very small compared to the resonator mode, the interaction is discussed in a perturbative way: the cavity modes are assumed to be not influenced by the particle as discussed above for the mode mixing. The particles only cause additional losses and frequency shifts to the resonator.

From Losses to Extinction

In the previous section, the influence of a lossy intracavity medium on transmission, reflection and linewidth of a resonator has been investigated. The loss is described by the quantity L representing the portion of light getting lost when passing through the medium once. For the loss L no assumptions for the shape or position of the lossy medium were made. In contrast, in the first section, the extinction cross section for nanoparticles has been introduced: this quantity associates a disk of a certain size to the particle, blocking light passing the particle. To bring both concepts together, the extinction cross section has to be compared to the mode area and thus the mode waist of the light beam at the particle. Furthermore, enhanced extinction due to a standing wave inside the resonator has to be considered.

For a particle with an extinction cross section much smaller than the beam area, centred to a Gaussian beam, the extinction cross section is converted to

losses by

$$L_{free} = \frac{2\,\sigma_{ext}}{\pi w_0^2}. \tag{2.90}$$

When the particle is placed into an antinode of a standing wave inside an optical resonator, the light interacting with the particle has an intensity twice as high as the average intensity resulting in a modified relation of L and σ_{ext}

$$L_{cavity} = \frac{4\,\sigma_{ext}}{\pi w_0^2}. \tag{2.91}$$

The intensity enhancement due to the interference of the beam with itself inside a resonator is treated by the construction of L in section 2.2.1.

Shift of the Resonance Frequency

Inserting a dispersive medium into an optical resonator changes the optical path length and thus the resonance frequency if the resonator length stays constant. This holds not only for macroscopic objects like a glass plate, but also for nanoparticles. For calculating the frequency shift, the real part of the polarizability, describing the dispersion, of the particle is compared to the mode volume of the resonator [63].

The mode volume of an optical resonator is defined as [64–66][6]

$$V_m = \frac{1}{u_0^2} \int |u_{l,m}(r)|^2 \,\mathrm{d}^3 r \tag{2.92}$$

For Hermite-Gaussian modes normalized to constant total power as in equation 2.83, the mode volume is independent of the mode indices l and m, and depends only on the waist w_0 of the corresponding fundamental mode and on the cavity length d:

$$V_m = \frac{\pi\, w_0^2\, d}{4}. \tag{2.93}$$

The shift of the resonance frequency of an optical cavity due to a nanoparticle at the Rayleigh limit at position(x, y, z) for an arbitrary mode is given by [69]

$$\Delta\nu = \frac{\Re(\alpha)\,\nu_{Laser}}{2\epsilon_0 V_m} \left(\frac{u_{l,m}(x,y,z)}{u_0} \right)^2. \tag{2.94}$$

Birefringent Particles in a Cavity

An elliptical particle has a different polarizability along its main axis thus causing different phase shifts on impinging light along its main axes. This difference in phase shifts causes in general a modification of the polarization of the passing light. Inside a cavity, the rotation of the polarization of the circulating light is enhanced. This effect can be exploited e.g. for Laser-stabilization within the Hänsch-Couillaud scheme [70].

[6] In contrast to this definition of the mode volume used in cavity QED, in the context of solid state system based micro resonators like photonic crystal cavities, a modified definition of the mode volume is often used [67, 68]: $V_m = \dfrac{\int \epsilon(r) \left|u_{l,m}(r)\right|^2 \mathrm{d}^3 r}{\max\left(\epsilon(r) \left|u_{l,m}(r)\right|^2\right)}$.

For the cavities described in this work, one mirror is birefringent, leading to two nondegerate orthogonally polarized eigenmodes of the resonator. By adding an additional birefringent object to the cavity, the polarization states of the eigenmodes are expected to get modified. Moriwaki et al. [71] and Brandi et al. [72] have simultaneously but independently investigated the effect of two birefringent mirrors on the polarization state of a cavity mode. They treat the birefringent mirrors as a pair of non-birefringent mirrors and two birefringent elements like waveplates inside the cavity as depicted in figure 2.15 which also models the problem in hand.

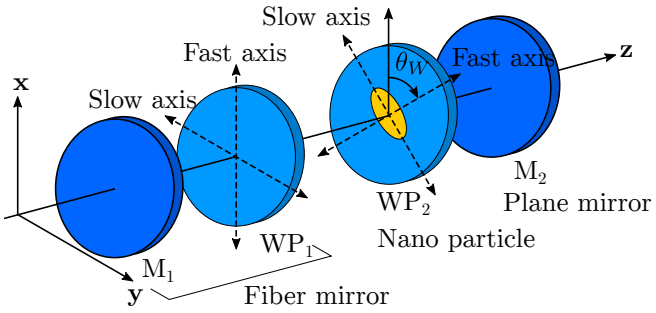

Figure 2.15: Cavity with two birefringent elements: Mirror M_1 and waveplate WP_1 correspond to the fiber mirror, waveplate WP_2 corresponds to the nanoparticle. (Figure adapted from [72])

For small relative phase shifts $\delta_1, \delta_2 \ll 1$ due to the two birefringent elements, Brandi finds an equivalent phase shift depending on the angle of the second birefringent element θ_W

$$\delta_{eq} = \sqrt{(\delta_1 - \delta_2)^2 + 4\delta_1\delta_2 \cos^2\theta_W}. \tag{2.95}$$

The angle of the equivalent element is given by

$$\cos 2\theta_{eq} = \frac{\delta_1/\delta_2 + \cos 2\theta_W}{\sqrt{(\delta_1/\delta_2 - 1)^2 + 4(\delta_1/\delta_2)\cos^2\theta_W}}. \tag{2.96}$$

The polarisation state of the transmitted or reflected light of the cavity can be calculated by a transfer matrix formalism based on the derivation of the cavity transmission (equation 2.56). For the transmitted electric field of an asymmetric cavity holds:

$$\boldsymbol{t_{cav}} = \boldsymbol{t_2} \cdot \sum_{n=0}^{\infty} (\boldsymbol{v} \cdot \boldsymbol{\psi} \cdot \boldsymbol{r_2} \cdot \boldsymbol{\psi} \cdot \boldsymbol{v} \cdot \boldsymbol{r_1})^n \cdot \boldsymbol{v} \cdot \boldsymbol{\psi} \cdot \boldsymbol{t_1} \tag{2.97}$$

with reflection matrices $\boldsymbol{r_i} = \left(\begin{smallmatrix} r_i & 0 \\ 0 & r_i \end{smallmatrix}\right)$ where r_i is the field reflectivity of mirror i, transmission matrices $\boldsymbol{t_i} = \left(\begin{smallmatrix} t_i & 0 \\ 0 & t_i \end{smallmatrix}\right)$ with field transmission t_i, propagation matrices $\boldsymbol{\psi} = \begin{pmatrix} e^{i\phi} & 0 \\ 0 & e^{i\phi} \end{pmatrix}$ with ϕ the accumulated phase and the loss matrix $\boldsymbol{v} = \begin{pmatrix} v_x e^{i\delta_{eq}/2} & 0 \\ 0 & v_y e^{-i\delta_{eq}/2} \end{pmatrix}$ introducing the equivalent phaseshift due to the birefringence of the cavity-particle system as well as losses due to the particle. The

losses are projected along the equivalent polarization axes:
$v_x = \sqrt{(1 - L_x)\cos^2(\theta_W - \theta_{eq}) + (1 - L_y)\sin^2(\theta_W - \theta_{eq})}$ and
$v_y = \sqrt{(1 - L_x)\sin^2(\theta_W - \theta_{eq}) + (1 - L_y)\cos^2(\theta_W - \theta_{eq})}$ where L_i are the losses along the main axes an elliptic nanoparticle.

Rotating the resulting transmission matrix $\boldsymbol{t_{cav}}$ with respect to the equivalent polarization angle θ_{eq} to the desired measurement basis allows for calculating the influence of the birefringence of nanoparticles to the observed transmission signal.

The experiments in this work have shown, that the polarization state of a fibre based cavity might be predominantly determined by the ellipticity of the mirror and eventually the birefringence of the nanoparticles inside might leave the resonator's polarization state unaffected (see section 4.4).

2.3 Enhanced Spatial Resolution Microscopy

The mightiness of optical instruments is mostly measured by their resolving power. It describes up to which spacing objects can be separated at the image. This section introduces resolution limits in classical microscopy which also limit the focusing of light within an optical resonator and thus the resolution of scanning cavity microscopy. Inspired by squeezing the position (or momentum) eigenstates of the quantum harmonic oscillator, a significant improvement of the spatial resolution by combining higher order modes is discussed.

2.3.1 Resolution Limits: Helmholtz, Rayleigh and Abbe

For the minimum distance of two incoherently self-luminous point-like objects at which they still can be discerned, Helmholtz [73] has introduced an explanation for microscopes while Lord Rayleigh [74] found a comparable model for telescopes. Both models are based on diffraction of the incoming light at the limited input aperture of the optical system. The input light from a point source gets diffracted at the aperture, the observer sees the diffraction pattern, an airy disk. Rayleigh has introduced an heuristic criterion up to which separation two of such airy discs are discernible: if the maximum of the diffraction pattern of one source is at the first minimum of the second, the two points are separable, if they are closer, they aren't. The minimum spacing for resolvable structures is given by

$$d = \frac{0.61\,\lambda}{\mathrm{NA}} \tag{2.98}$$

where λ is the wavelength and $\mathrm{NA} = n \cdot \sin\alpha$ the numerical aperture of the microscope objective with the full opening angle 2α. Figure 2.16 illustrates the Rayleigh criterion: the two light spots have a Rayleigh limited spacing.

A much deeper understanding of optical imaging has been provided by Ernst Abbe [75]. He investigated the image formation in a microscope for the imaging of coherently illuminated structures[7] [76]. Abbe investigated under which conditions one can resolve two neighbouring lines of a grating. He could show that two subsequent grating lines are resolvable, if the first order of the corresponding diffraction pattern can be seen by the objective[8]. This leads again to the well-known resolution criterion

$$d_{min} = \frac{\lambda}{\mathrm{NA}}. \tag{2.99}$$

Where NA is the numerical aperture of the objective. The result is up to a prefactor similar to that of Helmholtz and Rayleigh.

In a more general view, image formation according to Abbe can be seen as a series of Fourier transformations and frequency filtering. The objective performs a a Fourier transform to the back focal plane of the objective. Due to the finite diameter of the objective, higher frequency components of the object, corresponding to small structures, are cut out. The image is again Fourier

[7] As microscopy samples are very small, their illumination with any kind of light source can be treated as at least partly coherent.

[8] It is sufficient to receive only one of the two diffracted light cones. This is possible by a suitable tilted illumination and improves the resolution limit by a factor of 2.

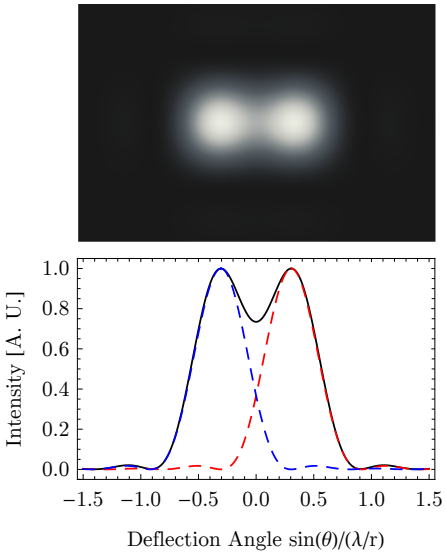

Figure 2.16: Two point sources at the Rayleigh limit: the maximum of the diffraction pattern of one source (dashed red) is at the minimum of the other (dashed blue). The black curve and the density plots shows the sum. The spacing depends on the aperture radius r and the wavelength λ

transformed to the image space by e.g. by imaging the back focal plane with an ocular:

$$\Omega_0(x,y) \xrightarrow{\text{Fourier}} \mathrm{F}_{\text{ideal}}(\alpha,\beta) \xrightarrow{\text{Filter T}(\alpha,\beta)} \mathrm{F}_{\text{real}}(\alpha,\beta) \xrightarrow{\text{Fourier}} \Omega_B(x,y) \quad (2.100)$$

The observed image is lowpass filtered by the optical system, high frequency components containing informations on small structures and sharp edges of the image get lost and thus, the image get smeared out as illustrated in figure 2.17.

2.3.2 Beating the Diffraction Limit

In Abbe's theory, the spatial resolution of a microscope is determined by the maximum transverse frequency of the image, that can pass the objective. For many decades, this was an insuperable limit. Only by shortening the wavelength, e.g. in electron microscopes, higher spatial resolutions at the cost of destructive radiation in vacuum were achievable.

Ultramicroscopy

One way to investigate structures smaller the diffraction limit is the observation of light scattered or emitted by very small particles or fluorophores attached to the structure of interest. Siedentopf and Zsigmondy used an illumination orthogonal to the optical axis of the microscope to detect and measure individual gold nanoparticles embedded in ruby glass [11]. Today their technique of ultramicroscopy is also known as light sheet microscopy. Advanced control of the emission individual dye molecules together with computer-based precise

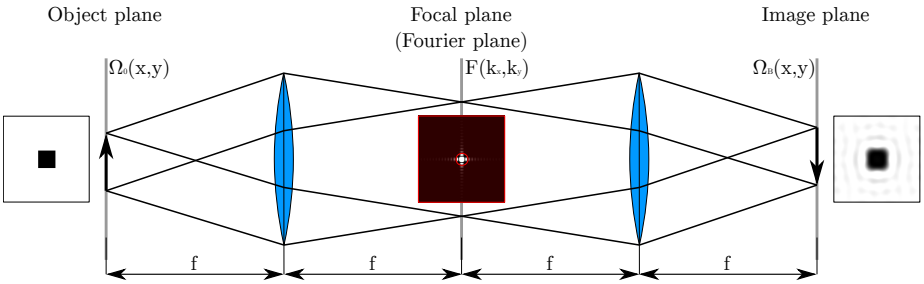

Figure 2.17: Abbe's theory of image formation. The imaging of an illuminated object via a lens can be seen as a Fourier transform at its backfocal plane. A second lens, the ocular, transforms the image back to the real space and it can be observed. Due to the limited aperture (in the picture depicted as red shaded area), the image gets lowpass-filtered and thus looses resolution. (Drawing adopted from [77])

methods for their localisation has enabled the invention of a large bunch of fluorescence microscopy techniques like STED [78], PALM [79], ect. allowing for imaging with a resolution at the nanometre scale.

Structured Illumination Microscopy

All methods mentioned above increase the spatial resolution by advanced localisation of fluorophores or light scattering particles. To observe non-emitting structures with enhanced spatial resolution, the transverse frequency space of the image has to be extended.

By spatially modulating the illumination of the sample, further frequency components can be added to the image. At structured illumination microscopy [49], the sample is illuminated with a sinusoidally modulated monochromatic pattern, generated by two counterpropagating laser beams, with an intensity pattern $I(x,y) = I_0\left[1+\cos\left(ux+\Delta\right)\right]$ where $2\pi/u$ is the spatial wavelength and Δ an arbitrary phase. In the Fourier domain this results into

$$F(k_x,k_y) = \sqrt{2\pi}\hat{S}(k_x,k_y) + \sqrt{\frac{\pi}{2}}\mathrm{e}^{-i\Delta}\hat{S}(k_x-u,k_y) + \sqrt{\frac{\pi}{2}}\mathrm{e}^{i\Delta}\hat{S}(k_x+u,k_y). \tag{2.101}$$

To retrieve the three Fourier components $\hat{S}$, three images at different phases Δ have to be taken resulting into a system of equations with 3 unknowns to be solved. By stitching the three Fourier components $\hat{S}(k_x,k_y)$, $\hat{S}(k_x-u,k_y)$ and $\hat{S}(k_x+u,k_y)$ together and Fourier transformation to the real space, a higher resolving image is obtained. The resolution gain depends on the modulation wavelength u and can be as large as 2 for a modulation wavelength equal to the wavelength of light.

2.3.3 Resolution Enhancement with Higher-Order Hermite-Gauss Modes

Besides a modulated illumination of the sample, higher order Hermite-Gaussian (or Laguerre-Gaussian) modes can be used to enhance the transverse momentum of the image and thus the spatial resolution. Various works have shown, that it is possible to focus radially polarized doughnut-shaped modes to focal spots beyond the standard diffraction limit [80–82].

The corresponding quantum system to an optical resonator is the quantum harmonic oscillator. As for the optical cavity, the eigenstates of the quantum harmonic oscillator are Hermite-Gaussian modes. To reduce the position (or momentum) uncertainty of the oscillator, the concept of squeezing has been introduced. Applying this method to microscopy with Hermite-Gaussian modes as in scanning cavity microscopy leads to an enhancement of the microscope's spatial resolution.

Squeezing of the Quantum Harmonic Oscillator

Due to the uncertainty principle, the momentum operator and the position operator of the quantum harmonic oscillator cannot be measured simultaneously better than $\langle(\Delta\hat{x})^2\rangle\langle(\Delta\hat{p})^2\rangle \geq \hbar^2/4$. In general, the uncertainty is distributed equally to $\langle(\Delta\hat{x})^2\rangle \geq \hbar/2$ and $\langle(\Delta\hat{p})^2\rangle \geq \hbar/2$. It is possible to reduce the uncertainty of one operator at the expense of the other. A state, for which holds $\langle(\Delta\hat{x})^2\rangle < \hbar/2$ or $\langle(\Delta\hat{p})^2\rangle < \hbar/2$ is called a squeezed state.

For the ground state (or the vacuum state of the operator) of the quantum harmonic oscillator, a squeezed state $|\xi\rangle$ can be written as a coherent superposition of even Fock states:

$$|\xi\rangle = \frac{1}{\sqrt{\cosh\rho}} \sum_{m=0}^{\infty} (-1)^m \frac{\sqrt{(2m)!}}{2^m m!} \mathrm{e}^{i\,m\theta} \tanh^m(\rho)\,|2m\rangle \tag{2.102}$$

with the squeezing strength ρ [83]. By superimposing the eigenstates of the resonator, which are Hermite-Gaussian modes, it is possible to reduce the position uncertainty of a state.

Combining Hermite-Gauss modes for higher resolution

A related principle can be used to enhance the spatial resolution in scanning microscopy techniques, like scanning cavity microscopy or confocal microscopy. Here, the sample is raster scanned with a superposition or subsequent Hermite-Gaussian modes to get an image. The modes can be generated using spatial light modulators [84], long cavities, where a coherent superposition of several modes is possible [85, 86] or short cavities (this work). To the knowledge of the author, a superposition of higher order Hermite-Gaussian modes for microscopy has been realized for the first time within this work.

Although a coherent superposition is not possible in the short cavity case, a heuristic combination of the modes can be found that minimises the point spread function. In contrast to the squeezing case, here both, even and odd modes are used to mimic the interference effect in the coherent case. As the summation now runs over odd and even modes, the variable m in the quantum

case is replaced by $m/2$. In the one-dimensional case, the modified point spread function or intensity distribution is

$$\Psi(x) = \frac{1}{\sqrt{\cosh \rho}} \sum_{m=0}^{\infty} (-1)^m \frac{\sqrt{m!}}{\sqrt{2^m}\frac{m}{2}!} \sqrt{\tanh^m(\rho)}\, |u_m(x)|^2 \tag{2.103}$$

with the squeezing strength ρ and Hermite-Gaussian modes

$$u_m(x) = \sqrt{\frac{1}{2^m m!}} \mathrm{H}_m\left(\frac{\sqrt{2}x}{w_0}\right) \mathrm{e}^{-\frac{x^2}{w_0^2}} \tag{2.104}$$

.

As this method is a heuristic procedure, there is some room for shaping the coefficients leading to slightly different properties of the resulting mode.

Figure 2.18 illustrates the principle of "squeezing" a Gaussian point spread function by combining higher order Hermite-Gaussian modes. The reduction of the size comes at first at the expense of a larger background modulation, this modulation is reduced with an increasing number of modes.

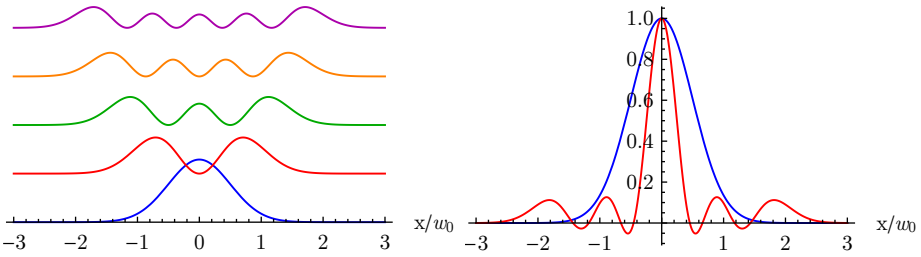

(a) Individual Hermite-Gauss modes that are added and substracted subsequently. The offsets are introduced for better visibility or the individual modes.

(b) Sum of 4 higher order modes (red) in comparison with fundamental mode (blue)

Figure 2.18: Reducing the size of the point spread function by combining higher order Hermite-Gaussian modes.

Compared to a coherent superposition of modes, using the squeezing formalism introduced above, the incoherent superposition of modes gives a narrower point spread function. This is illustrated in figure 2.19, where a coherent and an incoherent superposition of modes up to order 4 is shown. While for the coherent case only even modes contribute, in the incoherent case even modes are added and odd modes are subtracted.

This squeezing or superposition formalism can also be seen as a decomposition of the image into the orthogonal basis of Hermite-Gauss modes.

Limits of Mode Squeezing

Already a combination of few modes reduces the extent of the point spread function significantly as shown in figure 2.18. Figure 2.20 shows the size of the waist of the point spread function arising from a incoherent or a coherent superposition of modes in dependence of the highest contributing mode order. The plot shows, that a mode size well below the size of the fundamental mode

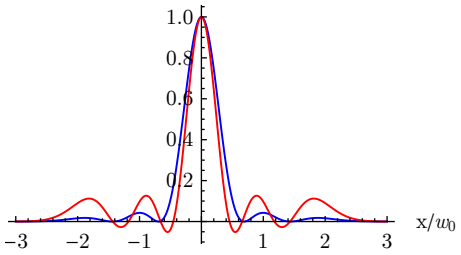

Figure 2.19: Comparison of a coherent (blue) and incoherent (red) superposition of modes up to the 4^{th} higher order mode.

is easily achievable while a very small mode requires an extremely high number of contributing modes. The waist of a coherent superposition of modes' point spread function decreases slower than that of an incoherent superposition of modes.

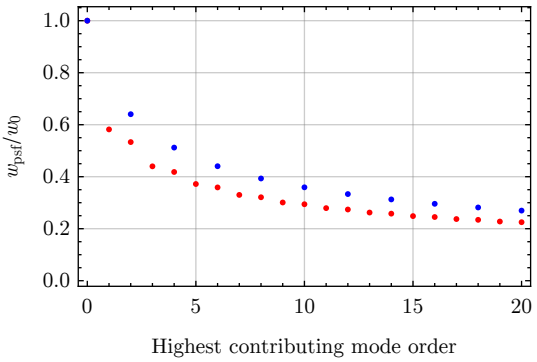

Figure 2.20: The $1/e^2$ radius w_{psf} of the central maximum of the point spread function of a coherent (blue) and incoherent (red) superposition of modes in units of the waist w_0 of the corresponding fundamental mode in dependence of the highest contributing mode order.

Beating the diffraction limit requires, that all contributing modes are focused diffraction limited. To achieve such a focus, Novotny and Hecht [49] show that the used objective has to be highly overfilled: the input mode has to be much larger than the input aperture. Thus the input mode is nearly a plane wave that gets focused down by the objective. This is only possible for the fundamental mode and the TEM01 and TEM10 mode. In the diffraction limited case, the squeezing method allows only for a small improvement of spatial resolution. For underfilled optical systems, that have a high NA but a small input mode, like in very short spherical cavities, this method allows to profit from the high NA for supporting also higher order modes and thus from the possibility to reduce the point spread function by the squeezing method shown above to get a resolution better than the fundamental mode.

Comparable approaches for increasing the spatial resolution of optical imaging by decomposing the image into higher-order modes have been discussed for

spatial mode demultiplexing [87], optical heterodyne detection [88] and holographic detection [89].

Especially in fiber-based cavities, many higher order Hermite-Gaussian modes can easily be excited due to imperfect mode matching. By clever combination, inspired by squeezing of the ground state of the quantum harmonic oscillator, these modes can be used to improve the spatial resolution of a scanning cavity microscope compared to its fundamental mode.

Chapter 3

Setup of the Scanning Cavity Microscope

3.1 Concept of a Scanning Cavity Microscope

In scanning cavity microscopy, the mode of an optical resonator is used as a scanning probe to measure the optical properties of nanoscaled objects. The cavity is set up of a plane mirror, that at the same time serves as a sample holder, and a concave mirror fabricated to the end facet of a single mode optical fibre. This tiny mirror allows for small radii of curvature and thus tight mode waists at very short cavity lengths enabling high spatial resolution and sensitivity. By scanning the plane mirror with respect to the fibre, and probing the cavity at each pixel, the optical properties of the plane mirror and thus of the samples on top can be determined.

To fully characterize the optical properties of an object with a size at the Rayleigh limit, it is sufficient to measure its polarizability tensor α. As the polarizabiliy is not directly accessible, it can be determined by a combination of an extinction ($\sigma_{ext} \propto |\alpha|^2 + \Im(\alpha)$) and a dispersion measurement ($\Delta\nu \propto \Re(\alpha)$).

The measurement of the extinction cross section is straight forward: an absorbing or scattering particle reduces the transmission and increases the linewidth of the resonator as illustrated in figure 3.1. By knowing the properties of an empty cavity, the extinction cross section of the particle can be deduced. In general, the fundamental mode is used for this type of measurement. Extinction measurements using higher order modes can be exploited to increase the spatial resolution by a clever combination of modes inspired from squeezing of quantum states.

The dispersion measurement is more tricky. The dispersing particle slightly shifts the resonance frequency of the cavity or, if the probe frequency is fixed, the length at which the cavity is resonant. The setup of the microscope is not stable enough to precisely measure changes in the order of a linewidth or below of the position of the resonance. For this measurement, the 2^{nd} higher order Hermite-Gaussian modes are used. Due to an asymmetry of the concave mirror on the fibre, these modes are not degenerate and have a slightly different resonance position. If the particle is placed to the centre of the three modes, the resonance frequency of the TEM02 and TEM20 mode will get affected by

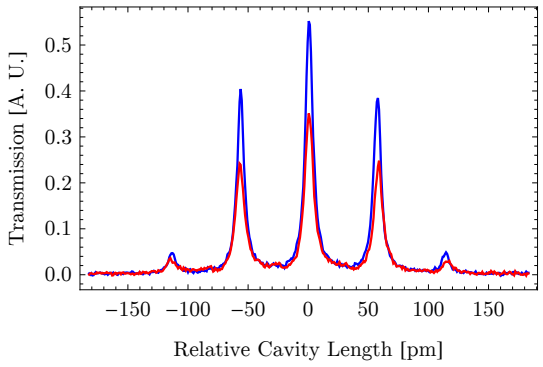

Figure 3.1: Transmission of a cavity without (blue) and with (red) a particle inside. Due to sidebands modulated to the probe laser for linewidth measurements, the resonance is split to a multiplet of lines. The extinction cross section of the particle is $71\,\mathrm{nm}^2$.

the particle as they have a non-zero field at the center while the frequency of the TEM11 mode remains unaffected as the cloverleaf shaped mode has no field at the centre and thus the particle can hide. From the shift of the TEM02 and TEM20 mode with respect to the TEM11 mode, the dispersion due to the particle can be deduced. Figure 3.2 illustrates the concept of the dispersion measurement.

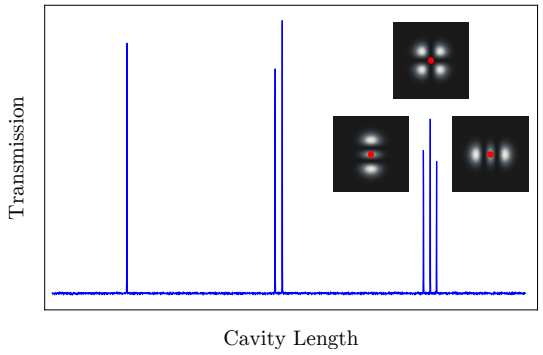

Figure 3.2: Principle of the dispersion measurement: The TEM02 and TEM20 modes are frequency shifted by a particle in the centre (red dot), while the TEM11 mode stays unaffected.

Furthermore, the ellipticity of the concave mirror on the fibre leads to a splitting of each mode of the resonator into two slightly frequency-shifted and orthogonally polarized modes. By coupling light to both modes and analysing them individually, extinction and dispersion signals along both polarisation axes of the cavity can be retrieved. This opens the possibility of reconstruction the polarizability tensor of the particle for the scanning plane.

In this chapter, at first fibre-based Fabry-Perot cavities are introduced. To

precisely position and align the fibre with respect to the sample, a stable mechanical setup is necessary that at the same time has many degrees of freedom for adjustment and scanning. This setup is presented in the subsequent section. It is followed by a description of the optical system to illuminate the cavity and to detect especially its transmission. To perform scanning cavity microscopy, an advanced experimental control is used to manage and to synchronise positioning of the sample, stabilising and modulating the cavity length, recording the resonator's transmission and on-line data evaluation. The measurement strategy and control is described in the last section of this chapter.

The setup described in this work, especially the mechanical part, continues the development started in the author's master thesis [52]. As the setup was continuously modified during the experiments shown in this work, only the most recent version is described. Relevant deviations at earlier stages are noted in the chapter on the results.

3.2 Fibre Fabry Pérot Cavities

The development of high-finesse optical resonators for ultra sensitive measurements has been driven mainly by three fields in physics: in gravitational wave physics, where smallest length variations of very long resonator due to gravitational waves impinging to it have to be measured [90, 91], in metrology, where high-finesse resonators serve as short-time frequency standard to generate narrowest and very stable laser frequencies [92], and in atom physics where high-finesse resonators opens the possibility to investigate coupled quantum systems made of atoms and a cavity [64]. To enhance the coupling between atoms and especially ensembles of atoms to the cavity, resonators with very small mode volume are required [93].

In the following, a brief motivation on atom-cavity coupling is given, leading to the introduction of fibre-based Fabry-Pérot resonators, that, starting from atomic physics, conquered wide interest in many fields of physics today. The fabrication and characterisation of such resonators is presented in a next step. Finally the fibres and plane mirrors used for the experiments in this work are introduced.

3.2.1 Cavities with small mode volumes

An optical resonator enables the coupling of a single atomic two-level system to an individual mode of light and thus to study the atom-light-interaction at the quantum level [64]. The coupling strength between cavity and atoms is quantified by the cooperativity

$$C = \frac{\left(\sqrt{n} g_0\right)^2}{2\kappa\gamma} \tag{3.1}$$

where n is the number of atoms, $g_0 = {}^{\mu E_0}/_{\hbar}$ the single atom coupling strength with the atomic dipole moment μ and the vacuum field $E_0 = \sqrt{{}^{\hbar\omega}/_{2\epsilon_0 V_m}}$ where V_m is the mode volume of the resonator, γ is the the spontaneous emission rate of the atom and κ the cavity photon decay rate.

For single atoms, the regime of strong coupling ($C > 1$ and $g_0 > \kappa\,\gamma$) can easily be reached with common cavities made of two spherical polished mirrors [94]. For ensembles of atoms like Bose-Einstein condensates, this regime is only accessible for cavities of very small mode volumes. In order to couple such a Bose-Einstein condensate, formed using an atom chip [95, 96], to a cavity [93], a resonator made of two curved mirrors fabricated by a CO_2-laser to the end facets of two optical fibres has been introduced [32, 33, 97].

Fibre Fabry Pérot cavities are set up either of two opposing optical fibres with mirrors on their end facet or such a fibre and a macroscopic large mirror as illustrated in figure 3.3. These cavities offer full access to the resonator mode and very good tunability of e.g. length and resonance frequency. Due to the flexibility of the laser ablation process for the fabrication of concave mirror structures, it is possible to widely vary the dimensions of these mirrors. This makes cavity lengths from ${}^{\lambda}/_{2}$ [98] to 1.5 mm [99] achievable. The perfect surface smoothness of the structures fabricated to the fibres in combination with high quality dielectric mirror coatings enable a nearly free choice of the resonator's optical properties, finesses up to 190 000 have been reported [34].

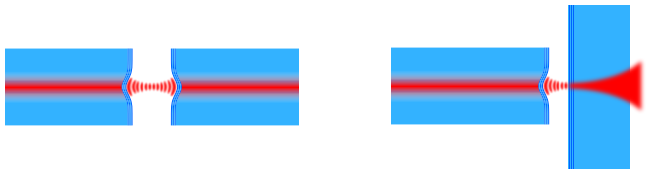

(a) Fibre-fibre cavity

(b) Fibre-plane mirror cavity

Figure 3.3: Different configurations of Fibre Fabry Pérot cavities: (a) a cavity set up of two micro machined fibres and (b) a cavity set up of a macroscopic plane mirror and a machined fibre.

All these features aroused the interest in various fields of physics. Today, not only neutral atoms [100, 101], but also ions [56, 102, 103], molecules [104], a wide selection of solid state emitters [98, 105–108], nanostructures [109] or mechanical systems [110–113] have been coupled in countless experiments to such cavities. Empty cavities have been used to investigate non-linear processes [114]. Experiments on Raman spectroscopy profit form enhanced pumping and emission in to the cavity mode due to the small mode volume [115, 116]. A further overview of recent experiments is given in the thesis by Kaupp [117].

3.2.2 Fabrication of Concave Mirrors on Optical Fibres

The centrepiece of an Fibre Fabry Pérot cavity is the micro machined concave mirror on the end facet of an optical fibre. The shallow depression is formed on the fibre end facet with few pulses of a CO_2-laser (wavelength 9.4 µm to 10.6 µm). The laser radiation gets strongly absorbed by fused silica of which fibres are made, the material gets molten and partly evaporated. Due to surface tension within a thin layer of molten glass, the surface gets extremely smooth [33, 117].

At this laser machining process, evaporation dominates melting the glass in contrast to other, similar processes, where the fibre tip is molten by a CO_2-laser to make micro lenses [118] or whispering gallery mode resonators [119]. The evaporation of glass is exponentially proportional to the temperature, which is again proportional to the laser intensity, that can be approximated by a parabolic distribution. Together, this leads to a Gaussian profile, evaporated out of the fibre [33]. Besides the intensity distribution of the laser, the structure depends also on its polarisation [34]. The more elliptic or even linear the polarisation of the light, the more elliptic structures are obtained.

The resulting structures of laser machining have nearly a Gaussian profile. In the centre, it can be approximated by a sphere of radius r:

$$r = \frac{D^2}{8t} \tag{3.2}$$

with $1/e$-diameter d and depth t as illustrated in figure 3.4. So the common theory for spherical mirror resonators can be applied for cavity modes with a transversal waist at the mirror that is small compared to the structure. For larger modes, the Gaussian profile cannot be neglected any more. This leads to

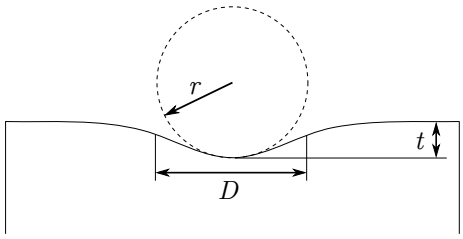

Figure 3.4: Approximation of the Gaussian mirror profile with $1/e$ diameter D and depth t by a sphere with radius r

modified eigenmodes of the resonator [61]. By using a spatial pattern of laser pulses of appropriate intensity, it is possible to achieve more spherical structures [99].

Measurements of the surface roughness by Hunger [32, 33] and Kaupp [117] with an atomic force microscope have shown an rms roughness below 1.5 Å corresponding to resonator losses due to scattering on the surface of 5×10^{-6} at a wavelength of 780 nm.

By variation of number, length and amplitude of the laser pulses and by varying the mode waist, a large range of structure sizes is achievable: shallow structures with a depth of some ten nanometres and small radii of curvature down to 10 µm for ultra short resonators [98] to deep structures (few micrometers) with radii of curvature of more than 100 µm can be fabricated with the same method.

To realize very short cavities that still allow for angular alignment, which is necessary as the produced mirror structures are not perfectly centred and the fibres are not cleaved perfectly orthogonal, the perimeter of the fibre is cropped with the laser as illustrated in figure 3.5.

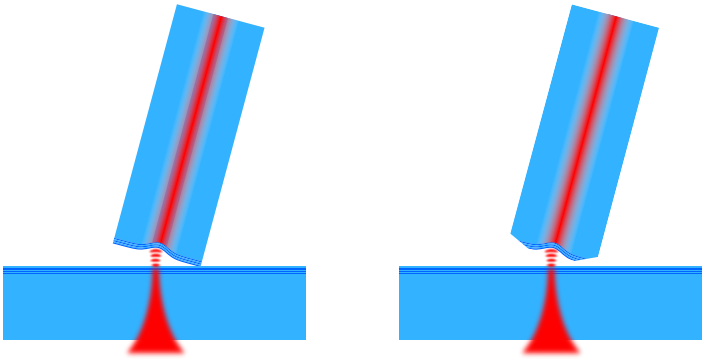

(a) An uncropped fibre bumps under an angle to the plane mirror.

(b) A cropped fibre unter an angle can still be scanned with respect to the mirror.

Figure 3.5: Cropping of the fibre's perimeter allows for shorter cavities.

One part of the fibres used in the scanning cavity microscope have been

produced with a CO_2-laser setup [120] at Laboratoire Kastler-Brossel in Paris in the group of Jakob Reichel. There, each fibre had to be placed individually onto a manual alignment stage. With help of a microscope included to the beam path, the fibre had to be brought to the focus of the laser. By switching the RF-pump of the laser, the pulse train could be controlled. This method was time consuming and hard to control, as no quantitative in situ analysis of the created structures was possible. Furthermore, switching the laser via the RF-pump does not give much control over the laser power.

In the scope of this work and a master thesis [121], a new fibre machining setup was designed and built.

3.2.3 Setup of the Munich Fibre Machining Experiment

The aim of the new setup has been to improve the Paris approach in many aspects: for a better stability of the laser and for more freedom in the control of laser pulses, an AOM[1] has been introduced. To get quick and accurate feedback on the produced structures allowing for optimisation, a white light interferometer for 3D surface reconstruction, directly accessible by the fibre positioning stage, has been added. Together with the high precision fibre positioning stage, the interferometer allows for precise positioning of the fibre with respect to the laser focus. For coarse alignment, a microscope with low magnification is included. To avoid excessive fibre handling between laser machining, characterisation and coating steps, a novel concept for mounting several fibres to a holding plate has been implemented.

The setup turned out to be a modular and versatile tool not only for fibre machining: also characterizing, marking and even cutting of larger substrates is possible.

Fibre Handling

The handling of individual fibres between different fabrication steps is time consuming as the fibres have to be mounted and aligned at each step and causes the danger of damaging or polluting the fibre tips. To facilitate the handling, several fibres are clamped onto a holding plate, that ensures precise positioning of the fibre tips on the plate. These plates can easily be mounted to the fibre positioning stage at the laser machining experiment allowing for subsequent processing of all fibres on the holding plate. After machining and characterising the fibres, the plates are stacked up and are ready for putting them into the coating machine.

Figure 3.6 shows an exploded drawing of a holding plate. The fibres are clamped with a clamping sheet Ⓔ fixed with small screws Ⓓ at a distance of 1 mm from the front edge. The clamping sheet sheet can be cut at s-shaped recesses next to each fibre position to remove individual fibres after coating. The fibre tips are protected by small noses at the sides of the plates. The long ends of the fibres are wound up and are stored in a race-track shaped slit within the plate. The non-machined ends of the fibres are clamped Ⓑ to grooves and cut such that they flush with the sides of the plate. Via these fibre ends, the fibres can be illuminated to localize their cores to centre the structures to fabricate.

[1] acousto-optic modulator

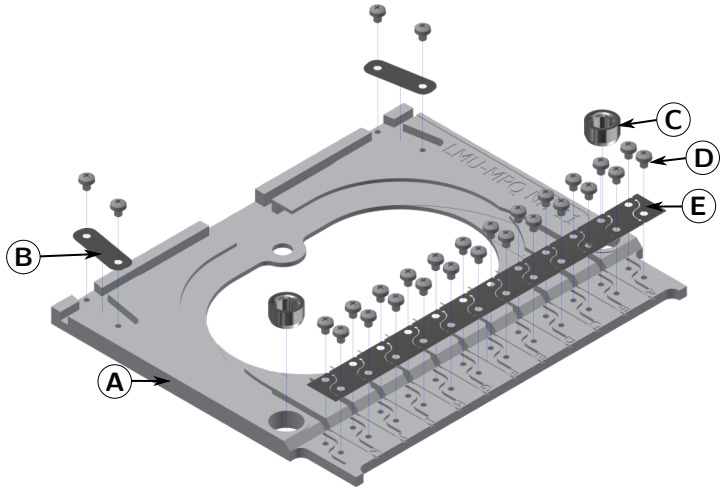

Figure 3.6: Holding plate for fibre machining and coating. Ⓐ Holding plate, Ⓑ Small clamping sheet for fibre ends, Ⓒ Bushing, Ⓓ Screw, Ⓔ Clamping sheet for fibre tips

The holding plates are centred on the positioning stage via three holes on conical seats.

For good coating results, it is necessary to place the fibres with an axial accuracy well below 100 µm in the vessel of the coating machine. To do so, five plates are stacked and fixed with two precision ground rods Ⓕ as illustrated in figure 3.7. These rods ensure a very accurate alignment of the plates to each other and to the mounting brackets Ⓖ. To avoid that the rods stick to the plates Ⓐ, made of aluminium, bushings Ⓒ are pressed into the corresponding holes.

The stacks of holding plates can be used for fibre storage. To prevent the fibres from dust and damaging, the front part of the holding plates is covered by an aluminium block with a pocket Ⓗ mounted on the lid of a dust-tight plastic box (*EMSA clip & close* 1.1 l). It is convenient to replace the ground rods by screws after coating, as the rods are delicate to disassemble.

3.2.4 Positioning

The spatially separated optics for finding, centring and characterizing, and laser machining the fibre demand for a positioning system with high accuracy and repeatability as an interconnect. In the experiment, a three axis ball-screw driven positioner is used. The axis (*PI miCos LS-180*) connecting the three different optics has a range of travel of 305 mm while the other two axes travel only 52 mm (*PI miCos PLS-85*). All three axes are equipped with an incremental linear measurement system allowing for a closed loop bidirectional positioning accuracy below 100 nm. The axes are driven with stepper motors, that in contrast to DC drives, do not jitter when keeping a position. This is mandatory for precise white light interferometry.

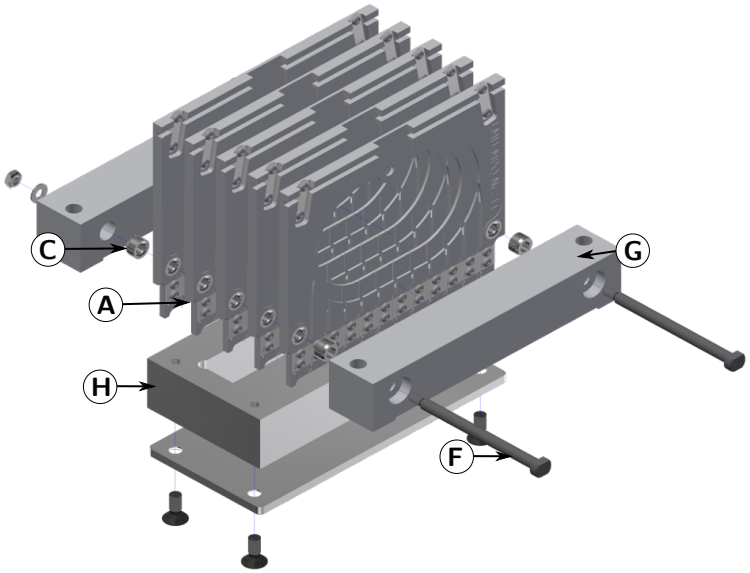

Figure 3.7: Stacked holding plates for coating and storing of micro machined fibres. Ⓐ Holding plate, Ⓕ Ground rod, Ⓖ Mounting brackets, Ⓗ Cover for fibre tips.

The system is powered with suitable motor drivers (*PI miCos SMC Hydra CM*) and operated with an advanced computer control system. Among many other features, this system knows the relative positions of the foci of the view finding microscope, the white light interferometer and the laser and allows for an automatic connection between these subsystems.

The fibre holding plates are mounted to the positioner via an adapter on conical centring pins and are fixed with a screw to avoid drifts of the plate because of vibrations during movement. These pins are hight adjustable and allow for adjustment of the tilt of the holding plate. Holders for other types of samples like microscope slides or spherical glass substrates can be attached to the same pins.

To prevent damaging the positioner or parts of the optics due to uncontrolled movements, the whole setup is designed such that moving parts at any position cannot collide with fixed parts of the setup.

3.2.5 Optics

The optical system comprises three subsystems described in the following: the view finder microscope, the white light interferometer and the CO_2-laser system. Figure 3.8 shows the complete setup.

View Finder Microscope

To initially find the position of each fibre, a view finder microscope with a large viewing angle at a sufficient magnification is used. An infinitely corrected long

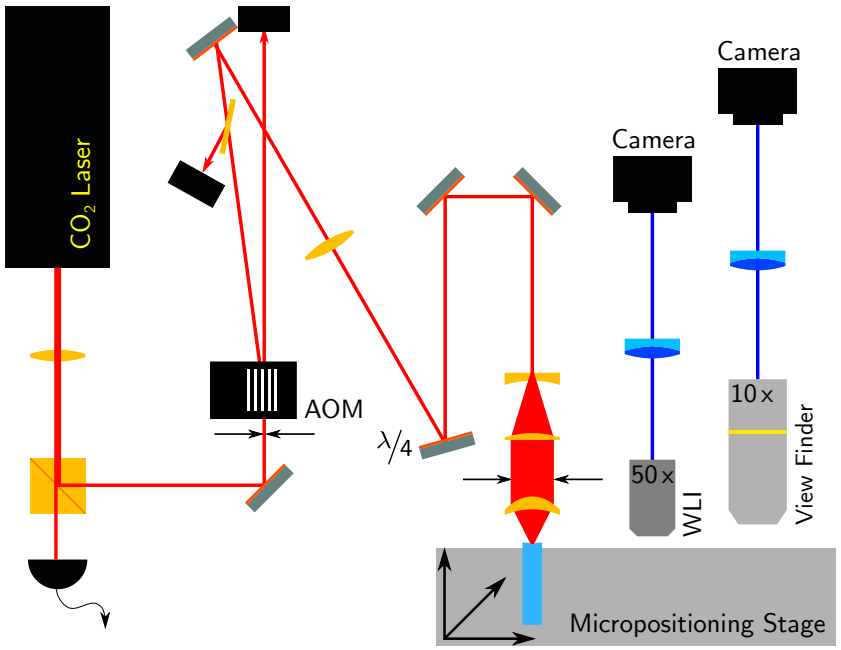

Figure 3.8: Setup for fibre machining.

working distance objective with a magnification of 10 (*Mitutoyo M Plan Apo 10x*) is imaged with an achromatic lens (f=200 mm) to a CMOS camera (*IDS Imaging UI-1640LE-C*). The field of view is with 2.6 mm × 2.1 mm large enough to find the position of fibres and larger samples. The reflected light microscope is illuminated with a white high power LED coupled to the beam path with an uncoated pellicle beamsplitter (*Thorlabs CM1-BP108*).

White Light Interferometer

The structures fabricated to the surface of an end facet of a fibre are characterized with a white light interferometer [122]. It is based on a Mireau-type microscope objective (*Nikon CF IC Epi Plan DI 50x*) as shown in figure 3.9. The objective contains an interferometer, that compares a reference beam, split of at a beam splitter at the output plane of the objective and reflected back on to a reference mirror with the light reflected at the sample giving an interference image of the surface profile of the sample. The objective is mounted onto a piezo scanning stage (*NPoint nPFocus100 controlled by NPoint LC 400*). The image and the interference pattern obtained with the infinitely corrected objective is imaged to a 5 mega-pixel CMOS camera with 14 bits digitalisation depth (*IDS Imaging UI-3580CP*) with a high quality tube lens with a focal length of 200 mm (*Mitutoyo MT-L*).

The interferometer is illuminated with a fibre-coupled blue LED at a wavelength of 470 nm. A large core multi-mode fibre (core diameter 200 µm), butcoupled to the emitting surface of the LED, ensures spatially coherent but temporally incoherent and homogeneous illumination of the objective. The fibre

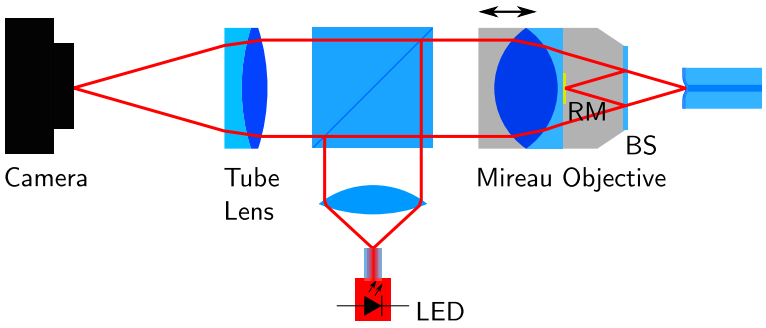

Figure 3.9: White light interferometer for characterizing the fabricated mirror profiles. The fibre is imaged with a Mireau objective and high-quality tube lens to a camera. The objective is illuminated with a fibre-coupled blue LED, for clarity, the blue light beam paths are depicted in red here. The objective contains an interferometer that compares a reference beam split of at a beam splitter (BS) at the front plane of the objective and back reflected inside the objective on a reference mirror (RM) with the light reflected by the sample.

is imaged to the objective with an aspheric lens through a beamsplitter cube. Due to the short wavelength and the high numerical aperture (0.55), a high transversal resolution is achieved. Due to the design of the objective, especially the internal mirror, a further shortening of the wavelength would not increase the resolution but lead to a dysfunctional interferometer.

By moving the objective along the optical axis, the phase of the interference pattern is shifted and recorded. From the phases of all pixels a hight map can be calculated. Due to the large amount of data, efficient measurement [123], namely a procedure taking the interference pattern at 5 different positions [124], and evaluation [125] strategies have to be used.

In the direction of the optical axis a resolution at the Ångström-level is possible, if mechanical noise is avoided and the recorded interference patterns are averaged in order to reduce the noise of the camera. The lateral resolution of 580 nm corresponds to the common diffraction limit.

The high magnification of the Mireau microscope is further used to accurately determine the position of the core of the fibre by localizing the illuminated core on the microscope image.

CO_2-Laser System

Centrepiece of the laser system is an industrial grade, water cooled and RF-driven pulsed CO_2-laser (*Synrad Firestar V40W OEM*). Triggered by a train of square pulses at a frequency of 5 kHz, the laser emits pulses at a wavelength of 10.6 µm. The pulse length and thus the average output power is set by the duty cycle of the driving pulses.

The temperature of the laser is controlled and stabilized by an air-water chiller (*Termotek P307*). To avoid an influence of slight temperature changes at the laser due to ambient air flow or thermal radiation, the laser is covered

with a metal box.

Half of the laser power is split of at a beamsplitter. This light can be used for power monitoring (*Thorlabs S350C*) or is dumped.

The other half is focussed to an AOM (*Gooch and Housego R37040-35-3-10*). The AOM allows to pick out individual pulses or pulse trains of controlled length, amplitude and shape. For safety reasons, the light in first diffraction order of the AOM is sent to the fibres while the 0^{th} order is dumped. Compared to switching the laser for pulse generation, the AOM approach is advantageous as the laser can run continuously and thus more stable while offering the possibility of precise shaping of length and amplitude of each pulse.

To keep the AOM itself thermally stable and to prevent it from overheating due to the RF- drive or the laser, it is also water cooled (*Ferrotec FT230*).

The light deflected by the AOM is guided to a periscope under an angle of 45°. At the upper, phase-shifting mirror, the linear polarized light is converted to circular polarized light. Besides changing the polarization state, the light is elevated by the periscope to an optical rail (*OWIS SYS65*) with an optical axis at the same height as the white-light interferometer and the view finder microscope.

The beam is aligned along the optical rail with help of two irises. To focus the light to smallest spots, the waist is expanded using an adjustable beam expander (*Ronar-Smith BXZ-10.6-2-8X*). The beam is focused to the fibre end-facet using aspheric lenses. Depending on the desired structure size, either a lens with a focal length of 12.7 mm (*Thorlabs AL73512-G*) or 25 mm (*Thorlabs AL72525-G*) is used. The latter is equipped with an air-curtain to prevent the deposition of glass debris during extensive machining tasks, like cutting glass slides.

The laser is protected from back reflected light from the target by a Brewster plate, placed before the phase shifting mirror. Both together act as a very poor man's optical isolator with an isolation of 1.8 dB.

Due to the long wavelength of 10.6 µm, the laser beam is also at millimetre-sized waists significantly divergent. This is in strong contrast to the experimenter's intuition for visible beams. Thus, the long beam path (around 3 m) requires guiding lenses to refocus the beam. The lenses have been chosen such, that the waists after the lenses lie within the AOM and the beam expander respectively. In a recent rebuild of the experiment at KIT Karlsruhe, the length of the beam path could be optimized to avoid the guiding lenses.

3.2.6 Fibres Used in the Experiments

The fibres used for scanning cavity microscopy have to obey several, partly contradictory requirements. For high spatial resolution as well as optimal sensitivity, the cavity mode waist should be as small as possible: this requires mirrors with a small radius of curvature. For polarisation resolved measurements, the mirror has to be elliptic. For a robust and discernible splitting also of higher order modes, the ratio of the two half axes, the ellipticity, should be around 0.9. For measurements involving higher order resonator modes, homogeneous coupling to all modes of one family is needed to discern the modes also when they are close together. To achieve such mode coupling a slight misalignment of structure and fibre core is necessary. When working with sidebands imprinted to the probe laser (see section 3.5.2), the higher order modes of one order have to

be sufficiently far apart from each other to avoid overlapping and thus mixing. Again, this requires a certain ellipticity.

All these requirements are hard to match and it is nearly unpredictable if a certain fibre will work or not. Dozens of fibres have been tested and only few had shown usable properties: mainly fibres with radii of curvature around 30 µm and an ellipticity near 0.9 could be aligned such that they fulfil the mentioned criteria. Figure 3.10 shows the two fibres that were successfully used in the described experiments. They stem from different fabrication campaigns and

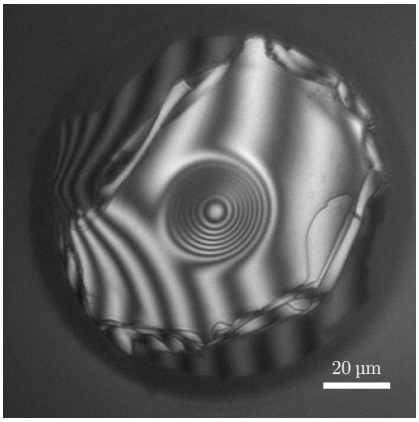

(a) Fibre 17-5. At the edges, delamination of the coating is visible.

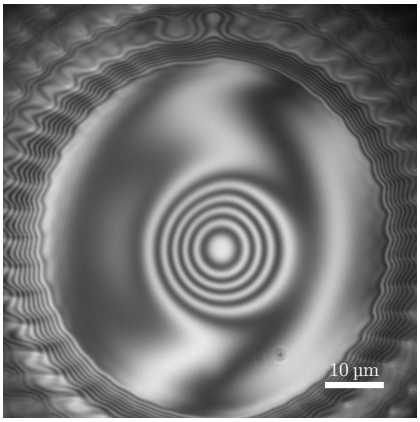

(b) Fibre 16-k. The wavy structure at the edge of the circular pedestal stems from the cropping process.

Figure 3.10: The two fibres used in the experiments described in this work. Note the different scale bars as the pictures have been taken with different objectives.

have slightly different mirror coatings.

The base material for both fibres is a a copper coated single mode fibre with an cut off wavelength of 770 nm (*Oxford Electronics CuBALL SM800-125CB*[2]). The copper coating (or any other metal coating like aluminium) is mandatory for the mirror coating process, as it has, compared to polymer coatings, a very little outgasing rate at elevated temperatures under vacuum.

Both mirror coatings have been applied by ion beam sputtering. At this method, unoxidised material for each layer like tantalum or silicon is sputtered of a target by accelerated argon ions. The target material condenses at the substrate and is oxidized by an oxygen plasma. Ion beam sputtering leads to a very dense, amorphous layer system with a very little defect concentration [126].

The first fibre, fibre 17-5, has been fabricated in Paris as described above. At the centre of the Gaussian depression, the radii of curvature of both axes are 30 µm and 37 µm. Is coated with a high reflective dielectric mirror centred at 780 nm (*Advanced Thin Films, Boulder*). The coating is designed for a transmission of 12 ppm with total losses of 12 ppm.

The second fibre, fibre 16-k, has been fabricated in Munich using the setup

[2]Company doesn't exist any more, alternative supplier e.g. ART Photonics

discussed in the previous sections. At the centre of the fabricated structure, the radii of curvature of both axes are 31 µm and 33.5 µm. Again it is equipped with a dielectric high reflective mirror coating centred at 780 nm (*LASEROPTIK*). It is designed for a slightly higher transmission of 16 ppm. The total losses at the mirror are 14 ppm.

By tilting the fibre in order to optimize the coupling to higher order cavity modes, the mode moves to the flanks of the Gaussian profile. Thus the effective radius of curvature defining the resonator mode gets significantly larger (around 60 µm).

3.2.7 Plane Mirrors

The counterpart of the fibre-based mirror in the scanning cavity microscope is a macroscopic plane mirror. These mirrors are deposited on super-polished fused silica substrates with a diameter of 12.7 mm. A perfectly smooth surface is mandatory to avoid scattering losses as well as mode mixing induced by surface imperfections. The wavelength of surface modulations should be much larger than the cavity mode. In the experiments substrates from *Layertec* have shown a good surface quality while substrates from *LASEROPTIK* although having comparable specifications showed large scattering losses and strong mode mixing.

Standard mirrors are designed such that the electrical field of the reflected light has a node at the surface. To bring samples to the field maximum and to profit from enhancement due to the standing wave inside a resonator, the mirrors used in this work have an additional, low refracting $\lambda/4$ thick spacer layer on top as discussed in the theory chapter 2.1.6.

As all measurements described in this work use the transmitted light through the plane mirror, it is desirable to direct most of the light, leaving the resonator, through this mirror. This can easily be achieved by choosing the transmission of this mirror larger than that of the fibre mirror.

In the experiments described in this works, two different mirror coatings have been used. The earlier coating was applied by *Layertec* by presumably magnetron sputtering. It has a transmission of 60 ppm at total losses of 34 ppm. The second coating was fabricated by *LASEROPTIK* by ion beam sputtering, which allows for lowest loss coatings. Here the transmission has been reduced to 30 ppm at total losses of 38 ppm.

3.2.8 Annealing

By annealing the ion beam sputtered coating, which means to slowly heat the mirror to 400 °C for 8 h under an air or oxygen atmosphere, the absorption loss can be reduced. During the the annealing process unoxidised parts of the coating can get oxidized and thus defects are reduced. So, the losses of a plane mirror could be reduced by 42 % to 16 ppm. Figure 3.11 shows the finesse of a mirror before and after annealing for both polarisations of the cavity and for different cavity length (for the method see section 4.2.2).

A comparable annealing process is in principle possible for the mirrors deposited on the fibre tips. As the copper coating withstands only temperatures up to around 150 °C without getting oxidised and thus making the fibre brittle, the fibre has to be heated very selectively only at its end facet. This has

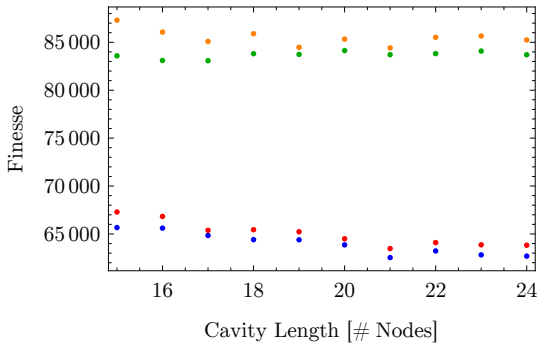

Figure 3.11: Finesse for different cavity lengths before (blue and red) and after (green and orange) annealing and for horizontal (blue and green) and vertical (red and orange) polarisation.

been tried by heating with an infrared halogen lamp. Figure 3.12 shows a section through the annealing device: a halogen rod lamp is imaged to the fibres, placed in a holding plate by an hollow elliptical mirror.

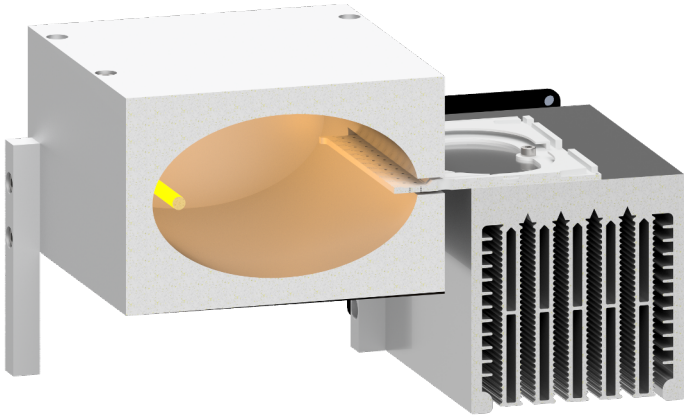

Figure 3.12: Section through the halogen rod lamp based annealing device. The lamp (left) is imaged with an hollow elliptical mirror to the fibre tips that are mounted to an holding plate. To avoid strong heating of the holding plate and thus the copper coating of the fibres, it is placed on a large heat sink equipped with a fan.

The temperature of the fibre should be measured by observing the temperature dependent shift of the first transmission maximum of the coating as marked in figure 3.13(a). This procedure has been tested at macroscopic mirrors with the same coating. The shift shows a certain hysteresis when heating up or cooling down the sample.

To control the temperature of the fibres during the annealing process directly, their temperature should be measured by observing the light of the heat lamp transmitted through the fibres. Due to the limited sensitivity of the spec-

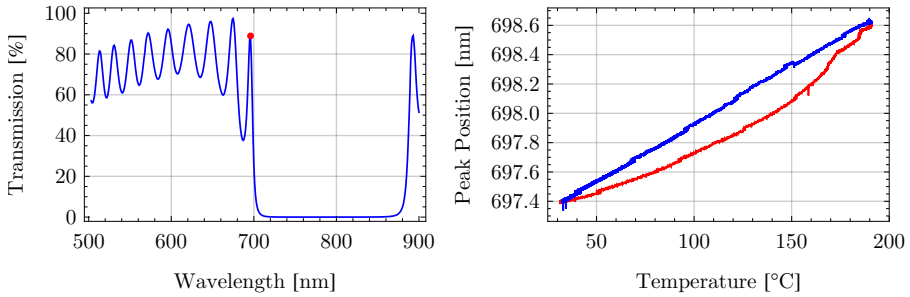

(a) Transmission spectrum of the mirror coating in the fibre measured at a macroscopic reference substrate. The first transmission maximum used for temperature measurement is marked red.

(b) Shift of the first transmission peak of the mirror coating depending on the sample temperature measured at a macroscopic sample at increasing temperature (red) and decreasing temperature (blue)

Figure 3.13: Temperature measurement of the coating by observing the shift of the first transmission peak.

trometer used and further problems with transfering white light with a single mode fibre, this approach has not succeeded yet [127].

3.3 Mechanical Setup

Setting up a scannable fibre-plane mirror cavity requires on the one hand a very stable mounting of the fibre with respect to the mirror, that allows to control the distance of fibre and plane mirror at the sub-nano metre scale. On the other hand, the plane mirror has to be movable over large distances in order to raster-scan the surface with the cavity mode. Good access to higher order modes requires easy angular alignment of the fibre.

The mechanical setup of the scanning cavity microscope shown in figure 3.14, where the main components are labelled with capital letters. The detailed mounting of fibre and plane mirror is shown in the figure 3.15, here the parts are labelled with small letters.

The fibre is clamped to a grooved steel plate ⓐ with a magnet (not shown). This steel plate is glued to a shear piezo chip ⓑ, that could be used for small length modulation. The fine length adjustment as well as length scans of the cavity (z axis) are done with a closed-loop controlled piezo actuator (*Physik Instrumente P-753.1 CD LISA*) Ⓐ. This positioning stage has a travel range of 15 µm at closed-loop resolution of 50 pm.

The angle of the fibre with respect to the plane mirror is aligned with a two-axes cross-roller supported goniometer (*MISUMI GPWG 50-68*) Ⓑ. The pivot points of both axes of the goniometer are very close to the fibre tip. This design makes it possible to align the angle of the fibre nearly without influencing the cavity length.

Coarse adjustment of the cavity length is done with a micrometre screw driven stage (*MISUMI XSG80-CZ-H*) Ⓒ with a travel range of 25 mm.

For changing the fibre, a part of the mounting column Ⓓ can be screwed of which provides good access to the fibre.

The plane mirror ⓒ sits in an interchangeable quadratic sample holder ⓓ that is tightly fitted to a sample mount ⓔ. The tight fit of the sample holder to its mount makes measurements of the mirror's surface before and after applying nanoparticles without changing the orientation of the mirror with respect to the scanning axes possible. The sample mount is designed such, that its centre of mass is in the centre of a piezo driven two-axes (x-y axes) scanning stage (*Physik Instrumente P-734.2CD*) Ⓔ. This stage has for both axes a closed-loop travel range of 100 µm at a closed-loop repeatability of below 2.5 nm.

For coarse positioning of the sample, the piezo scanner is mounted on a home-built stepper motor driven two axes stage based on a commercial cross table *OWIS KT150* Ⓕ. With this table, having a travel range of 20 mm × 20 mm, the sample can be moved out of the microscope for interchange. Furthermore, the stage enables an automatised stitching of multiple areas of the surface, that are covered by the piezo scanner. For absolute positioning without the need of reference drives, a laser, focused to a large area quadratic CMOS camera (*IDS UI-3370CP-M-GL Rev.2*) is used. This allows for a spatial resolution of around 2 µm.

All scanning tables as well as the baseplate Ⓖ have an aperture providing access to the light transmitted through the plane mirror. The collection optics is installed underneath the apparatus, thus the whole device is mounted on thick posts.

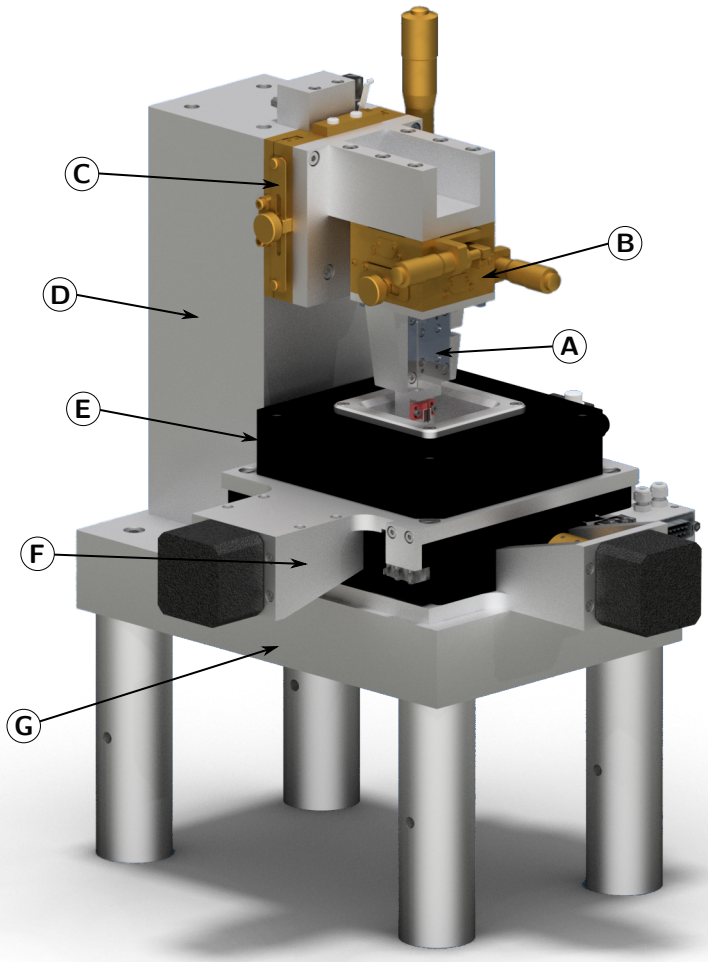

Figure 3.14: Mechanical setup of the scanning cavity microscope. Ⓐ Piezo stage for cavity length adjustment, Ⓑ Goniometer, Ⓒ Rough positioning stage for cavity length, Ⓓ Mounting column, Ⓔ Piezo scanner sample plane, Ⓕ Rough positioning stage for sample, Ⓖ Baseplate

To avoid acoustical noise to couple to the microscope and to excite vibrations, the device is designed to be as rigid and massive as possible. Furthermore, the setup is mounted to an individual breadboard (60 cm × 60 cm, *Thorlabs*) that is placed on a large and heavy floating optical table. At earlier stages of the experiment, additionally a bicycle tube was used for further vibration isolation. Due to the high centre of mass of the setup, the whole device tended to rolling movements cancelling the damping effect.

Acoustic noise as well as dust is shielded from the experiment by a noise damping box fitting around the breadboard made of special plywood with a cork core (*Rudolf Rost Polyvan-31*). To prevent dust from entering this box,

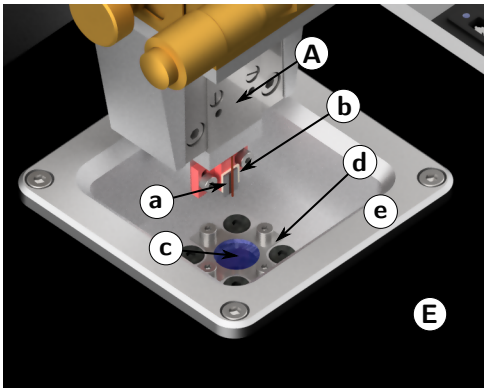

Figure 3.15: Detail view of the fibre mount and the sample. ⓐ Steel plate with groove for magnetic fibre clamping, ⓑ Shear piezo, ⓒ Plane mirror, ⓓ Sample holder, ⓔ Sample mount, Ⓐ Piezo stage for fine cavity length adjustment, Ⓔ Piezo scanner for sample

it is flushed with clean dry pressurized air, when the microscope is not active. The air flow is controlled by a magnetic valve by the experiment control.

3.4 Optics

For the scanning cavity microscope, different light sources are used : a laser at 780 nm, where the resonator has its highest finesse, probes the cavity's resonances and thus determines the extinction and dispersion of nanostructures. To stabilize the length of the resonator a laser at 970 nm is used. At this wavelength, the finesse of the cavity drops below 1, thus it isn't sensitive to absorbers any more. For measuring the length of the cavity, the resonator is illuminated by a superluminescent diode.

All three light sources are sent by fibre to a combination optic at the separate breadboard of the scanning cavity microscope. The transmitted light of the cavity is collected by an optical microscope, split up again and analysed with various detectors.

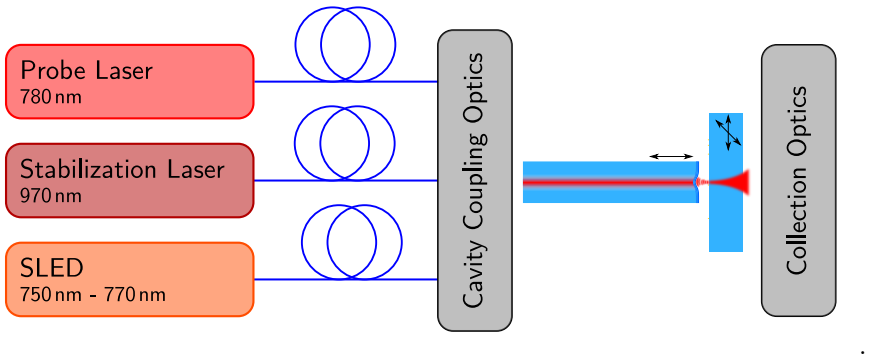

Figure 3.16: Schematic overview of the optical system of the scanning cavity microscope.

Figure 3.16 gives an overview of the optical system, all parts are discussed in the following.

3.4.1 Light Sources

Laser for Probing the Cavity

The probe laser system at a wavelength of 780 nm is shown in figure 3.17.

Laser The laser is a tunable external cavity diode laser using a diffraction grating in Littrow configuration as frequency selective element () *Toptica DL100*). The laser is protected from back reflections especially from the cavity by a two-stage Farady isolator (*Isowave I-50U-4*).

Electro Optics To precisely measure the linewidth of the cavity resonances in units of frequency, the laser gets phase-modulated with a free space electro-optic modulator (*Newfocus 4421*) at a frequency of 1.78 GHz. The RF-signal for the resonant modulator is synthesized with a frequency generator (*Rhode und Schwarz SMY02*) and amplified to a power of 30 dBm (*Mini-Circuits ZHL-42+*). To protect the amplifier from back reflections, especially if the modulator is not

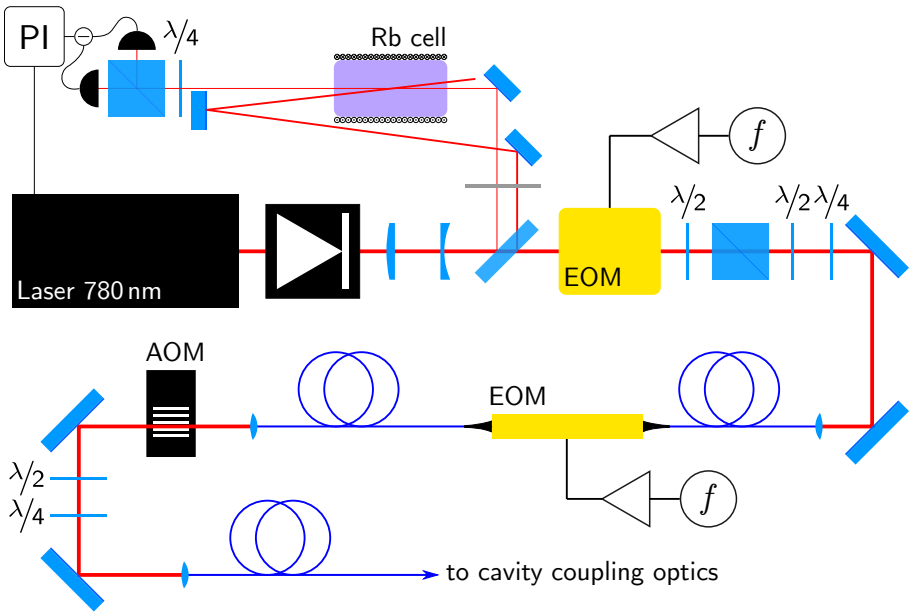

Figure 3.17: Probe laser system at 780 nm. The figure shows beam shaping optics, the electro optics for phase modulating the laser and at the upper part the DAVLL frequency lock.

driven at its resonance frequency, a circulator (*MECA CS-1.500*) is inserted between amplifier and modulator.

For measuring the dispersion of a particle, the shift of the TEM02 and TEM20 mode with respect to the TEM11 mode as depicted in figure 3.2 is used. Due to the ellipticity of the mirror on the fibre, these modes are split in the range of 100 GHz. To bring the lines closer together in order to avoid fluctuations especially du to mechanical noise, the laser is further modulated at high microwave frequencies. For economic reasons[3], a deep modulation to the 2nd order sidebands with suppression of the carrier at frequencies between 15 GHz to 40 GHz is used. The modulation is done with a fibre-coupled electro-optic modulator (*EOSpace PM-AV5-PFA-PFA-780SMP*), that can be used up to 40 GHz. The modulator is driven by a microwave generator (*WILTRON*[4] *68063B*). The signal is amplified (*CIAO Wireless CA3540-2030* (35 GHz to 40 GHz), *RF-Lambda RLNA 17-27 GHz*) and in order to protect the amplifier from back reflections fed via an isolator (*DITOM D3I2640* (26.5 GHz to 40 GHz), *DBwave PAIS15180026650A* (18 GHz to 26.5 GHz)) to the modulator. In contrast to the free-space resonant modulator, here the modulation frequency can be chosen freely.

Frequency Stabilization To avoid fluctuations and disturbances like mode mixing due to laser frequency drifts, the laser is locked to a rubidium D2 transi-

[3]EOMs and microwave electronics suitable for frequencies up to more than 100 GHz are available but extremely expensive.

[4]now Anritsu

tion using a Doppler-free dichroic atomic vapor laser lock (*DAVLL*) [128–130].

This locking technique is based on magnetically induced dichroism at a rubidium gas. In contrast to other locking schemes, that rely on frequency modulation of the laser [131] or at least the spectroscopy light [132], the DAVLL technique is very simple, robust and leaves the laser unaffected, which is crucial for probing cavity resonances.

Here, a magnetic field of approximately 22 G is applied along the optical axis by a solenoid directly wound onto the rubidium cell (^{85}Rb and ^{87}Rb, mixing ratio according to natural abundance). The magnetic field leads to a normal Zeeman-splitting of the Hyperfine levels into three states, absorbing (or emitting) right-hand circular polarized light (σ^-), linear polarized light (π) and left-hand circular polarized light (σ^+). While the π-state remains unshifted but having no emission or absorption along the magnetic field, the σ^-- and σ^+-state are symmetrically frequency shifted with respect to the initial state at zero magnetic field [133].

By shining in linear polarized light along the magnetic field axis, and analysing the absorption of both, σ^- and σ^+ light individually using a $\lambda/4$ plate and a polarizing beamsplitter with photodiodes at each exit port, an error signal with a zero-crossing at the original line position can be generated by subtracting the signal of one photodiode from the other.

The scheme is extended to a Doppler-free saturation spectroscopy using a counterpropagating pump beam that saturates the transitions such that for atoms with no velocity component along the beam axis the probe beam gets less absorbed [134].

Both, the pump- and the probe-beam are branched of just before the first EOM with a one-sided anti-reflection coated glass plate. The reflexes at both sides furnish two beams with a good power ratio for saturation spectroscopy. To profit from the high extinction of rubidium at low powers, the beams are further attenuated by a neutral density filter.

In general, the laser can be locked to any transition within the rubidium D2-line using a lock-box comprising a PI[5]-controller (*Anton Scheich: LB5*) to control the laser current (P signal) and the piezo voltage for adjusting the grating (I signal). As the presented experiments don't require a certain frequency but a stable one, the laser is locked to the $F = 2 \rightarrow F' = 2, 3$ cross over line, as this transition is the strongest one.

Power Stabilization To stabilize the laser power and to compensate power fluctuations due to the polarization maintaing transfer fibre (*Thorlabs PM780-HP*) to the fibre coupling optics, an acousto-optic modulator (*Crystal Technologies*[6] *3080-120*) is integrated. The power is controlled by deflecting a small portion of light out of the 0^{th} order beam. The reference signal comes from a photodiode (*Thorlabs PDA36A-EC*) at the fibre-couling optics just after the transfer fibre. The AOM is controlled by an PI-controller (*Anton Scheich: LB5*), where the P and I part are summed up to regulate the RF-power, driving the AOM. This stabilization scheme allows for a power stability of 10^{-4}.

For measurements only based on the linewidth and the line spacing of the cavity, intensity fluctuations don't matter. Especially for dispersion measure-

[5] Proportinal-Integral

[6] now Gooch and Housego

ments, highest available power at the 2nd order higher modes is more important than a stable power. So, the stabilization has been left off during these measurements.

Laser for Stabilizing the Cavity Length

For stabilizing the length of the cavity, a home-built diode laser [135] at a wavelength of 970 nm is used, the optical system is shown in figure 3.18. The wavelength has been chosen such, that the light is guided in single mode by the cavity fibre and that the finesse of the cavity is minimized. At such a very low finesse, the cavity transmission is barely influenced by nanoparticles on the plane mirror. Due to the small finesse on the order of 1, the transmitted intensity in dependence of the resonator length corresponds to an Airy-function. For the implemented electronic stabilization scheme, described in the following section 3.5.2, this is advantageous as only a small sampling rate is required to digitize and to process the signal. The laser is protected from back reflections

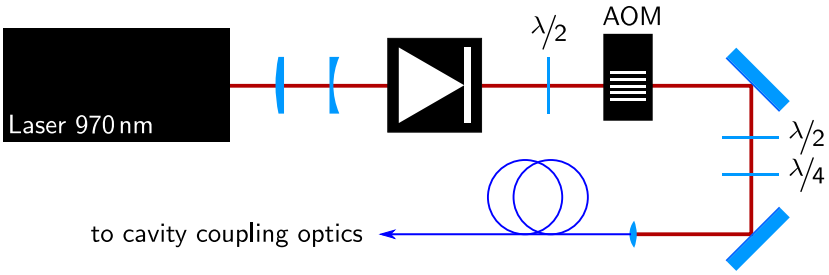

Figure 3.18: Cavity stabilization laser system at 960 nm.

with a Farady isolator (*Newport ISO-05-980-LP*). The power can be stabilized just as described above using an AOM (*AA Opto-Electronic AA.MTS.1200 10*) and a photodiode at the cavity coupling optics. The light is transferred to the coupling optics with a polarization maintaining fibre (*Thorlabs PM980-HP*).

Superluminescent Diode for Measuring the Cavity Length

To measure the cavity length spectroscopically, a superluminescent diode (SLED) is used. The SLED (*EXALOS EXS7505-8411*) is a broadband light source, centred around 760 nm with a 3 dB bandwidth of 20 nm. Although a SLED is a broadband source, it efficiently emits into the mode of a single mode fibre, it's coupled to. Figure 3.19 shows the optical system for the SLED.

As a SLED is mainly a laser diode that doesn't lase, as it has no internal resonator, it is very sensitive to back reflections. A double stage Farady isolator (*Gsänger*[7] *FR 780 TS*) protects the SLED from back reflected light.

The SLED emits unpolarized light. The polarization state is optimized and cleaned up with a λ/2-plate and a polarizing beamsplitter in front of the isolator. The light of the SLED is sent to the cavity coupling optics via a polarization maintaining fibre (*Thorlabs PM780-HP*).

[7] now Excelitas

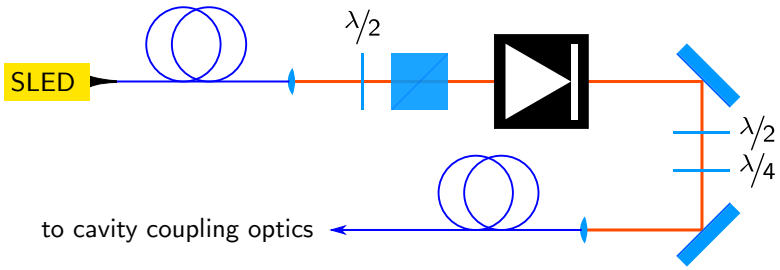

Figure 3.19: Superluminescent diode for spectroscopic cavity length measurement.

3.4.2 Cavity Coupling Optics

All three light sources described above have to combined and coupled to the cavity fibre. Therefore, the light is transferred to the breadboard the microscope assembly is mounted on. Figure 3.20 shows the optics on this breadboard. The

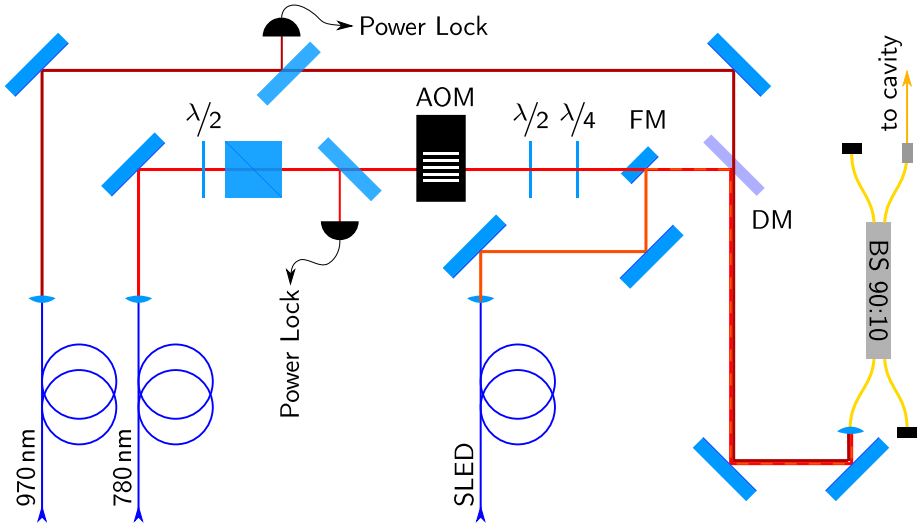

Figure 3.20: Optics for combining the light sources and for coupling them to the cavity fibre.

probe laser at 780 nm is coupled out the transfer fibre and its polarization is purified with a polarizing beamsplitter. A small fraction of light is branched of to a photodiode (*Thorlabs PDA36A-EC*) with a single side antireflection coated glass plate for power monitoring and as feedback for the power stabilization described above.

The coupling efficiency to the different orders of cavity modes strongly varies due to very different modematching between resonator mode and fibre mode. In order to optimally exploit the dynamic range of the digitizer and the photodetec-

tors, the laser power coupled to individual mode families is quickly modulated by an AOM (*Crystal Technologies 3080-120*).

After setting the polarization state of the light with a $\lambda/2$- and a $\lambda/4$-plate, the light is overlapped with the stabilization laser at a dichroic mirror (*Thorlabs DMLP900*).

The stabilization laser at 970 nm is also power monitored with an equivalent photodiode as the probe laser.

Both lasers are coupled to a 90:10 fibre-beamsplitter (*Thorlabs FC780-90B-APC*). The cavity fibre is attached to the output port with an FC/APC mating sleeve. The open ports of the beamsplitter are terminated with fibre beam dumps (*Thorlabs FTAPC1*). The beamsplitter allows for easy optimisation of the coupling of all light sources to the fibre and enables a better beam alignement leading to a much higher coupling efficiency compared to direct coupling to the cavity fibre, although 10 % of the light is branched of.

Instead the probe laser at 780 nm, the SLED for measuring the cavity length can be coupled to the resonator. A motorized flip mirror mount (modified *Radiant Dyes RD-KLS-1"-M*) allows to change between both light sources.

3.4.3 Collection Optics

The light transmitted by the cavity is collected with a long working distance microscope objective (*Mitutoyu M Plan Apo 20x*) and analysed. Figure 3.21 shows the corresponding optical system. To observe the position and the focus

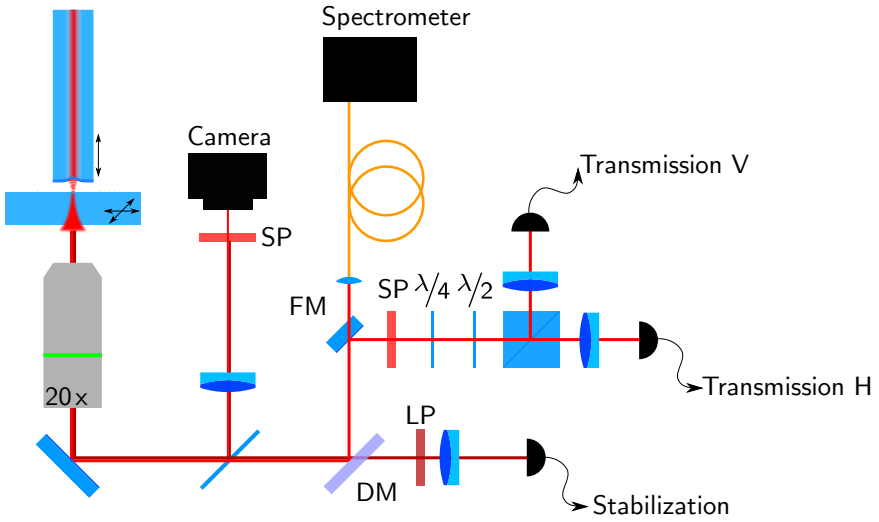

Figure 3.21: Optics to collect and analyse the transmitted light of the cavity.

of the collection optics relative to the cavity, a small portion of light is split of with a pellicle beamsplitter (*Thorlabs CM1-BP108*) and imaged to a CMOS camera (*IDS Imaging 1245LE-M*) with an achromatic lens (f=120 mm).

The stabilization laser is split of the probe light (laser at 780 nm or SLED) with a dichroic mirror (*Thorlabs DMLP900*). Probe light leaking through that

mirror is blocked with a longpass filter (*Thorlabs FEL850*). Finally, the stabilization laser is focused to a photodiode (*Thorlabs PDA36A-EC*).

The probe light can either be sent via a multimode fibre to a spectrometer or to polarization sensitive photodetectors by a motorized flip mirror (*OWIS KSHM 40*). The spectrometer (*Ocean Optics HR2000*) is used to observe the transmission of the light emitted by the SLED for determining the resonator length. To analyse the orthogonally polarized modes of the cavity, the light is split up according the two axes with a $\lambda/4$-, a $\lambda/2$-plate and a polarizing beamsplitter. Both channels are focused to fast and very sensitive non-counting avalanche photodetectors (*Thorlabs APD110A/M*) with a bandwidth of 50 MHz. The photodiodes are protected from residual light from the stabilization laser with a shortpass filter (*Thorlabs FES900*) before the polarization optics.

The implementation of photomultipliers (*HAMAMATSU microPMT H12403-01* with amplifier *C11184*) instead of the photodiodes in order to increase the detection sensitivity failed due to the strong non-linearity of the photomultipliers in the relevant high gain regime. For lower gains, where the photomultipliers work more linear, the gain is comparable to the used photodiodes.

The optomechanics of the collection optics system is based on a lens tube and cage system (*Thorlabs*), making a compact setup at very limited space possible. The compactness comes at the cost of low flexibility and accessibility of individual components. The whole optical system is mounted on a 3-axes positioner (*Newport ULTRAlign M-562-XYZ*) to align the optics with respect to the resonator for efficient light collection.

3.5 Experiment Control

In the previous sections, a large number of positioning stages for scanning the cavity length as well as for positioning the plane mirror with respect to the cavity fibre, and of detectors for measuring the transmitted light of the resonator for microscopy and stabilization have been introduced. All these components have to be operated and read out in a well coordinated way, while the large amount of incoming data has to be processed during the measurement to extract the information of interest. This chapter describes at first the electronics used to control the experiment and to digitize the measurement signals. The second part of the chapter elucidates the control, measurement and evaluation procedures implemented to the experiment control software.

3.5.1 Control Electronics

Centre piece of the electronics is a performant computer (*Fujitsu CELSIUS W520*) equipped with a 4 core processor (*Intel Xenon E3-1275 v2*). To this computer, all device controllers and digitizers are attached and controlled. Figure 3.22 shows all relevant components and their interconnection.

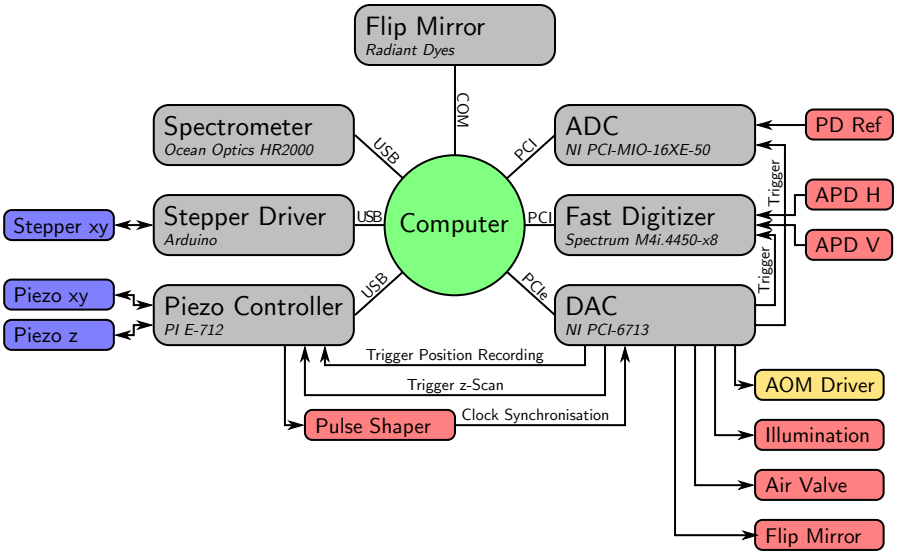

Figure 3.22: Control electronics of the scanning cavity microscope.

The signal from the photodiodes, detecting the transmitted probe light from the cavity is digitized using a fast (up to 500 MS/s) high resolution (14 bit) 2 channel digitizer card (*Spectrum M4I.4450-X8*) connected via the PCI Express bus to the computer. In earlier stages of the experiments, a high resolution (12 bit) digital oscilloscope (*LeCroy WaveRunner HRO 66Zi*) was used. As both digitizers have compatible properties, the replacement didn't affect the data quality.

The recording of the cavity stabilization signal requires a much lower sampling rate. Therefore a multifunctional PCI-based analogue to digital converter

(ADC) card with a sampling rate of 20 kS/s and a resolution of 16 bit is used (*National Instruments PCI-MIO-16XE-50*).

The piezo-based positioning stages (x-y scanning table and z-stage for cavity length) are operated by a digital closed loop controller (*Physikinstrumente E-712*). This device can individually control all three axes, generate scan pattern and record the positions by reading the capacitive position sensors of the positioning stages. The digital servo loop regulates the positions of each axis with an update rate of 50 kHz.

At each pixel of the microscope image, a length scan of the cavity in order to retrieve its transmission spectrum has to be precisely coordinated with the data taking as well as with the AOM used for modulating the power of the light, coupled to the cavity. Therefore a digital to analogue converter card (DAC) (*National Instruments PCI-6713*) is used to generate a 4-channel pulse pattern to trigger the different data taking devices and to control the AOM driver. This sequence is described in detail in the following section.

As the clock frequency of the piezo controller is much lower than the internal clock frequencies of the other devices, the clock of the piezo controller is used to trigger the actual trigger pattern to accurately synchronize the length scan and the data taking. The clock pulses of the piezo controller are converted to TTL-pulses accepted as a trigger pulse by the DAC by a circuit based on a retriggerable monoflop (*Texas Instruments 74LS123N*).

The controller of the x-y scanning table for coarse adjustment of the plane mirror is based on an Arduino nano micro controller. The stepper motors are addressed by two stepper motor drivers (*Allegro A4988*). Together with a camera and a laser for absolute positioning of the table as described above, it is possible to achieve an absolute positioning accuracy around 1 µm using a computer control relying on a LabVIEW-based software. Especially for the initial positioning of markers on the sample with respect to the fibre, a gamepad (*Microsoft Xbox 360*) facilitates the operation.

In addition, the DAC card comprises several digital input/output (IO) lines. These lines are employed for further control and automation of the experiment: the flushing of the noise isolation box around the microscope setup with clean dry air when no measurement takes place is controlled by a magnetic valve. The box is illuminated, when the stepper driven coarse positioning table is activated. To change between cavity transmission and length measurements using either photodiodes or a spectrometer, the flip mirror within the collection optics is controlled by the DAC card. The flip mirror at the input of the cavity, changing between the probe laser and the broadband light for length measurements, is controlled by the computer via a serial port. The spectrometer is read out by the computer via an USB interface.

3.5.2 Measurement Procedure

The images in scanning cavity microscopy are built up by probing the cavity and measuring its properties like amplitude, linewidth or spacing between certain modes at each pixel. The measurement scheme to acquire such an image is depicted in figure 3.23: after starting and initializing the measurement and its parameters like resonator length and spacing between each data point, the first field of interest on the plane mirror is approached by the stepper-driven scanning table. Than, the cavity length is measured to ensure, that the measurements are

done at an optimal cavity length in order to avoid mode mixing. At each pixel, addressed by the piezo scanning table, the cavity is probed an the properties of each resonance, like linewidth, position or amplitude, are measured. The crucial steps of the protocol, the cavity length measurement and the spectroscopy of the cavity resonances in transmission at each pixel of the microscope image including the length stabilization mechanism, will be discussed in the following section.

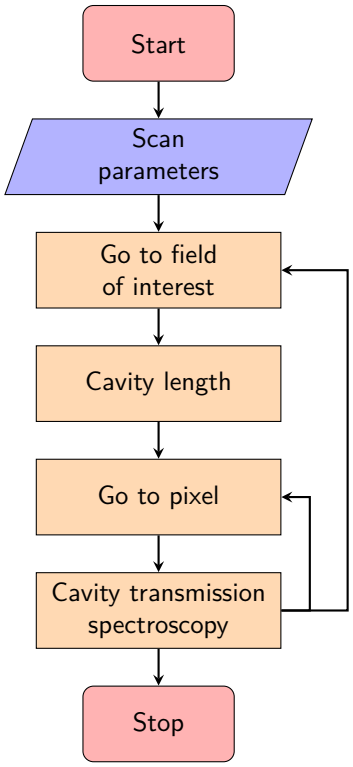

Figure 3.23: Overview of measurement procedure.

A typical scanning cavity microscope image covers an area of 100 µm × 100 µm with a pixel spacing of 0.2 µm. Because of the large number of 250 000 pixels, the time required to measure one pixel is crucial. The whole procedure is optimized to minimize the measurement time (200 ms to 250 ms per pixel for a measurement including the first 3 orders of modes). To reduce the positioning time, all data points lie on a meandering path. The data evaluation profits from parallel computing to further shrink the measurement time.

The computer control of the experiment has been implemented in LabVIEW[8]. Especially LabVIEWs intrinsic capability of parallelizing computation tasks turned out to be very advantageous for the work in hand.

[8]A graphical programming environment dedicated to lab automation applications developed by National Instruments.

Cavity Length Measurement

The measurement of the length of very short cavities profits from their large free spectral range (20 THz corresponding to 37 nm at a wavelength of 780 nm for a cavity length of 20 antinodes) and a strong dependence of the resonance wavelength λ_{res} to the cavity length ($\lambda_{res} = {}^{2\,d}/_{q}$, where q is the number of antinodes and d the cavity length) which can easily be resolved with a spectrometer, if the cavity is illuminated with spectrally sufficiently broad light. In this case, the resonator can be seen as a narrowband spectral filter that is only transparent at wavelengths corresponding to resonances associated to the cavity length as depicted in figure 3.24.

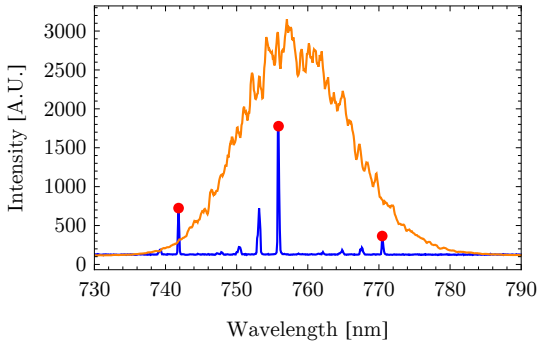

Figure 3.24: Transmission spectrum of a cavity (blue). 0^{th} transversal order resonances are marked red. For comparison to the peak amplitudes, the spectrum of the SLED is shown (orange).

In the scope of this work, length measurement schemes based on both effects have been implemented and are discussed in the following.

Length from the Free Spectral Range The length of a cavity can be calculated from the resonance frequencies or wavelengths λ and λ' of two resonances of the same transverse but subsequent longitudinal order as illustrated with red dots in figure 3.24 by

$$\frac{1}{2\,d} = \left| \frac{1}{\lambda} - \frac{1}{\lambda'} \right| . \tag{3.3}$$

This relation follows from the general resonance condition $d = q \cdot {}^{\lambda_q}/_{2}$ (c.f. equation 2.52), where q is the number of antinodes of the field inside the cavity and λ_q the corresponding wavelength.

This method requires nothing than the transmission spectrum of the resonator showing two subsequent resonances of the same order, which makes it to a very universal tool for length measurement.

The simplicity of this technique comes with some drawbacks: For high reflectivity dielectric mirror coatings as used in the experiments in this work, the reflectivity and thus the penetration depth of the light field within the coating varies with the wavelength. As the free spectral range is large and as here, the spectral centre of the spectroscopy light source is approximately 20 nm away from the coating's design wavelength, the cavity is probed at at least at one

point, where the reflectivity and thus the optical penetration depth into the coating have changed significantly. Hence the measured cavity length is only an approximate value to the real length at the probe laser wavelength.

Due to the limited spectral width of the light source, it is challenging to automatically detect the right resonances. This can be faced by considering the spacing between the modes in order to assign each peak to the right longitudinal and transversal mode order. When the free spectral range comes close to the bandwidth of the light source for short cavities or if many higher transversal order modes are excited, a reliable automated evaluation of transmission spectra is not feasible any more.

Length from the Shift of the Resonance Frequency To overcome especially the problem of the penetration depth, which in principle could be faced by an extended modelling of the mirror coatings, by a direct measurement, a second method to determine the cavity length has been implemented. This technique relies on the shift of the resonance frequency or wavelength λ_{res} at a fixed longitudinal order q when modulating the resonator length d:

$$d + \delta d = \frac{q}{2} \left(\lambda_{res} + \delta\lambda \right). \tag{3.4}$$

If the cavity length is stepwisely adjusted and the resonance wavelength starting at the wavelength of interest is recorded, the resonator length can be determined from the slope of the arising line. This method requires a very precise and quantitative length adjustment, which is provided by the closed loop z-positioning stage. Due to the integrated position sensor, a reliable positioning reading on the 50 pm level is possible.

The implementation of this scheme is more elaborate than the free spectral range approach, where it is sufficient to evaluate a single transmission spectrum. At first, the starting point for the length modulation where the resonance frequency of the cavity is very close to the probe laser wavelength has to be found. Therefore the cavity length is scanned in small steps of 2 nm over a bit more than one geometric free spectral range equal to $\lambda/2$, starting at first with the fully retracted actuator in order to avoid any crashing of the fibre to the plane mirror. At each step, a transmission spectrum is taken and the amplitude at the probe laser's wavelength is recorded. The actuator's position at the highest transmission, where the fundamental mode at the probe wavelength is resonant, is taken as a starting point for the next step. Again the cavity length is scanned, here in 50 steps of 2 nm. Now, the position of the transmission peak which is at the beginning closest to the probe laser wavelength is tracked and recorded in dependence of the actuator's position. From the slope of the arising line, the cavity length is calculated as described above. In order to reduce the error by averaging and to compensate for tracking failures, the second step is repeated 20 times.

As the slope of the peak position with respect to the resonator length is steeper for shorter cavities, the measurement is repeated for the shortest cavity possible that is on the one hand reachable with the positioner and that on the other hand safely avoids touching the plane mirror with the fibre. This increases the measurement accuracy, which is important to set the appropriate cavity length for the actual scanning cavity imaging.

Cavity Transmission Spectroscopy and Stabilization

At each pixel of the microscope image, the cavity is probed in order to measure its optical properties and eventually the influence due to nanoparticles. To do so, the cavity length is scanned over one free spectral range to excite the fundamental and higher order transversal modes. The transmission signal is recorded and directly evaluated. The simultaneously measured resonance of the stabilization laser is used to keep the cavity length constant and to compensate for non-planar scanning and drifts.

Data Acquisition After commanding the piezo scanning table to the appropriate pixel and ensuring, that the positioner has arrived at the target position, the length scan of the cavity and the data acquisition is initiated by a pulse sequence. This pattern, shown in figure 3.25(a), is generated before the scanning microscopy starts, as the pattern doesn't change during scanning.

While the time between the trigger pulse for the ramp and the data taking for position and stabilization laser is fixed, the timing of the trigger for the recording of the cavity transmission of the probe laser depends on the experimenter's choice for cavity length and on the number of transversal modes to measure. It is calculated from the frequency spacing of two subsequent transversal mode orders $\Delta\nu = \nu_F \left[2\Delta\zeta/\pi\right]$ with the Gouy-phase $\Delta\zeta$ following from equation 2.84 and the time to sweep over one free spectral range.

The same ansatz is used to initialize the voltage pattern to control the AOM for switching the cavity input power. The amplitudes of each voltage step are adjusted such that the amplitudes of the resonances are as equally high as possible. This is illustrated in figure 3.25(c).

To modulate the length of the cavity, the piezo stage performs a triangular movement pattern as shown in figure 3.25(b). The graph shows the position of the piezo stage measured by its internal sensor, the expansion of the positionier as depicted leads to a reduction of cavity length. The scanning pattern has an amplitude of 500 nm. The slope is chosen as steep as possible to avoid individual cavity resonances getting affected by acoustical noise. Furthermore the slope is flat enough, that the bandwidth of the transmission peaks of the probe laser is well below the bandwidth of the photodetectors and that the piezo controller can follow the linear ramps except at their starting- and turning points. The offset of the ramp is set to address a chosen longitudinal mode order. The offset is initially calculated from the measured cavity length and the chosen number of antinodes and continuously adjusted during scanning by the cavity length stabilization, as described in the last part of this section.

In order to reduce the acquired amount of data and thus to minimise the readout and evaluation time, the position of the piezo stage, the transmission of the stabilization laser as well as the transmission of the probe laser are only recorded at shortest possible parts of the positive flank of the cavity scan as illustrated in the subfigures 3.25(b) and 3.25(c).

Data Evaluation For measuring the polarizability tensor of nanoparticles, many parameters have to be extracted from the cavity transmission signal. For extinction measurements, the linewidth and amplitude of the fundamental mode has to be determined. To enhance the spatial resolution by higher order modes,

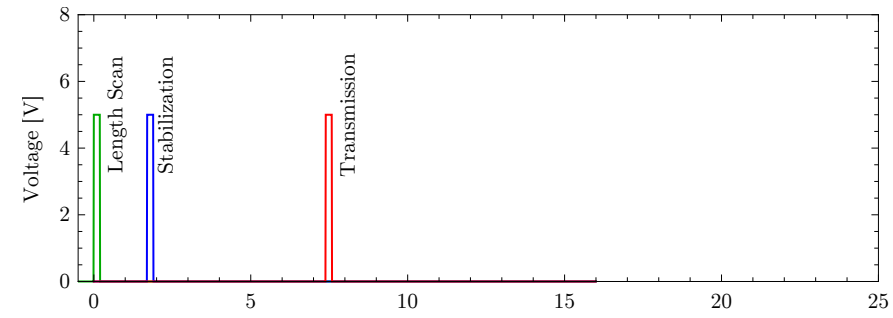

(a) Trigger pattern

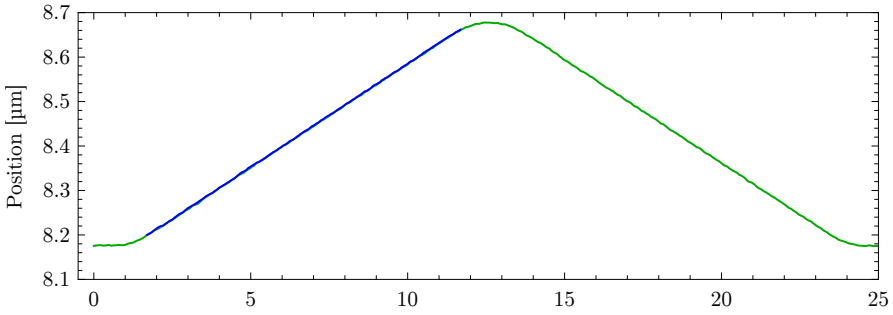

(b) Cavity length scan: movement of the positioner (green) and recorded position (blue).

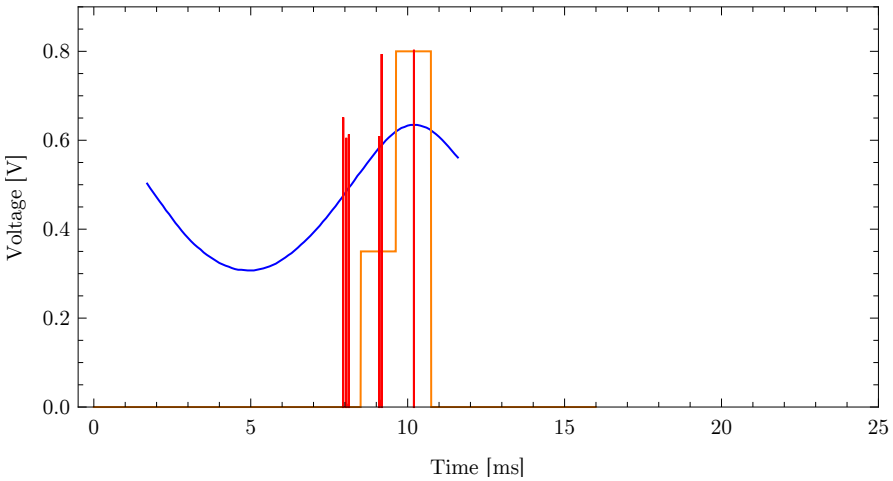

(c) Cavity transmission signals: stabilization laser ($\times 5 - 0.5\,\mathrm{V}$, blue), power switching pattern (orange), probe laser (red).

Figure 3.25: Timing of the measurement process at one pixel. The three plots show (a) the trigger pulses for the length scan (green), the recording of the position and the cavity transmission of the stabilization laser (blue) and for the transmission signal of the probe laser (red); (b) the movement of the positioner (green) and the recorded position signal (green); (c) the cavity transmission signals of the stabilization laser (blue) and the probe laser (red) as well as the voltage pattern for switching the probe laser power (orange).

also from these modes amplitude and linewith have to be evaluated. To measure the dispersion due to a particle, the spacings between the TEM11 and TEM02 and TEM20 mode respectively have to be determined. For measuring the particle's optical properties along two axes, all the mentioned quantities are measured for both orthogonally polarized eigenmodes of the cavity. Further more, the frequency spacing between each orthogonally polarized mode is measured to learn about the birefringence of the investigated particle.

To avoid the need of storing large amounts of cavity transmission data, each transmission spectrum is directly evaluated and only the mentioned quantities are stored for further evaluation.

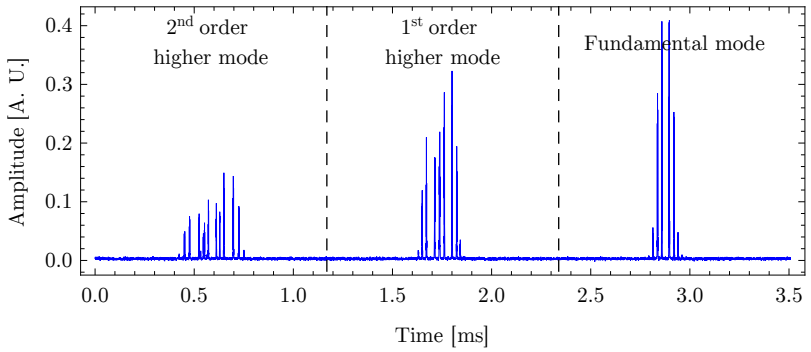

Figure 3.26: Recorded transmission signal of the cavity including all sidebands. For clarity, only the signal corresponding to one polarization is shown. For further processing, the signal is split up along the dashed lines.

Figure 3.26 shows a typical transmission signal of the cavity. In the figure, the high frequency sidebands, here at a modulation frequency of 37 GHz, are clearly visible. The modulation depth is chosen such, that the carrier is fully suppressed, which serves as a marker for the line centre for the evaluation. Each peak visible in the figure is again split up into a multiplet of lines due to the low frequency modulation of the probe light. The modulation depth of the low frequency modulation is adjusted such that the sideband amplitude is close to the amplitude of the carrier. This low frequency splitting is more clearly visible in figure 3.27. In contrast to the first graph, this figure shows the signals from both detectors recording the two orthogonally polarized cavity modes.

As the different mode orders furnish various information, they are evaluated individually using algorithms optimized for the respective order. To save computation time, this is done in parallel. To speed up the preprocessing of the data, the incoming transmission data is decimated. Only the actual fitting of the resonances is done with the original sampling rate of 125 MS/s.

In the following, typical signals of the first three transversal mode orders are shown and the evaluation strategy is discussed.

Fundamental Mode The first step at the evaluation of the resonances of the fundamental mode is a peak detector, that gives the positions and amplitudes of each resonance. By analysing the spacings between subsequent peaks, the two multiplets of resonances next to the suppressed carrier of the high

frequency sidebands are selected as illustrated by the green shaded stripes in figure 3.27. At each multiplet, the highest peak is associated to the carrier of

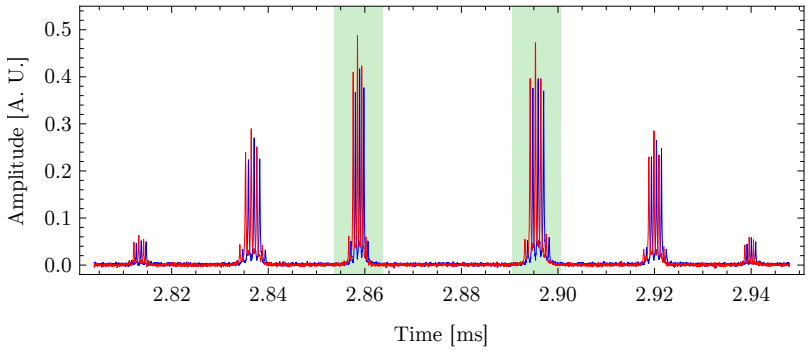

Figure 3.27: Transmission signal of the fundamental mode for both polarizations (red, blue). The two triplets of peaks within the green shaded areas are evaluated.

the low frequency sidebands. To the carrier and the two neighbouring peaks, a sum of three Lorentzians with equal width, $f_{fit}(x) = \sum_{n=0}^{2} a_n \frac{\left(\frac{\Gamma}{2}\right)^2}{\left(\frac{\Gamma}{2}\right)^2+(x-x_n)^2}$, is fitted using the nonlinear curve fitting package of LabVIEW based on the Levenberg-Marquardt algorithm [136, 137]. Figure 3.28 shows the adjustment of this function to the measured data (blue). The starting parameters stem from the results of the peak detector (green). The fitted function (red) and the residuum (orange) illustrate the good agreement of data and model. To reduce the computation effort, the data range is chosen as small as possible. From the fit parameters, namely width and positions of the peaks in units of

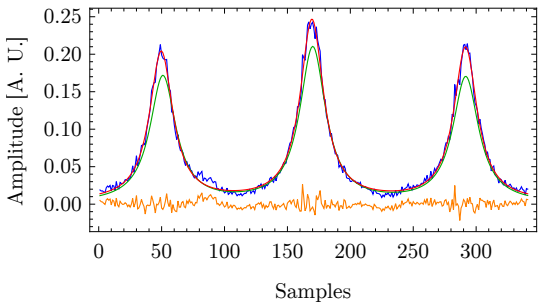

Figure 3.28: Fitting of a triplet of resonances. Data (blue), initial parameters of the fit function (green), the fitted triple Lorentzian (red) and the residuum (orange).

samples and the knowledge of the lower modulation frequency, the linewidth of the resonance in units of frequency is calculated. By comparing the positions of the peaks for both polarizations and from the lower modulation frequency the shift between the orthogonally polarized modes is deduced. The interpolated

position sensor signal and the average position of the peaks allow to localize the cavity resonances with respect to the positioner.

Finally, the average amplitude, linewidth, position and spacing between the orthogonally polarized modes of the two evaluated triplets of resonances are stored to a matrix forming the microscope images.

First Order Higher Modes To analyse the TEM01 and TEM10 mode, the first step is again a peak detector to get the positions of each resonance. To avoid disturbing effects on the measurement due to mixing of the two modes because of to the overlapping sidebands in the middle, only the resonances away from the centre are taken for evaluation as depicted in figure 3.29. The marked

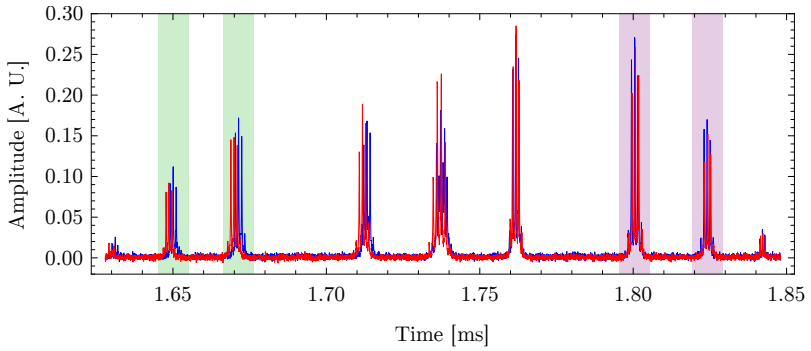

Figure 3.29: Transmission signal of the first higher mode for both polarizations (red, blue). The four triplets of peaks within the green and purple shaded areas corresponding to the TEM01 and TEM10 mode respectively are evaluated.

multiplets of resonances are evaluated in the same manner as described above by fitting a sum of three Lorentzians. For each mode, amplitude, linewidth, position relative to the positioner and the frequency spacing of the two orthogonally polarized modes are stored.

Second Order Higher Modes At the analysis of second order of higher transversal cavity mode, besides the quantities introduced so far, a new feature to measure comes into play: the precise measurement of the frequency spacing between the three modes. Therefore, the high frequency modulation of the probe light in order to generate sidebands to brige the large spacing between the modes has been introduced. The modulation frequency is set to bring the second sidebands of the TEM02 or TEM20 mode as close as possible to that of the TEM11 mode or even to overlap the resonances. These overlapping resonances are highlighted in orange in figure 3.30.

The bring order to this confusing bunch of modes, again the spacing between the resonances is analysed. Compared to looking at amplitudes, the position is more stable, as the amplitudes vary due to different coupling to the individual modes and due to extinction at nanoparticles.

At first, the two multiplets of resonances next to the suppressed central carrier, highlighted in green in figure 3.30, are evaluated by fitting a sum of

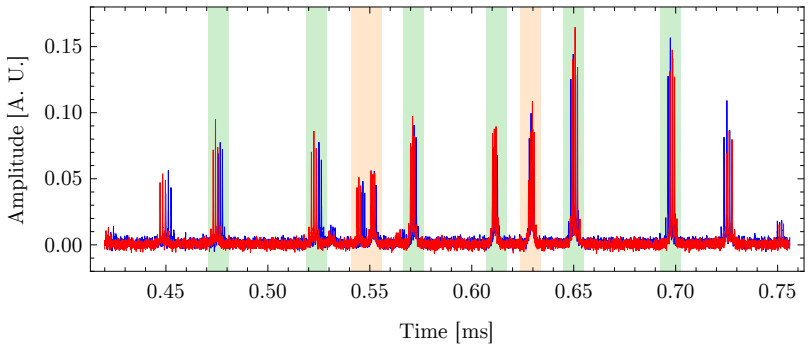

Figure 3.30: Transmission signal of the second higher mode for both polarizations (red, blue). The triplets highlighted in green are used to measure the properties of each mode, the resonances marked in orange provide the spacing between the TEM11 mode in the centre and the TEM02 and TEM20 modes respectively.

three Lorentzians as described for the fundamental mode to get information about amplitude, linewidth and position of the mode.

In a next step, the overlapping resonances of neighbouring modes are analysed. If the two multiplets are still sufficiently far apart from each other to be assayed separately, the multiplets are fitted just as before. From the positions of the outermost lying resonances, the spacing of the peaks within one multiplet and the lower modulation frequency, the spacing between the neighbouring modes is calculated.

If the second order sidebands of two neighbouring modes overlap, the arising mode pattern is fitted at once. The fit function

$$f_{fit}(x) = \sum_{n=0}^{2} a_n \frac{\left(\frac{\Gamma_l}{2}\right)^2}{\left(\frac{\Gamma_l}{2}\right)^2 + (x - x_l - n s_l)^2} + \sum_{n=0}^{2} b_n \frac{\left(\frac{\Gamma_r}{2}\right)^2}{\left(\frac{\Gamma_r}{2}\right)^2 + (x + x_r + n s_r)^2} \tag{3.5}$$

is set up by two sums over three Lorentzians corresponding to the carrier and its two low frequency sidebands. The positions of the outermost peaks, x_l and x_r serve as anchor points. The positions of the other peaks are described by their spacing s_l and s_r to the outer peak. The starting values for s_l and s_r are retrieved from the fit of the respective neighbouring first order high frequency sideband at the first evaluation step. The amplitudes for the first and third peak of each triplet is set to be equal. As starting values, the amplitudes of the first two peaks from the left and the right are taken. Although the starting values for the fitting procedure might be a bit off the real values as depicted in figure 3.31 (green curve), the fit (red) converges very good to the data (blue).

From the positions of the outermost peaks, the spacing between the peaks and the lower modulation frequency, the spacing between the neighbouring modes is calculated just as above and stored to a matrix to build the microscope image corresponding to the dispersion of the nanoparticles on the plane mirror.

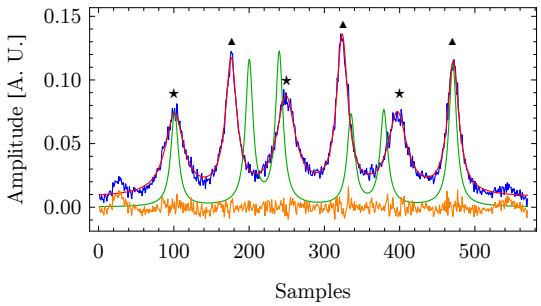

Figure 3.31: Fitting of two overlapping triplets of neighbouring resonances to determine their spacing. Data (blue), initial parameters of the fit function (green), the fitted sum of Lorentzians (red) and the residuum (orange). Resonances of the same mode are marked with ★ and ▲ respectively.

Cavity Length Stabilization To keep the length of resonator stable, especially to avoid a jump of the longitudinal mode order and to prevent a resonance falling out of the narrow detection window, a digital control loop is used. This loop relies on the resonances of the stabilization laser at wavelength where the finesse of the resonator has dropped below 1. Thus it is very insensitive to absorbers on the plane mirror and gives still a signal also when the transmission of the probe laser has dropped to zero.

As reference quantity for stabilization the relative position of the peak or valley of the lock laser transmission signal, that appears closest before the fundamental mode when scanning the cavity length is used. This position is calculated at the beginning of the measurement sequence. Compared to classical reference signals, like the side of fringe, the peak/valley method is insensitive to fluctuations of the amplitude of the lock signal. This is especially important as the signal might vary due to absorbers. Furthermore, the modulation depth and the lock signal amplitude varies with the cavity length, which make an amplitude independent stabilization procedure desirable.

To stabilize the cavity length, the actual relative position of the peak or valley of interest of the lock laser, detected by a peak detection algorithm coming with LabVIEW is compared to the calculated set point leading to an error value. Using a digital PID[9]-control loop, the position deviation is compensated at the next pixel of the scanning image by shifting the offset of the cavity length scan ramp.

The stabilization profits from the continuous meandering scan path with equally small steps. This makes it possible to stay in lock during the whole scanning process without the need for further stabilization techniques.

[9]Proportional-Integral-Differential

Chapter 4

Measurements with the Scanning Cavity Microscope

4.1 Introduction

To test the capability of the scanning cavity microscope introduced in the previous chapters for spatially resolved measurements of the optical properties of individual nanoparticles, measurements on differently sized and shaped gold particles have been performed. This chapter presents the results of these measurements, proving the ability for quantitative extinction and dispersion of the microscope.

Gold particles were chosen as a testbed, as they have well understood and calculable optical properties. The microscope is operated in the near infrared at 780 nm while the plasmon resonance of gold is located in the green. Thus, the extinction cross section of gold particles in the near infrared has dropped by two and a half orders of magnitude compared to the green as shown in figure 4.1.

Testing the microscope with gold nanoparticles far away from the plasmon resonance is advantageous compared to measurements close this resonance as the particles are still sufficiently large to detect them by complementary methods like scanning electron microscopy or dark-field microscopy.

Furthermore, colloidal suspensions of gold particles of well defined shapes and sizes are easily commercially available due to their wide-spread applications in science [138].

The measurements shown within this chapter are ordered chronologically starting with extinction measurements on 40 nm gold nanospheres. Higher order modes have been used to significantly enhance the spatial resolution of these measurements.

Gold nanorods introduce asymmetry to the cavity: with these particles, for the first time the splitting of each cavity resonance to orthogonally polarized modes has been exploited. The contrast of extinction for both polarizations has

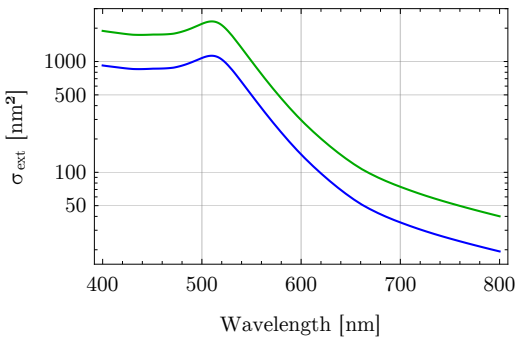

Figure 4.1: Extinction cross section σ_{ext} of gold nanospheres on a fused silica mirror surface of diameter 40 nm (blue) and 50 nm (green) as used in the experiments.

been observed. Furthermore, the birefringence and the effect of the particles on the cavity's polarization state have been investigated.

The last result of the work has been a measurement of the polarizability of 50 nm gold spheres. Therefore, an extinction and a simultaneous dispersion measurement using the 2^{nd} order higher transversal modes have been performed. By combining both measurements, the complex polarizability of the particle determining its optical properties could be quantified.

4.2 Extinction Measurements with 40 nm Gold Spheres

4.2.1 Sample Preparation

In the scanning cavity microscope, the optical resonator to probe the nanoscaled sample is set up of a microscopic mirror on the endfacet of a fibre and an extent plane mirror that serves at the same time as a sample holder. The nanoparticles have to be brought to the mirror without contaminating it by dirt coming from the suspending liquid or the ligands inhibiting the aggregation of the particles.

The particles, here gold spheres with a mean diameter of 41.1 nm with a variation of 8 % in colloidal suspension[1] with a concentration of 9×10^{10} particles/ml were spin-coated to the plane mirror. To adjust the particle concentration, the suspension was diluted py 33 parts of double distilled water.

100 µl of the diluted suspension were dropped to the slowly rotating mirror at the spin coater. After 30 s, when sufficient particles have settled to the mirror surface, the rotation speed was cranked up to 2000 rpm and the the remaining liquid was centrifuged off.

To find a good particle density, the spin coating process eventually has to be repeated until a good particle density is achieved.

Optimizing the particle concentration by spin coating them to other, cheaper substrates like microscope cover slips can be delusive. Different substrates carry different surface charges, the particles are also charged [139] thus the adhesion of the particles to the substrate strongly varies. The same suspension of particles leads to very different particle densities on various substrates.

To check the particle density on the plane mirror and to prove that individual particles were deposited, the mirror was investigated with a scanning electron microscope (SEM) after the scanning cavity microscopy measurements. Therefore, a nanometre-thin chromium layer was deposited on the mirror which destroyed the sample for further scanning cavity measurements. Figure 4.2 shows the SEM image where a sparse distribution of individual particles is visible.[2]

Gold particles can be removed by dissolving them with Lugol's iodine, a solution of potassium iodine with iodine in water [140]. For further cleaning, spin cleaning[3] with ultra clean water and ethanol can be used. In addition, collodion, a solution of nitrocellulose in ether and ethanol, can be applied to the mirror surface. When the collodion dries, it forms a film, binding the dirt, that can be pulled of the mirror with tweezers or an embedded piece of cloth.

The described methods are the least worse working ones among many other tested techniques and materials like ultrasonic cleaning. In general, any cleaning method cannot restore the initial cleanness of a new mirror.

4.2.2 Calibration and Characterisation

Before starting the actual microscopy measurement, the cavity should be characterized. To convert cavity transmission and linewidth to the extinction of the

[1] BBI Solutions Gold colloid - 40 nm EM.GC40, Batch 14387

[2] The author thanks Quirin Unterreithmeier for performing the SEM measurements.

[3] A cleaning procedure where the quickly rotating sample is flushed with diverse solvents. Due to the fast rotation, the sample is dried by centrifuging off the solvent together with potential dirt.

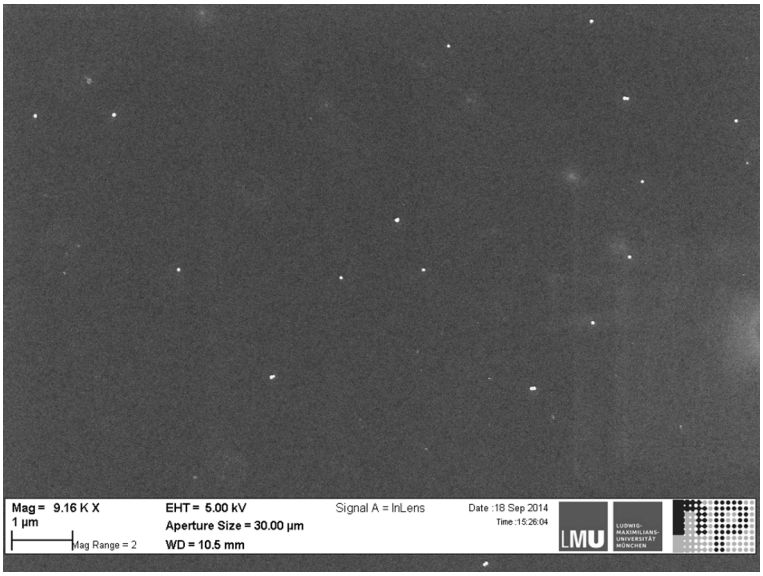

Figure 4.2: SEM image of the mirror with individual gold nanospheres used in the experiments described in this section.

nanoparticles, precise knowledge of the actual mirror parameters and the finesse are necessary. Furthermore, a suitable longitudinal mode order has to be found at which the modes used for the measurement don't mix and thus disturb the imaging.

To identify a good longitudinal mode and to measure the finesse, small scanning cavity images with a size of 10 µm × 10 µm are taken for subsequent longitudinal mode orders as shown in figure 4.3. The wormy structures as well as a wavy background at certain longitudinal modes come from mode mixing. For the actual microscopy, a order with no mixing is chosen by eye, here order 33.

To prove the mirror coating specifications, the mean linewidth of each longitudinal mode is measured and compared to the calculated linewidth (c.f. equation 2.2.1) of the resonator using the mirror specifications. Figure 4.4(a) shows the linewidth of the two orthogonally polarized fundamental modes of the cavity in comparison to the parameters of the mirror on the fibre (fibre 17-5, effective radius of curvature around 60 µm, transmission 12 ppm, losses 12 ppm) and the plane mirror (coating and substrate from *Layertec*, transmission 60 ppm, losses 34 ppm). Figure 4.4(b) shows the resulting finesse of both fundamental modes in comparison to the expected value. Both modes show slightly different losses, thus the finesse of one mode is a bit above, that of the other mode is a bit below the specified value. For the further evaluation, the value given by the mirror parameters for a finesse of 53 247 is used.

4.2.3 Extinction of Gold Nano-Spheres

To measure the extinction cross section of a large number of gold nanospheres in order to reproduce the distribution of particle sizes, 24 areas of 100 µm × 100 µm

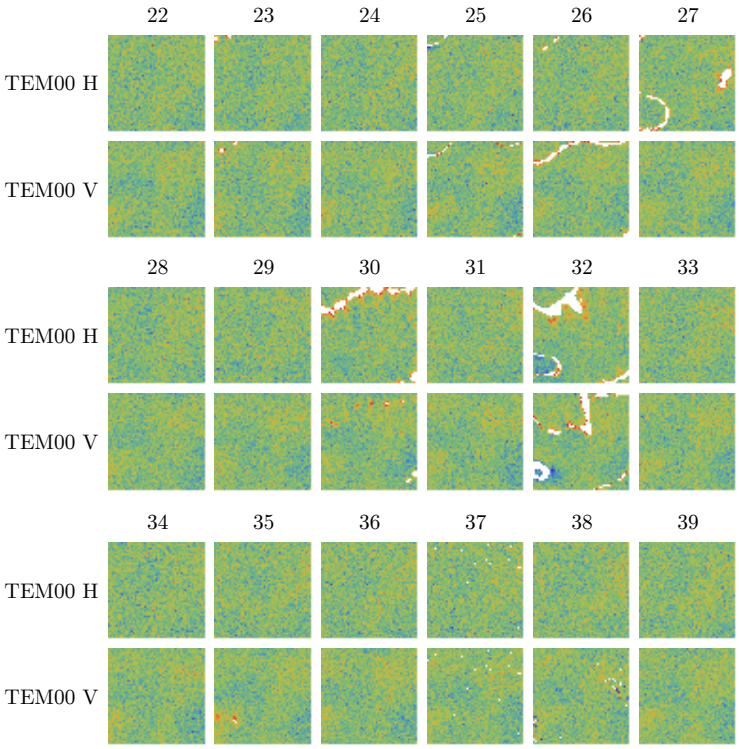

Figure 4.3: Scanning cavity microscope images of the normalized and standardized linewidth of the fundamental mode (TEM00) for subsequent longitudinal mode orders (22 – 39) for both polarizations (H, V). Image size is 10 µm × 10 µm, the pixel size 0.2 µm × 0.2 µm.

were scanned with a pixel size of 0.5 µm × 0.5 µm. Figure 4.5 shows images of the scanned surface already converted to units of extinction cross sections. For all measurements shown in this section, the signals coming from the two orthogonally polarized modes of the cavity have been averaged. The wavy structure of the background of the images, visible in figure 4.5(b) is attributed to mode mixing.

For converting the measured cavity transmission $T_{cav,meas}$ to extinction cross sections σ_{ext} of particles on the plane mirror, the transmission amplitude $T_{cav,meas}$ is normalized with respect to the most probable transmission value $T_{prob,max}$ and multiplied with the transmission of an empty cavity

$$T_0 = \frac{2T_1T_2}{(T_1 + T_2 + L_1 + L_2)^2} \tag{4.1}$$

using the mirror parameters (transmission T_1, T_2, losses L_1, L_2) determined above.

$$T_{cav} = \frac{T_{cav,meas}}{T_{prob,max}} \cdot T_0 \tag{4.2}$$

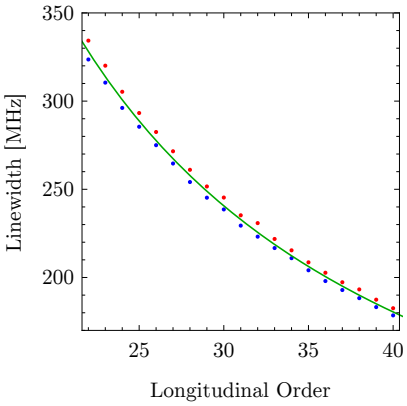

(a) Linewidth of the cavity depending on the longitudinal mode order.

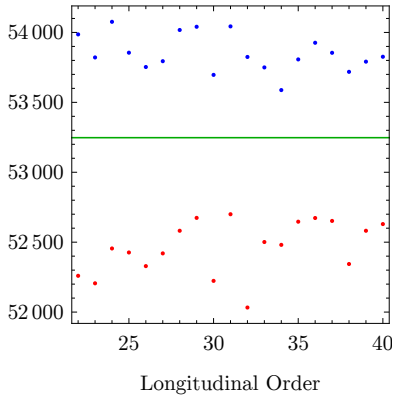

(b) Finesse of the cavity depending on the longitudinal mode order.

Figure 4.4: Linewidth and finesse of the two orthogonally polarized fundamental modes (H: red, V: blue) of cavity for different longitudinal modes in comparison to the specified values (green).

By solving the equation for the cavity transmission (c. f. equation 2.60)

$$T_{cav} = \frac{2T_1T_2}{(T_1 + T_2 + L_1 + L_2 + 2L)^2} \tag{4.3}$$

for the additional cavity losses L, the losses of the cavity due to the nanoparticles are obtained. By comparing the losses L to the mode waist w_0 of the cavity (compare equation 2.91), they are converted to extinction cross sections

$$\sigma_{ext} = \frac{\pi w_0^2}{4} L. \tag{4.4}$$

The waist is obtained from evaluating the size of the point spread functions obtained for individual particles by fitting 2D Gaussians (for a section through such a point spread function compare figure 4.12).

Basically it is equivalent to derive the losses and the extinction cross section of particles within the cavity from the transmission or the linewidth of the resonator. Figure 4.6 shows a comparison between the extinction cross section of an individual particle (which is not a single gold sphere) obtained from the linewidth of the cavity and from its transmission. In later stages of the experiment, it turned out, that the extinction measurement from the linewidth is more robust, especially power fluctuations don't affect the signal any more. In the polarization sensitive experiments with nanorods (section 4.4) the transmission signal was influenced by some unknown effect leading to implausible results, while the measurements from the linewidth gave valid values. Thus, all later experiments were optimized for linewidth measurements achieving comparable or better data quality as the transmission data in this experiment.

To measure the individual extinction cross section of each nanoparticle, the particles are at first located using an image recognition algorithm coming with

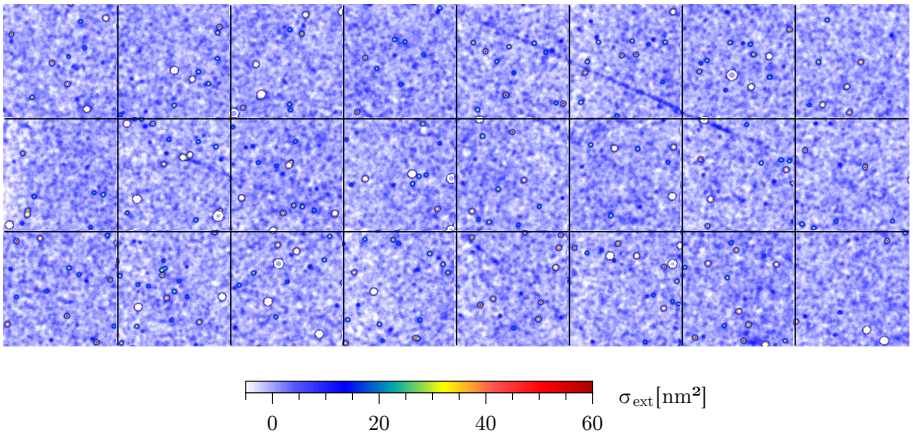

(a) Stitched extinction cross section image. The image is composed of 24 images with a size of 100 µm × 100 µm each and a pixel size of 0.5 µm × 0.5 µm.

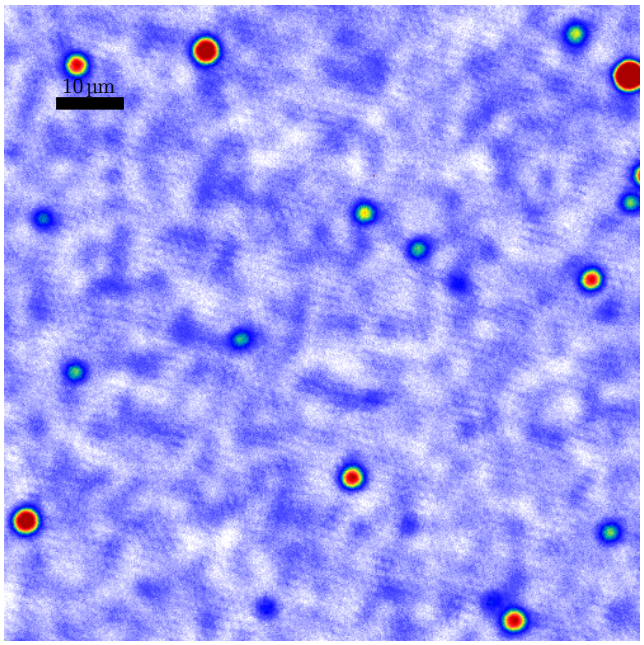

(b) Single scanning cavity image with a size of 100 µm × 100 µm at a pixel size of 0.2 µm × 0.2 µm.

Figure 4.5: Extinction cross section imaging of a surface carrying gold nanoparticles with a diameter of 41 nm. The colour scale is the same for both images.

Mathematica[4]. Therefore each image is binarized and the arising white blobs are identified with particles. Figure 4.7 shows the measured extinction data and a greyscale image where the detected particles are marked with red circles.

[4] A very powerful computer algebra system by Wolfram Research

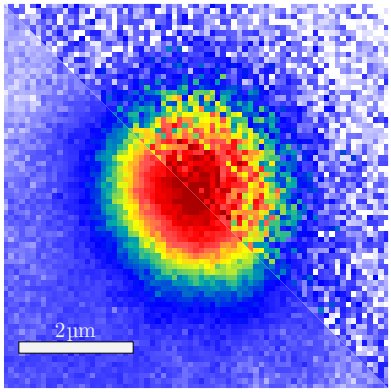

(a) Extinction image: upper right corner extinction measured from linewidth, lower left corner: extinction measured from transmission.

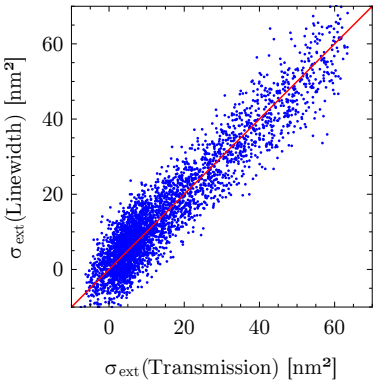

(b) Pixel-by-pixel comparison of the extinction measured by transmission or linewidth.

Figure 4.6: Equivalence of the extinction measurement by linewidth and transmission.

To each particle found, a 2D-Gaussian is fitted, and amplitude and size are

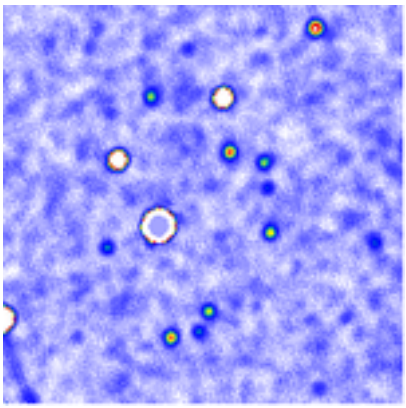

(a) Extinction image, Color scale as in fig. 4.5.

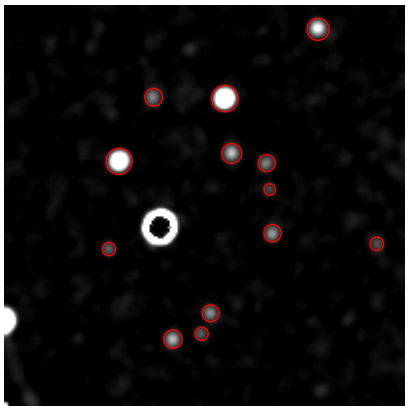

(b) Greyscale image with marked particles.

Figure 4.7: Detection of particles on a 100 µm × 100 µm large extinction image with a pixel size of 0.5 µm × 0.5 µm.

stored. From this data set, at first the mode waist is measured. As the observed particles are convolutions of a nanoparticle with the cavity mode, which is orders of magnitude larger than the particle, the observed point spread function size is a good measure for the cavity mode waist. Figure 4.8 shows the corresponding histogram and a Gaussian fit giving a waist of $2.4 \pm 0.1\,\mu\text{m}$.

To investigate, down to which extinction cross section particles could be detected, the variation of the extinction cross section of the empty background

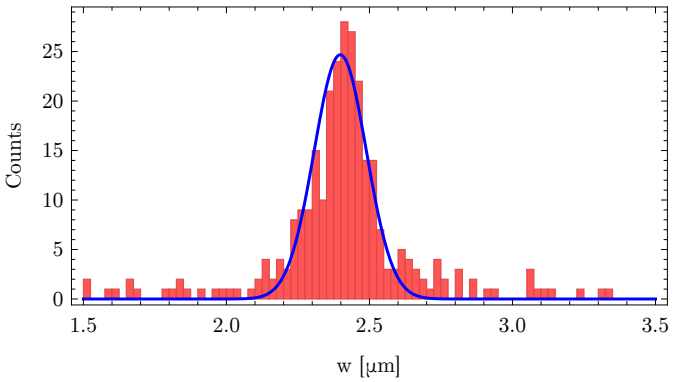

Figure 4.8: Histogram (red) and Gaussian fit (blue) of the observed particle size and thus the waist of the cavity mode.

of the measured surface is histogrammed as shown in figure 4.9. A Gaussian

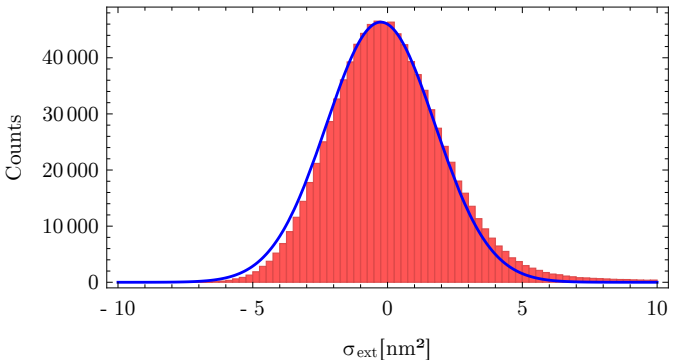

Figure 4.9: Histogram (red) and Gaussian fit (blue) of the background extinction cross section.

fit to this histogram shows, that the background signal is well centred around zero (centre: $0.25\,\mathrm{nm}^2$). The standard deviation of the Gaussian and thus the sensitivity of the microscope is $2.0\,\mathrm{nm}^2$.

The central result of this experiment is the measurement of the extinction cross section of gold nanospheres with a diametre of 41 nm. Figure 4.10 shows the distribution of the measured extinction cross sections. For this evaluation, only particles with a size close to the measured waist of the cavity mode have been selected in order to suppress disturbing effects due to extent agglomerates or dirt.

The measured data (red histogram) is compared to a calculated distribution of the extinction cross section in Rayleigh approximation (c.f. section 2.1.2) taking into account effects due to the surface, the particle is placed on (c.f. section 2.1.6), and due to the small particle size (c.f. section 2.1.5). The model is based on the material parameters for gold [45] and takes into account the given size and its variation by the manufacturer. Except from the amplitude of

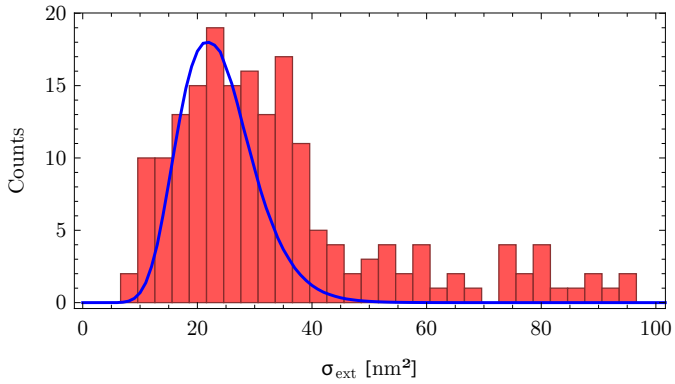

Figure 4.10: Histogram (red) and calculated distribution (blue) of the extinction cross section of gold nanospheres with a diameter of 41 nm.

the resulting distribution, the model has no free parameter.

The good agreement of the ab initio calculus to the measured data, except from a small number of particles with large extinction, which might correspond to particles with a size beyond the specifications, doublets of particles, point-like dirt or mirror contaminations, demonstrates the capability of quantitative measurements of the extinction cross section of individual nanoparticles at high sensitivity and resolution.

4.3 Enhanced Resolution Microscopy

Fibre-based micro resonators allow for easy coupling to higher order transversal cavity modes due to the non-optimal matching of the fibre mode to the fundamental cavity mode. These higher order modes can, as shown in section 2.3.3, be used to improve the spatial resolution of the scanning cavity microscope by adequate linear combination. As the higher modes cannot be avoided, the resolution enhancement basically comes only for the cost of evaluating the modes.

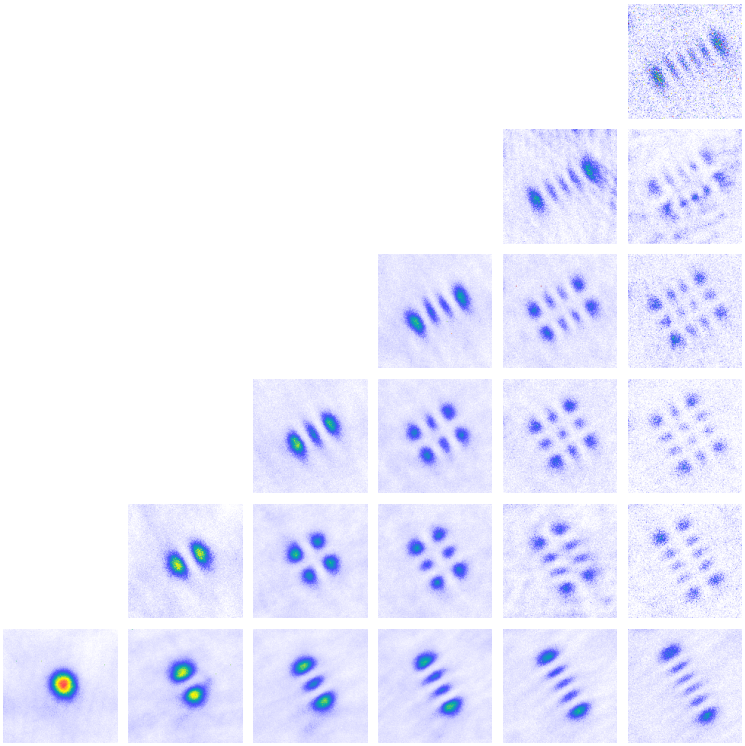

(a) Individual modes of the fundamental and the first five higher orders of transversal modes.

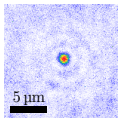

(b) Enhanced resolution image.

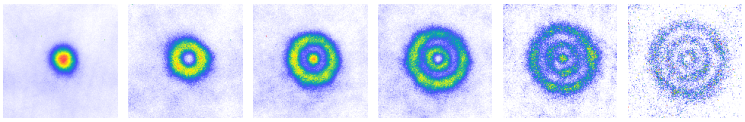

(c) Sums of the modes of each transversal order.

Figure 4.11: Extinction images of the individual modes used to generate an enhanced resolution image.

For demonstrating this method, transverse modes up to the 5^{th} higher order have been recorded. To get modes that are not disturbed by mode mixing, transverse modes from three neighbouring longitudinal orders have been consid-

ered. Figure 4.11(a) shows extinction maps of a single particle recorded using these modes. The individual extinction maps of each order are summed up as illustrated in figure 4.11(c) resembling rotationally symmetrical Laguerre-Gauss modes.

These Laguerre-Gaussian like modes are added up to a weighted sum with weighting factors

$$c_m = \frac{1}{\sqrt{\cosh \rho}} \sum_{m=0}^{\infty} (-1)^m \frac{\sqrt{m!}}{\sqrt{2^m}\frac{m}{2}!} \sqrt{\tanh^m(\rho)} \tag{4.5}$$

according to equation 2.103. The squeezing strength $\rho = 2$ was empirically chosen to optimize the resulting mode waist while leaving the background modulation small. Figure 4.11(b) shows the resulting resolution enhanced image.

The waist of the fundamental mode and the enhanced resolution mode have been determined by fitting a Gaussian to averaged (5 rows) sections through the respective extinction maps. For the map taken with the fundamental mode, a waist of 2.33 µm and for the enhance resolution map a waist of 0.87 µm has been found. This corresponds to an increased resolution by a factor of 2.7. Figure 4.12 shows these sections.

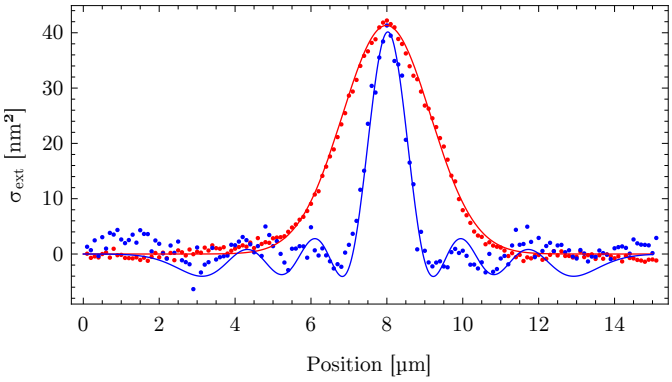

Figure 4.12: Average section (5 rows) through the extinction map of an individual particle taken with the fundamental mode (red dots) with a Gaussian fit (red solid line) and through the enhanced resolution map (blue dots) with a corresponding fit for six superimposing Hermite-Gaussian or Hermite-Laguerrian modes (blue solid line).

As discussed in section 2.3.3 and illustrated in figure 2.20, the highest gain in spatial resolution is obtained by combining the first and eventually second order higher transverse mode, which is more easy to realize in practice.

Figure 4.13 shows an example for resolution enhancement for a very dense sample with gold nanospheres of a diameter of 41 nm. While on the extinction image taken with the fundamental mode (figure 4.13(a)) individual particles are only barely visible, adding images taken with two additional resonator modes allows to easily locate individual particles (figure 4.13(b)). The enhancement of spatial resolution doesn't influence the extinction measurement much and still provides quantitative information on the extinction cross section.

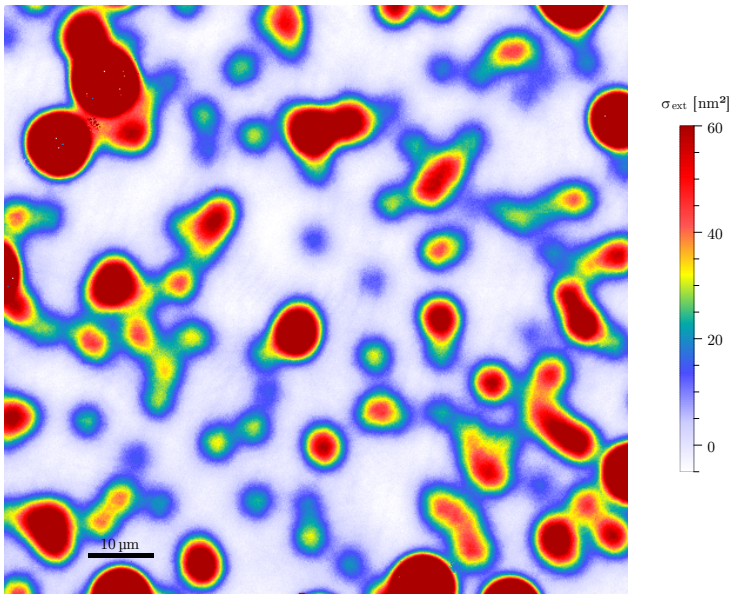

(a) Fundamental mode image.

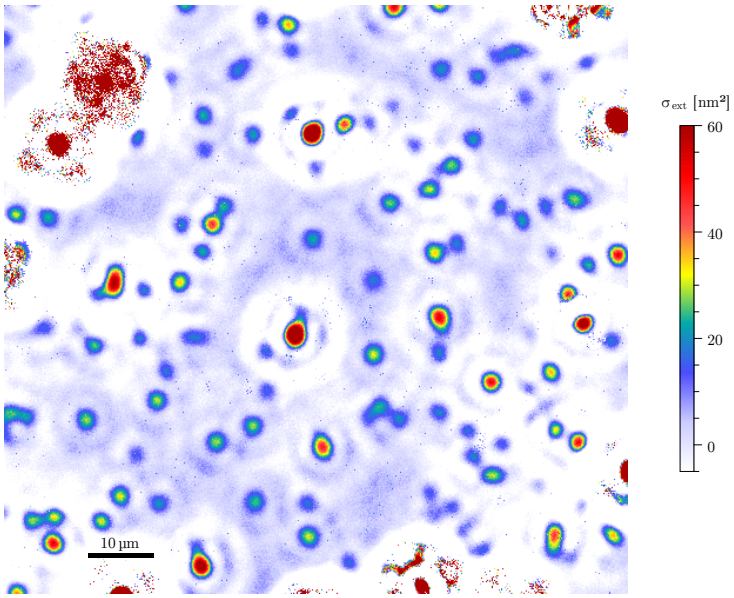

(b) Enhanced resolution image comprising the first and second higher order transverse modes.

Figure 4.13: Extinction imaging of a dense sample carrying gold nanospheres with a diameter of 41 nm. The image size is 100 µm × 100 µm, the pixel size 0.2 µm × 0.2 µm.

4.4 Extinction Contrast and Birefringence of Gold Nanorods

4.4.1 Introducing Anisotropy to the Cavity

Gold nanorods introduce anisotropy to the cavity which can be detected by exploiting the splitting of each cavity mode into two orthogonally polarized resonances. As the nanorods have a different polarizability along each half axis, they have different extinction cross sections for each axis. By analysing the linewidths of the two polarization channels individually, the difference of the two extinction cross sections of the particle, projected onto the cavity axes, $\sigma_{ext,H} - \sigma_{ext,V}$ can be detected.

The projection of the extinction cross section is derived from the projection of the polarizability tensor of the particle to the cavity axes H and V given by

$$\alpha_H = \sqrt{\left(\Re(\alpha_l)\cos\theta\right)^2 + \left(\Re(\alpha_s)\sin\theta\right)^2} + i\sqrt{\left(\Im(\alpha_l)\cos\theta\right)^2 + \left(\Im(\alpha_s)\sin\theta\right)^2} \tag{4.6}$$

$$\alpha_V = \sqrt{\left(\Re(\alpha_l)\sin\theta\right)^2 + \left(\Re(\alpha_s)\cos\theta\right)^2} + i\sqrt{\left(\Im(\alpha_l)\sin\theta\right)^2 + \left(\Im(\alpha_s)\cos\theta\right)^2} \tag{4.7}$$

where α_l denotes the polarizability of the long and α_s the polarizability of the short half axis of the particle and θ the angle between the particle's long axes and the H-polarization plane. Figure 4.14(a) shows the extinction cross sections of the two half axes and their difference depending on the orientation of the particle.

Furthermore the nanorod induces different frequency shifts to the two cavity axes. Thus, it can be seen as a birefringent object inside the resonator. By observing the frequency spacing between the two orthogonally polarized resonances of each mode, the birefringence projected to the cavity axes can be observed. Figure 4.14(b) shows the expected frequency shift for an individual rod used in the experiment.

Eventually a birefringent particle influences the orientation of the cavity polarization as introduced in section 2.2.3 leading to modified extinction measurements.

Due to a miscalculation during the planning and evaluation of the experiment, very small nanorods with a size of $34\,\mathrm{nm} \times 25\,\mathrm{nm} \times 25\,\mathrm{nm}$ corresponding to an extinction cross section of $19\,\mathrm{nm}^2 \times 5\,\mathrm{nm}^2$ were used. As the sample was initially analysed under the assumption of 8 times higher extinction cross sections, it was prepared such that particles of larger extinction cross section, possibly agglomerates of particles dominate individual ones. The results presented in the following are based on a reevaluation of this data.

4.4.2 Sample Preparation

For measurements on gold nanorods, particles with a size of $34\,\mathrm{nm} \times 25\,\mathrm{nm} \times 25\,\mathrm{nm}$ with a variation of $8\,\%$[5] in an aqueous dispersion were diluted with water and

[5] STREM Chemicals Gold nanorods (Axial Diameter - 25 nm, Wavelength 550 nm) 79-6000, LOT 21230100

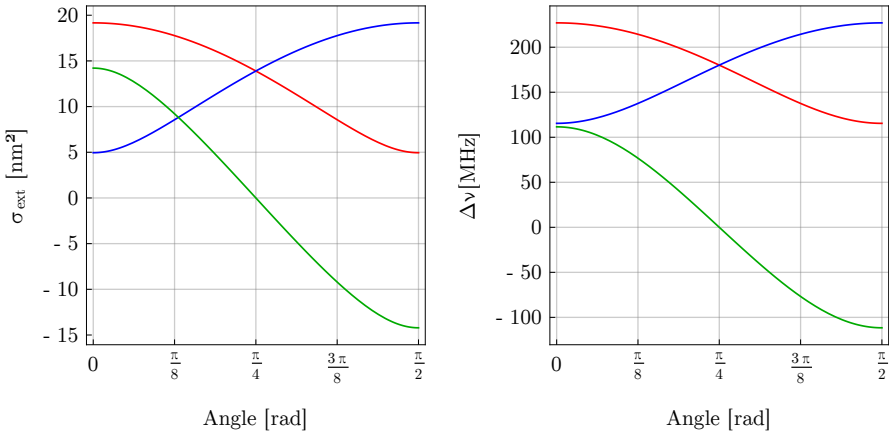

(a) Extinction cross section of nanorods

(b) Frequency shift due to nanorods

Figure 4.14: Extinction cross section and frequency shift of a cavity (wavelength 780 nm, waist 2.4 µm, length 32 antinodes) due to a gold nanorod (34 nm × 25 nm × 25 nm) depending on its orientation with respect to the H-polarisation plane of the probe light. Absolute values for polarization axes (red (H), blue (V)) and their differences (green) are calculated using numerical results for the depolarization factor [41] taking into account the shape of the particles. The values shown include effects of the surface, the particle is placed on and effects due to the small particle size.

spincoated to a plane mirror[6] as described for the nanospheres. Figure 4.15 shows an extinction map of the sample, the colour scale is chosen such that individual particles are clearly visible. Figure 4.16 shows a histogram of the extinction cross sections of particles on the sample with a point spread function size comparable to the mode size of 2.4 µm for both polarization axes of the cavity.

This histogram is compared to calculated extinction cross section distributions for individual nanorods, based on numerical depolarization factors [41] and various clusters of nanorods. Here the extinction cross sections are estimated by ellipsoids with half axes corresponding to the sum of the half axes of the individual particles setting up the cluster. All models assume a size variation of 8 % as stated by the particle manufacturer and average over all particle orientations. As the extinction cross section of nanorods and even more of clusters of particles strongly depends on the exact shape [22, 41], the arrangement and the gap between the individual particles [141–143] the shown distributions are only rough estimates. By combining the extinction distributions for compact clusters of 1 to 4 particles, the found extinction cross section distribution can at least partly resembled.

Nevertheless, the exact type of the particles, having an extinction cross section larger than that of individual ones, where the modelled extinction distri-

[6] substrate and coating by *Layertec*

bution fits very well, has to remain open.

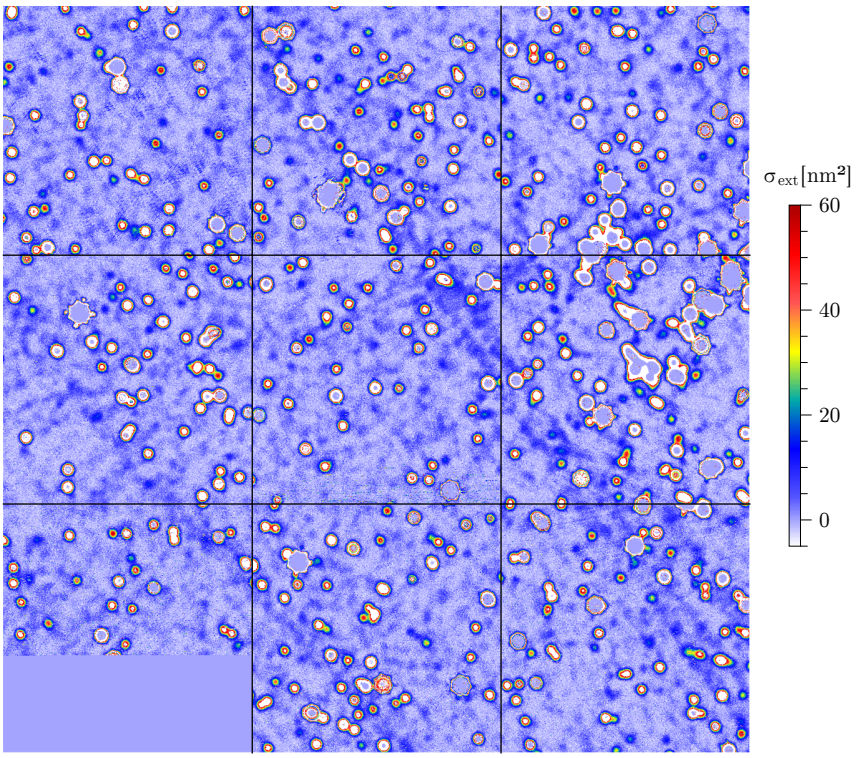

Figure 4.15: Stiched extinction cross section map of the gold nanorod sample. The map shows the average of both polarization channels. The image is composed of 9 images with a size of 100 µm × 100 µm each and a pixel size of 0.25 µm × 0.25 µm.

4.4.3 Extinction Contrast and Birefringence

Qualitative Observation

To illustrate the effects of anisotropic particles in a cavity with polarization split resonances, at first clusters of nanorods are investigated, as their effect on the resonator is much more pronounced than that of individual ones.

Figure 4.17(a) shows an extinction cross section map for the horizontally polarized resonance of the cavity while figure 4.17(b) shows the map for the vertically polarized resonance. To identify elongated particles showing more absorption along one axis than along the other, the extinction contrast, the difference of both channels $\Delta\sigma_{ext} = \sigma_{ext,H} - \sigma_{ext,V}$ is mapped in figure 4.17(c).

Besides different extinction along the two half axes of the particle, the ellipticity leads to different frequency shifts of the cavity and thus to a variation of the splitting of the two orthogonally polarized resonances of each cavity mode. Figure 4.17(d) shows the variation of the splitting of the two resonances. For

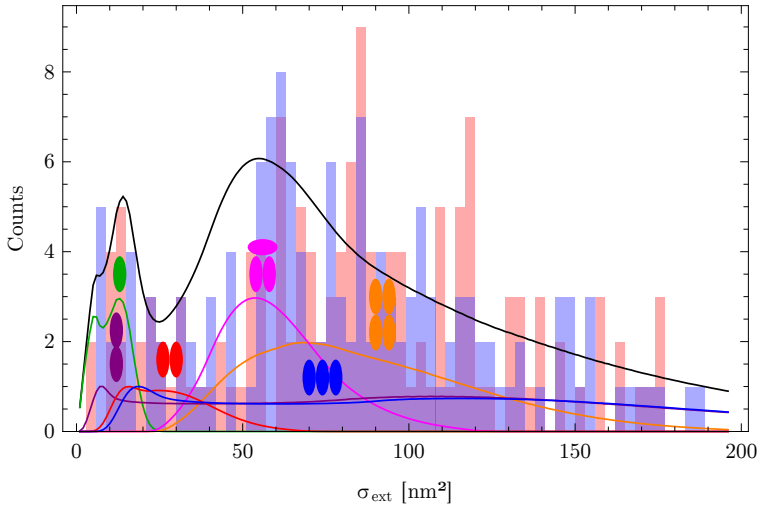

Figure 4.16: Histogram of the extinction cross sections of particles on the nanorod sample for horizontally (light red) and vertically (light blue) polarized light. Calculated extinction distributions for individual nanorods (green line), various clusters of particles are shown (colour lines) and an empirically weighted sum of them (black line). The arrangements of the corresponding clusters are illustrated in the plot, the aspect ratios are not to scale.

clarity, the map is shifted by the intrinsic splitting of 740 MHz to be centred around zero.

To illustrate the effect of an asymmetric nanocluster to the cavity, the transmission signal when scanning over such a cluster is recorded: figure 4.18 shows the sum of the two orthogonally polarized resonances of the fundamental mode when scanning over the particles denoted in figure 4.17(b). While for particle A, the spacing gets narrower and the H component of the light gets more absorbed than the V component, for particle B it's the other way round: the spacing gets wider and the absorption of the V component is stronger.

Quantitative Measurements

The results for the clusters investigated so far suggest a connection between extinction contrast and line splitting. While the extinction contrast $\Delta\sigma_{ext} = \sigma_{ext,H} - \sigma_{ext,V} \propto |\alpha_H|^2 - |\alpha_V|^2$ and the $\Delta\nu_H - \Delta\nu_V \propto \Re(\alpha_H) - \Re(\alpha_V)$ a strict correlation of both quantities can only be found for particles of equal size and shape, where $|\alpha|^2$ and $\Im(\alpha)$ are linked via the depolarization factors of the particle (c.f. section 2.1.3).

For a quantitative evaluation, the extinction contrast map (figure 4.19(a)) and the birefringence map (figure 4.19(b)) corresponding to the sample shown in figure 4.15 have been analysed.

Therefore individual particles have been detected in an average extinction map of both polarization channels as described for the nanospheres. For each particle found, a 2D-Gaussian has been fitted to the data from each polariza-

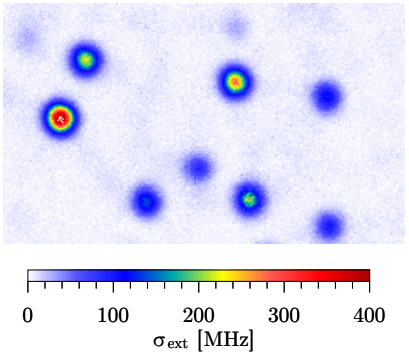

(a) Extinction cross section for H polarization.

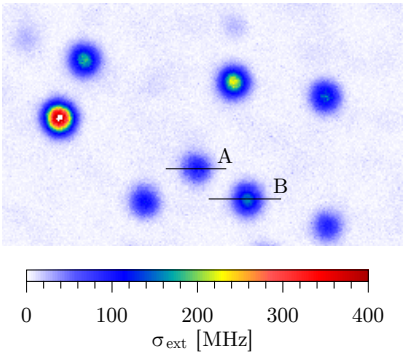

(b) Extinction cross section for V polarization.

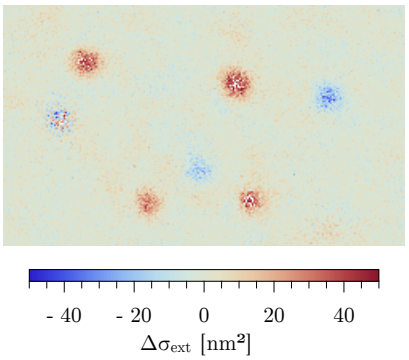

(c) Extinction contrast

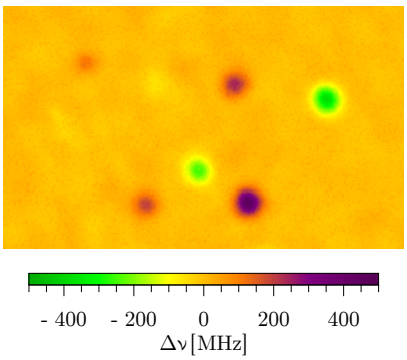

(d) Relative splitting of the two orthogonally polarized resonances.

Figure 4.17: Extinction contrast and birefringence imaging of a sample with clusters of nanorods. The image size is 50 µm × 30 µm, the pixel size is 0.2 µm × 0.2 µm.

tion channel and to the line spacing individually to retrieve mode waist and the extinction cross section for each channel and the extremal line spacing respectively.

Figure 4.20 shows the line splitting of particles with a point spread function size of (2 µm to 2.8 µm) compatible to the mode waist of 2.4 µm in dependence of the extinction contrast. Especially for very small line shifts or small extinction cross section, this measurement includes a large error, as data close to the background noise is hard to fit.

For an analysis of individual particles with a determined size and fixed shape, the particles were further selected by the extinction cross section. In figure 4.21, the line splitting in dependence of the extinction contrast of particles with an extinction cross section smaller than 30 nm^2 is shown. Most of these particles can be assumed to be individual nanorods.

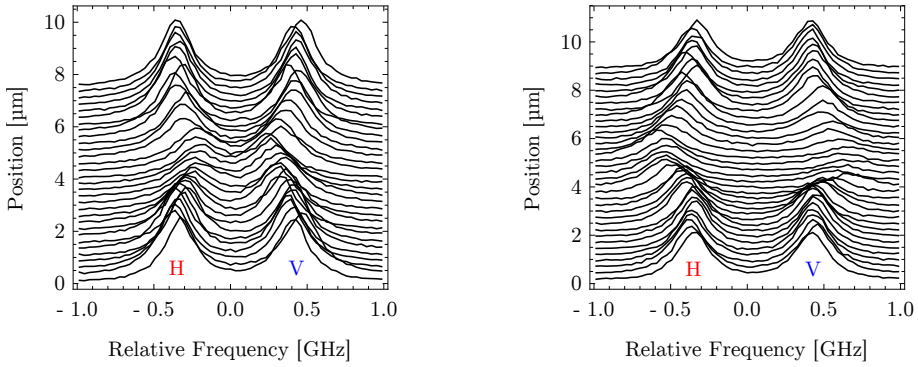

(a) Cavity transmission at particle A.

(b) Cavity transmission at particle B.

Figure 4.18: Sum of transmission signals for both polarizations when scanning over particle clusters denoted in figure 4.17(b).

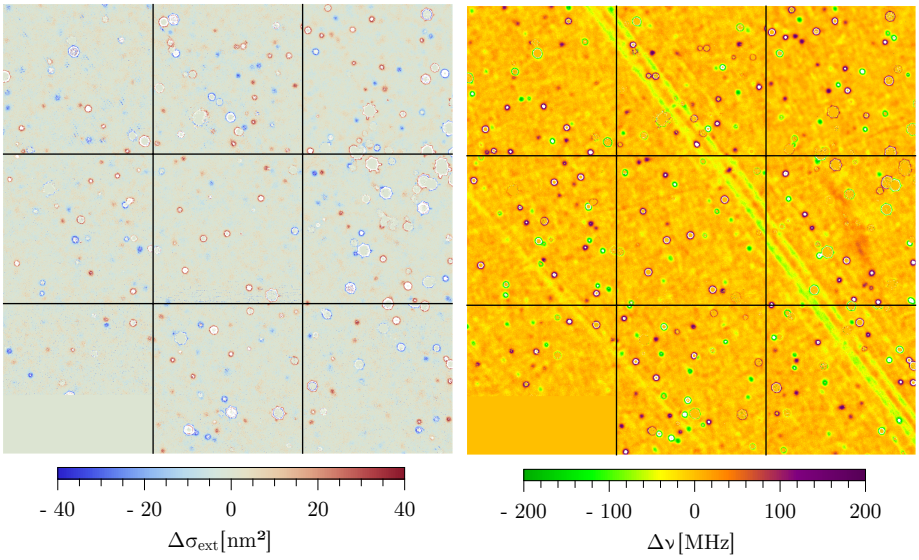

(a) Extinction contrast.

(b) Line spacing, centered around zero.

Figure 4.19: Stiched map of the extinction contrast and line spacing of the gold nanorod sample. The image is composed of 9 images with a size of 100 µm × 100 µm each and a pixel size of 0.25 µm × 0.25 µm.

4.4.4 Effects on the Cavity Polarization

A birefringent object inside an asymmetric cavity, as the resonator used here, is expected to modify the polarization of the cavity modes as introduced in section 2.2.3. To check, whether this is the case and the polarization of the cavity is turned by the particle or not as eventually the polarization state could be

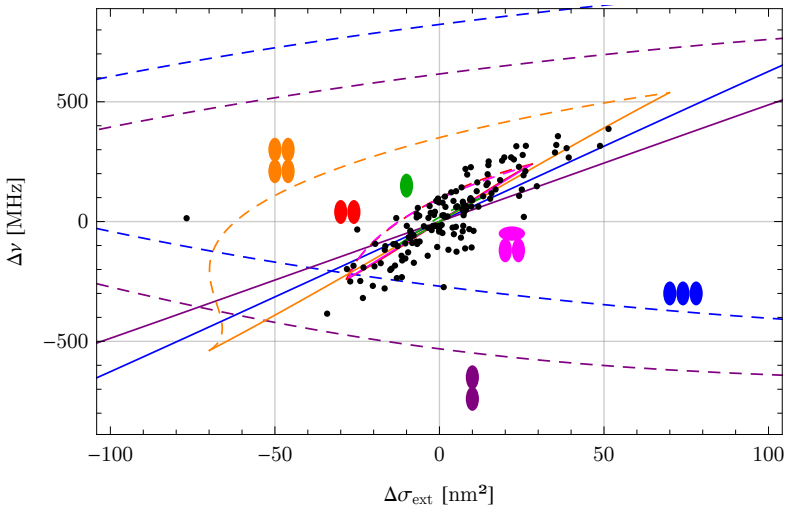

Figure 4.20: Line splitting $\Delta\nu$ in dependence of the extinction contrast $\Delta\sigma_{ext}$ of individual nanoparticles and clusters in comparison with ab initio models for this correlation for individual rods and various clusters. Models assuming a fixed polarisation are plotted with solid lines, models assuming a rotation of the polarisation of the resonator by the nanoparticle are plotted with dashed lines. The respective cluster configurations are depicted in plot, the shape of the particles is not to scale.

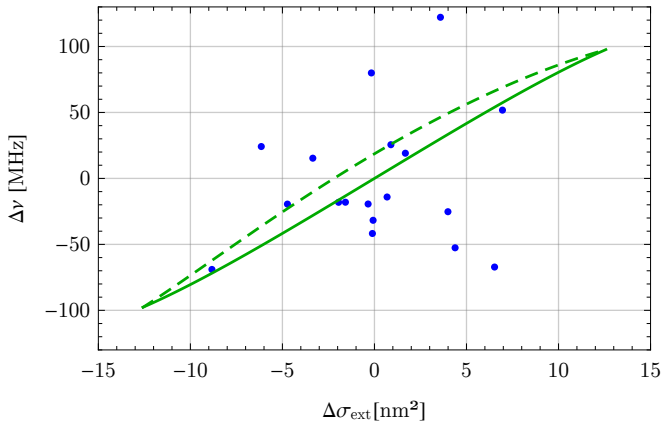

Figure 4.21: Line splitting $\Delta\nu$ in dependence of the extinction contrast $\Delta\sigma_{ext}$ for particles with an extinction contrast smaller than $30\,\mathrm{nm}^2$ in comparison to an ab initio model for nanorods assuming a fixed polarization within the cavity (green solid line) or a polarization modified by the particle (green dashed line).

strongly confined by the cavity mirror geometry, at first the measured correlation of extinction contrast and line splitting for individual particles is compared to

models of nanorods or clusters of nanorods inside a resonator assuming a fixed or a modified polarization.

Both models are based on the polarizability tensor of the particle or cluster approximated as an ellipsoid, calculated from the particle or cluster size, given by the manufacturer, material data for gold [45]. The model takes effects due to the surface, the particle is placed on and the small particle size into account as described in section 2.1.6 and 2.1.5. To face the more rod like than ellipsoidal shape of the individual rod, here numerical results for the depolarizability [41] are used.

For the models assuming a fixed polarization within the cavity (solid lines with zero-crossing in figure 4.20 and 4.21) the extinction contrast and the line splitting for different angles of the nanorod with respect to the fixed polarization planes within the resonator have been calculated and were correlated. For the model assuming a rotation of the polarization planes due to the nanorod (dashed curves in figure 4.20 and 4.21) the extinction contrast has been calculated with respect to the particle angle and the equivalent polarization angle θ_{eq} as described in equation 2.96 while for the line splitting the effective frequency shift δ_{eq} from equation 2.95 has been considered [71, 72].

Due to the poor data quality because of the choice of to small particles and the high number of potential agglomerates of particles, the data presented in figure 4.20 and 4.21 does not allow to confirm whether the polarization of the cavity stays in place or is influenced by the nanoparticles.

For a further investigation of the influence of nanorods on the polarization state of the resonator, the transmission signal of the cavity at each pixel is used. The polarization optics for separating the two orthogonally polarized resonances of each mode is aligned to the empty cavity such, that each detector sees only one resonance. If the polarization rotates, e.g. due to a nanorod, each detector will see two resonances: one at the initial position and the other at the position of the second polarization resonance, as the splitting optic doesn't fit properly any more.

To check for this effect, the transmission has been analysed at first as described in section 3.5.2. In a second step, a sum of two Lorentzians has been fitted to each channel in order to detect an arising second resonance peak due to a turning polarization. To do so, the positions and widths of the peaks found at the initial step have been fixed and only the amplitudes a_1 and a_2 of the two peaks were taken as free fit parameters.

Figure 4.22 shows normalized difference of the fitted amplitudes $\frac{a_1-a_2}{a_1+a_2}$ in dependence of the line splitting for both polarization channels. The amplitudes have been measured at the centre of the Gaussian fitted to the line splitting.

The data has been selected for line splitting point spread functions corresponding to the mode size of the cavity in a range of 2 µm to 2.8 µm. As the effect on the polarization state of an individual nanorod is very small, also larger objects were included. Because the amplitudes of the second arising peaks are very small, the measurement from the amplitude map is very susceptible for errors and measurement noise that get enhanced by the normalization process. Therefore the data is noisy and does not allow for a clear conclusion whether the polarization stays constant which would imply that the differences stay at a value close to one for all line splittings or is turned. This would lead to modulated values of the normalized difference at small line splittings. These modulations have again been modelled for individual nanorods and clusters of

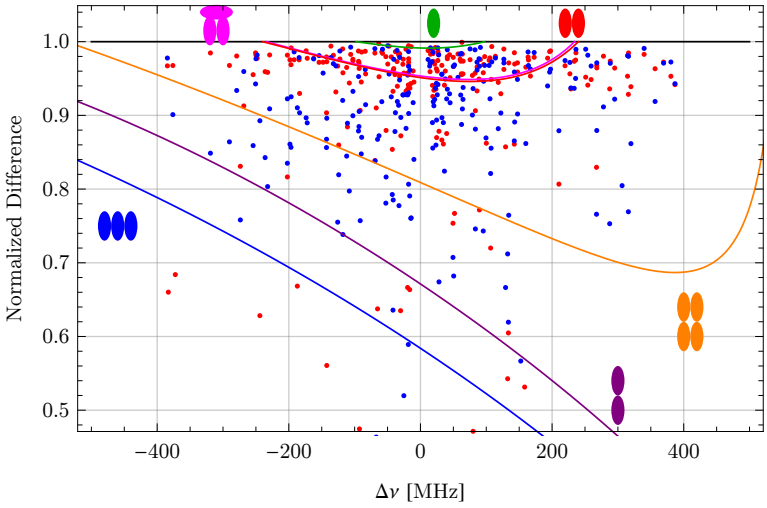

Figure 4.22: Normalized differences of the amplitudes of a sum of two Lorentzians fitted to each transmission channel (red, blue). The maximum of 1 for an uninfluenced peak is indicated by a black line. Models for a signal for a modified polarization for various clusters of particles are shown in coloured lines.

them. They are depicted in coloured lines in the figure.

As the data shown here is noisy and stems at least partly from particles of unknown size and shape, it is mandatory to repeat this measurement with larger particles of defined size and shape showing a more pronounced signal in order to prove whether the cavity behaves as expected meaning that the polarization turns with increasing birefringence of inserted particles, or if the high ellipticity of the mirror fabricated to the fibre leads to an unexpected high confinement of the polarization state. If the latter would be the case, especially the transition from the confined to the classical regime, where the polarization state turns, would be interesting to investigate.

4.5 Polarizability Measurements with 50 nm Gold Spheres

The last measurement sequence with the scanning cavity microscope shown in this work aims to determine the full complex polarizability of gold nanospheres. Due to the larger signal, here spheres with a diameter of 50 nm have been used. To measure the complex polarizability, two measurements are necessary to determine the real and the imaginary part of the quantity: an extinction measurement to get $\sigma_{ext} \propto |\alpha|^2 + \Im(\alpha)$ and a dispersion measurement for obtaining $\Delta\nu \propto \Re(\alpha)$.

Both measurements have been performed simultaneously: the extinction cross section is deduced from the linewidth of the fundamental mode of the cavity while the dispersion due to the particle is determined from the shift of the TEM02 and TEM20 mode with respect to the TEM11 mode as described in the introduction to the chapter on the setup (see chapter 3.1).

To compensate the background of the mirror in the dispersion measurement having nearly the same amplitude than the signal due to the particle, differential measurements have been performed. Therefore measurements before and after applying the nanoparticles have been subtracted to reduce the background and to access the dispersion information of the particles.

4.5.1 Sample Preparation and Characterization

As described for the previous experiments, the sample has been prepared by spincoating a diluted aqueous dispersion of gold nanospheres onto a plane mirror substrate. Here, nanospheres with a mean diameter of 48.5 nm with a variation below 8 % at an concentration of 4.5×10^{10} particles/ml[7] have been spincoated to an annealed plane mirror[8] to make a sparse sample. Figure 4.23 shows an extinction map of the sample.

To align the measurements before and after application of nanoparticles for subtracting the background, markers are fabricated to the plane mirror by the CO_2-laser. The marker structures have to be small and faint in order not to loose to much space on the mirror surface and in order to prevent the cavity length stabilization from falling out of lock when scanning over the markings.

For good pre-alignment, the mirror is mounted in a quadratic holder with tight fit to the scanning table allowing on the one hand to take the mirror out of the microscope and back with high position repeatability and on the other hand for spincoating nanoparticles without removing the mirror from the mount. This mount is depicted in figure 3.15, part ⓓ.

4.5.2 Setting up the Cavity

In contrast to the measurements shown so far, where only the fundamental mode of the cavity had been used, now the fundamental and at the same time the second order higher modes of the cavity are used as a scanning probe for microscopy.

[7] BBI Solutions Gold colloid - 50 nm EMGC50, Batch 14610
[8] Mirror substrate by *Layertec*, coating by *LASEROPTIK*

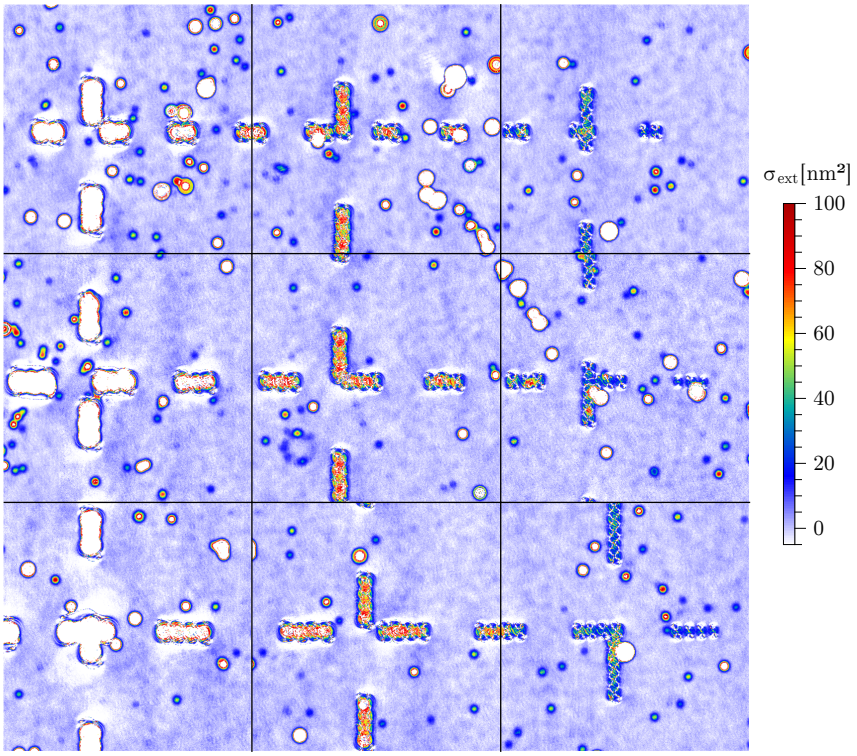

Figure 4.23: Extinction map of the sample carrying gold nanospheres of a diameter of 50 nm used for polarizability measurements. The image is composed of 9 microscope images with a size of 100 µm × 100 µm with a pixel size of 0.2 µm × 0.2 µm.

To do so, the modes of the selected order should not be influenced by mode mixing. Furthermore, the splitting of the TEM02 and TEM11 modes as well as the splitting of TEM20 and TEM11 modes should be equal to bridge the splitting with high-frequency sidebands and to evaluate the spacing as described in section 3.5.2.

For the cavities used in the experiment, the spacing between the TEM02 and TEM11 mode and between the TEM20 and TEM11 mode turned out to be asymmetric. The TEM11 mode is shifted between the TEM02 and TEM20 mode depending on the cavity length as shown in figure 4.24 for both polarizations.

This splitting reduces the freedom of choice for the resonator length to one or two nodes around the cavity length, at which the spacing is close to symmetric.

As the asymmetry of the splitting of the second order higher modes doesn't strongly depend on the angular alignment of the resonator, eventual mode mixing can be faced by this degree of freedom. Together with a lot of patience of the experimenter and a bit of luck it is possible to find a setting of the cavity where all required modes can be addressed with at least little disturbance.

A further challenge is the separation of the two polarization planes of the cavity. For most fibres tested including fibre 16k used in the experiments de-

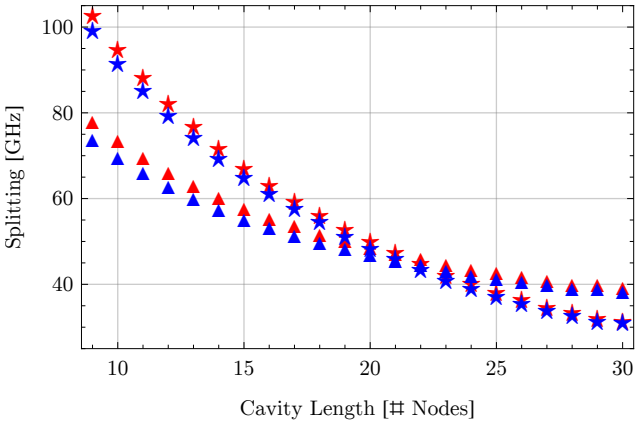

Figure 4.24: Frequency spacing between the TEM02 and TEM11 mode (▲) and between the TEM20 and TEM11 mode (★) for H (red) and V (blue) polarization in dependence of the cavity length of fibre 16k. The values are measured without high-frequency sidebands.

scribed in the following it's only possible to separate one plane while the other plane remains a mixture of polarisations. Especially for the TEM11 mode the separation of polarizations is challenging.

4.5.3 Background Subtraction

For effective background subtraction, the measurements before and after applying nanoparticles have to be aligned as good as possible. Although, the mirror mounting allows for a very precise positioning, the two measurements, figure 4.25 shows exemplary extinction maps for the two measurements, have to be fine-aligned. Therefore, the images are binarized and pre-aligned using *Mathematica's* `FindGeometricTransform` algorithm, that gives a transform that overlaps both images. Here, only shifts along the coordinate axes were used, but no rotations.

To optimize the alignment further, the positioning of the two images with respect to each other is varied for some pixels around the found shift. For each setting, a histogram of the difference of both images is evaluated. The width of the distribution of the background is used as an indicator for the overlap of the two images. The setting leading to the narrowest distribution is used for further evaluation.

The results of the background subtraction for extinction and dispersion measurements are discussed in the following sections.

4.5.4 Extinction of Gold Nanospheres

To analyse the extinction due to the mirror and the particles on its surface, the measured linewith of the cavity is in a first step converted to additional losses of the cavity. Based on the exact knowledge of the cavity length l, the definition

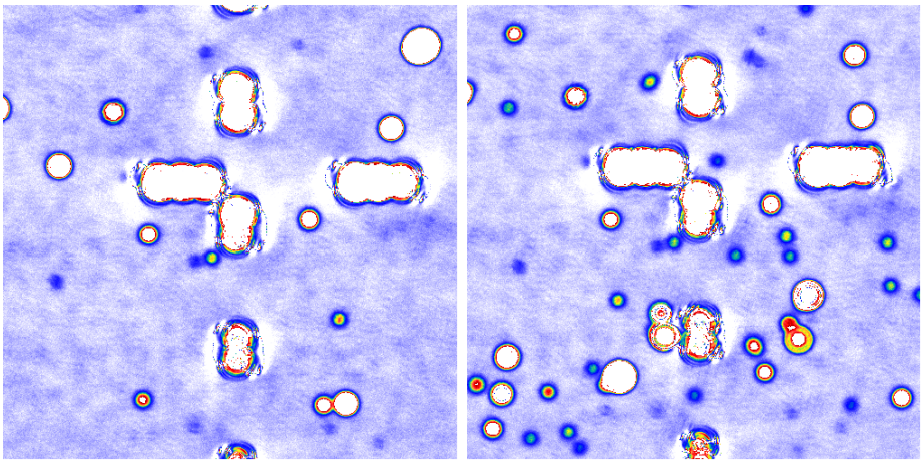

(a) Before applying particles. (b) After applying particles.

Figure 4.25: Extinction map of the sample before and after applying nanoparticles. The image size is 100 µm × 100 µm, the pixel size is 0.2 µm × 0.2 µm, the colour scale is the same as in figure 4.23.

of the finesse

$$\mathcal{F} = \frac{\nu_F}{\Delta\nu} = \frac{2\pi}{2L + L_1 + L_2 + T_1 + T_2}. \tag{4.8}$$

(c.f. equation 2.2.1) is used to calculate the losses. Instead of finding the exact cavity parameters from fitting a measurement of the linewidth in dependence of the cavity length, here the cavity finesse and thus the additional loss due to particles is calculated from the measured linewidth $\Delta\nu$, the most probable value for the linewidth $\Delta\nu_0$ and the cavity length without knowledge of the precise mirror parameters. The losses are determined by

$$L = \frac{1}{2}\left(\frac{1}{\mathcal{F}} - \frac{1}{\mathcal{F}_0}\right) = \frac{1}{2\nu_F}\left(\Delta\nu - \Delta\nu_0\right) \tag{4.9}$$

with the free spectral range

$$\nu_F = \frac{c}{2l} \tag{4.10}$$

where c is the speed of light.

Due to lower mirror losses on the plane mirror and the fibre mirror, the cavity used in this experiment has a finesse of 86 800.

Before investigating the extinction cross sections of the particles, the effect of the background subtraction on the extinction measurement is studied. Figure 4.26 shows extinction maps of the same area without and with subtracted background, determined by a previous measurement without samples.

Although the background noise gets more homogeneous, the amplitude of the background is not significantly improved. While the standard deviation of the background of the extinction map for the uncorrected image is 1.75 nm^2 it is 1.7 nm^2 for the corrected map. Figure 4.27 illustrates, that the extinction measurements are only limited by instrument noise but not by extinction fluctuations e.g. due to mode mixing of the mirror substrate.

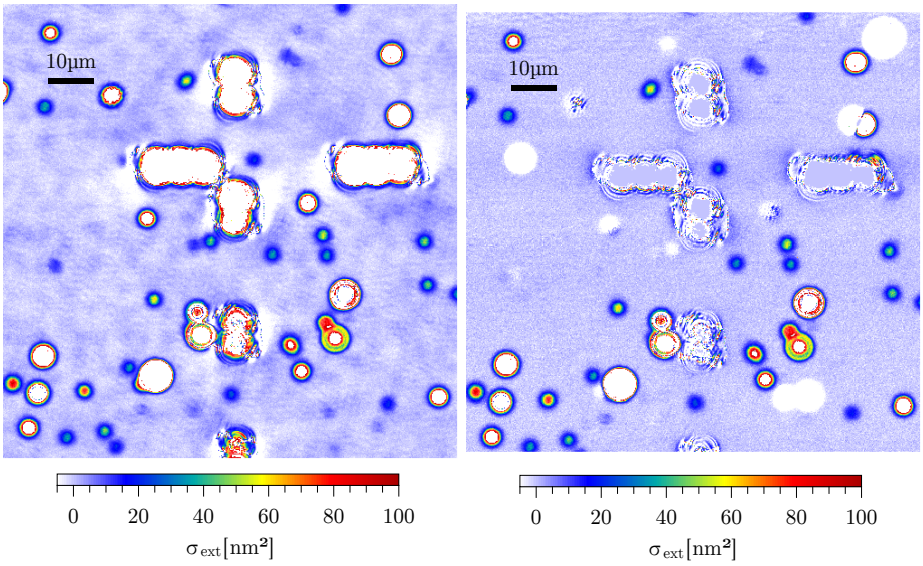

(a) With background. (b) Background subtracted.

Figure 4.26: Extinction map of gold nanosphere without and with subtracted background. The imagesize is 100 µm × 100 µm, the pixel size 0.2 µm × 0.2 µm.

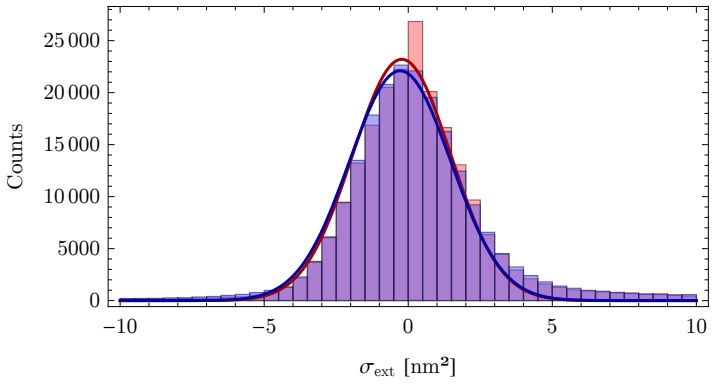

Figure 4.27: Histogram of the background of an extinction map with (red) and without subtracted background (blue). The overlapping area of both histograms is shaded purple. The solid lines show Gaussian fits to the histograms.

The analysis of the extinction of gold nanospheres has been done as described for the 40 nm spheres: after background correction, the images have been binarized, the particles have been detected using a particle detection algorithm and finally, a 2D-Gaussian has been fitted to each particle in order to retrieve the particle size and thus the size of the cavity mode and the losses due to the particle.

From the found particle size, the extinction cross section is calculated from

the fitted losses for each particle. The distribution of sizes, centred around $2.0 \pm 0.15\,\mu m$ is shown in figure 4.28.

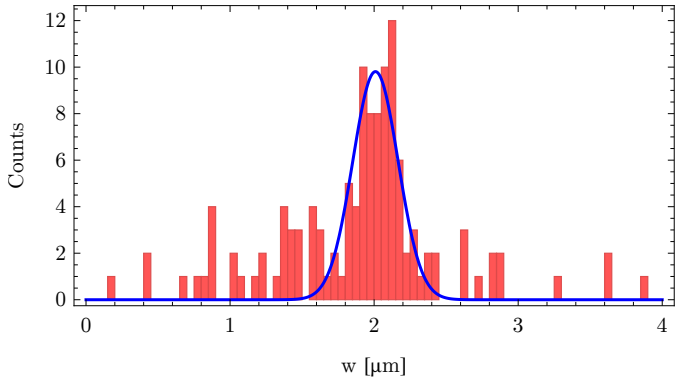

Figure 4.28: Histogram (red) of the mode waist w obtained from fitting a 2D-Gaussian to each absorbing particle. A Gaussian fit to the distribution is shown in blue.

The resulting distribution for the extinction cross sections is shown in figure 4.29. For the analysis, only particles with a size of $2.0 \pm 0.3\,\mu m$ are considered. The measured distribution is compared to an ab-initio calculated distribution, taking into account the given particle size distribution, the surface, the particle is lying on and effects due to the small particle size. The measurement of the extinction cross section and the calculation free of any adjustable parameter agree very well.

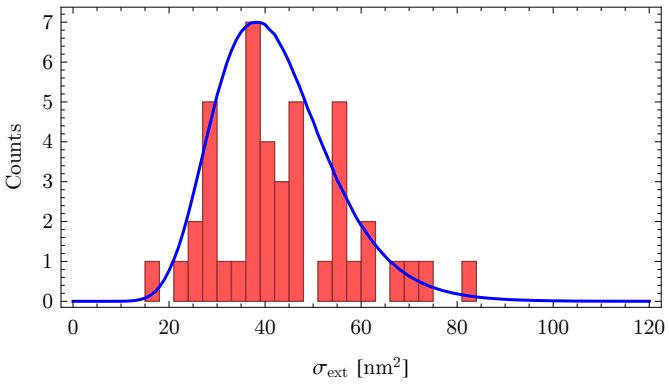

Figure 4.29: Histogram of the extinction cross sections of the gold nanospheres (red) and calculated distribution (blue) taking into account the particle size distribution, the surface the particle is placed on and effects due to the small particle size.

4.5.5 Dispersion due to Gold Nanospheres

To measure the dispersion due to a nanoparticle inside the cavity, the frequency shifts between the TEM02 and TEM11 and the TEM20 and TEM11 mode are exploited as described in the introduction to the previous chapter 3.1: while the resonance frequency of the TEM11 mode is unaffected if a particle is placed to its centre, the resonance frequency of the TEM02 and TEM20 modes get shifted, as they have a non-vanishing electrical field in their centre in contrast to the TEM11 mode which has no field there. This method suppresses noise due to mechanical fluctuations and allows to measure frequency shifts at the sub-linewidth level.

The frequency difference between the TEM02 and TEM11 mode is given by equation 2.94:

$$\Delta\nu_{11-02} = \frac{\Re(\alpha)\,\nu_{Laser}}{2\epsilon_0 V_m}\left[\left(\frac{u_{11}(x,y,z)}{u_0}\right)^2 - \left(\frac{u_{02}(x,y,z)}{u_0}\right)^2\right]. \tag{4.11}$$

To combine both spacings between the TEM11 and TEM02 or TEM20 mode respectively and for efficient evaluation and data representations, the both differences are summed up and $\Delta\nu = (\nu_{11} - \nu_{02}) + (\nu_{11} - \nu_{20})$ is analysed. The combination of three higher order modes leads to a bloom-shaped point spread function shown in figure 4.30.

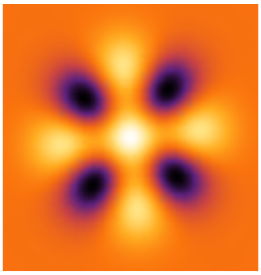

Figure 4.30: Point spread function of the dispersion measurement.

A measured frequency spacing map of a mirror carrying gold nanospheres is shown in figure 4.31(a). The map shows the same area as the extinction maps shown in figure 4.26. Within the strong background, the individual particles are barely visible. To reduce the background, resulting from modulations of the mirror surface [144] and slight refractive index modulations of the dielectric coating both at length scales of the cavity mode, a measurement of the same area without particles is subtracted as described above. Figure 4.31(b) shows the same area as before with subtracted background. Now, individual particles get visible, indicated by their bloom-shaped point spread function.

As the dispersion measurement is susceptible to disturbances, it fails at quite a few pixels, visible by the grainy structure in the frequency spacing maps. To get a clearer view on the data and the apparatus' capability to resolve small index fluctuations, the faulty pixels have been removed at a section of the frequency spacing map shown in figure 4.31 and have been replaced by the average values of the surrounding pixels. Figure 4.32 shows the respective map in comparison with a map still containing the faulty pixels.

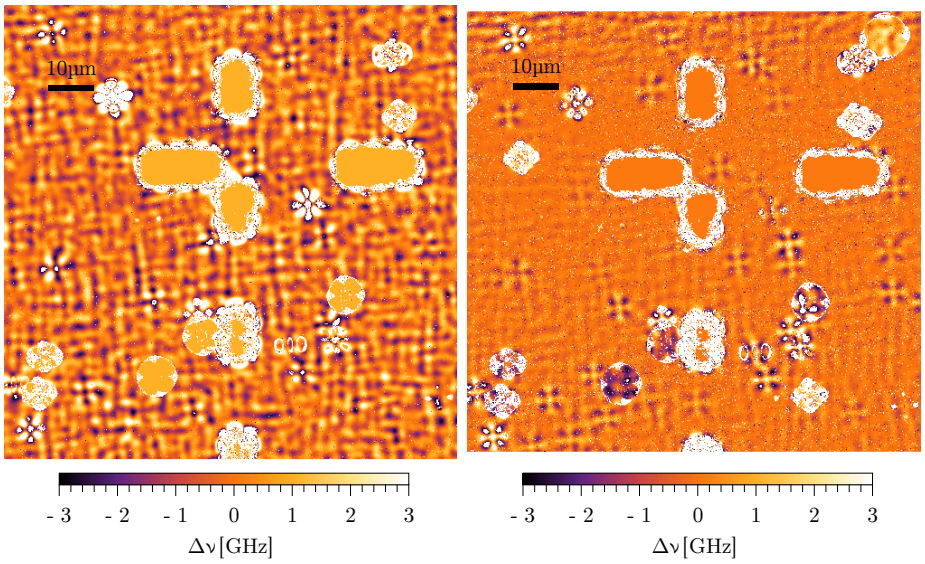

(a) With background. (b) Without background.

Figure 4.31: Frequency spacing map of a mirror surface carrying 50 nm gold nanospheres. The image size is 100 µm × 100 µm,the pixel size is 0.2 µm × 0.2 µm.

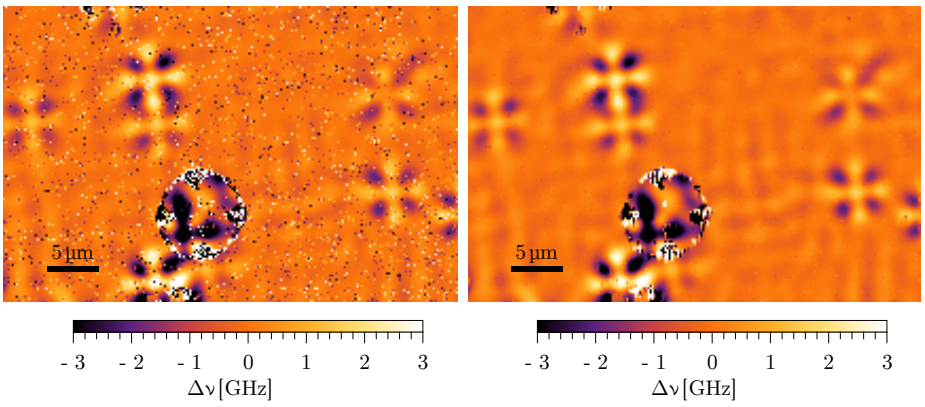

(a) With faulty pixels. (b) Without faulty pixels.

Figure 4.32: Detail view of a frequency spacing map of a mirror surface carrying 50 nm gold nanospheres with and without faulty pixels. The faulty pixels have been replaced by the average value of the neighbouring ones. The image size is 44 µm × 22 µm, the pixel size is 0.2 µm × 0.2 µm

For a quantitative analysis of the effect of background subtraction at the frequency spacing measurement, the background before and after subtraction are plotted as a histogram (figure 4.33). By fitting Gaussians to the histograms, the distribution is analysed: by background subtraction the wide-spread background

(standard deviation 780 MHz) is reduced by a factor of 4.5. The standard deviation of the subtracted background is 196 MHz allowing to observe individual 50 nm gold spheres (frequency shift peak-peak 3.5 GHz).

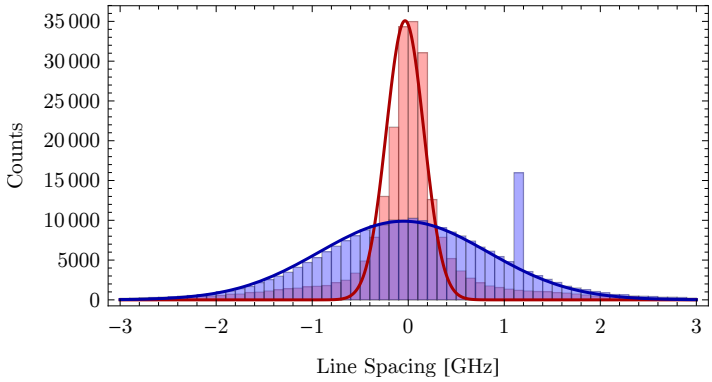

Figure 4.33: Histogram of the frequency spacing background before (blue) and after (red) subtraction. Gaussian fits to the data are shown as solid lines. The data corresponds to the frequency spacing maps shown in figure 4.31.

To investigate the frequency spacing for many particles, the same field as for the extinction measurement has been analysed. The corresponding frequency spacing map is shown in figure 4.34.

To each particle, the function for the frequency spacing given above is fitted. As the function is not spherical symmetric, its angular orientation has to be a fit parameter as well as the waist and the real part of the polarizability that can be measured directly here.

The resulting values for the real part of the polarizability are shown in figure 4.35 and, as above, compared to a calculated distribution. Again the measured data resembles the calculated distribution very well.

Knowing the real part of the polarizability, it is possible to calculate the corresponding imaginary part from the extinction measurement as

$$\sigma_{ext} = \sigma_{abs} + \sigma_{sca} = \frac{2\pi}{\lambda\,\epsilon_0}\Im\left(\alpha\right) + \left(\frac{2\pi}{\lambda}\right)^4 \frac{1}{6\pi\,\epsilon_0^2}\left|\alpha\right|^2. \tag{4.12}$$

Solving for $\Im\left(\alpha\right)$ leads to

$$\Im\left(\alpha\right) = \sqrt{\frac{3\lambda^4\,\epsilon_0^2}{8\pi^3}\,\sigma_{ext} - \frac{3\lambda^3\,\epsilon_0}{4\pi^2}\,\Re\left(\alpha\right) - \Re\left(\alpha\right)^2}. \tag{4.13}$$

The resulting distribution of $\Im\left(\alpha\right)$ calculated for each particle from the measured values for σ_{ext} and $\Re\left(\alpha\right)$ is shown in figure 4.36. Again the data resembles the calculated distribution for $\Im\left(\alpha\right)$ very well.

This result underlines the ability of the scanning cavity microscope not only to quantify the extinction cross section of individual nanoparticles but also the dispersion and thus the full complex polarizability. By measuring this quantity, the optical properties of particles at Rayleigh limit can be fully determined. It

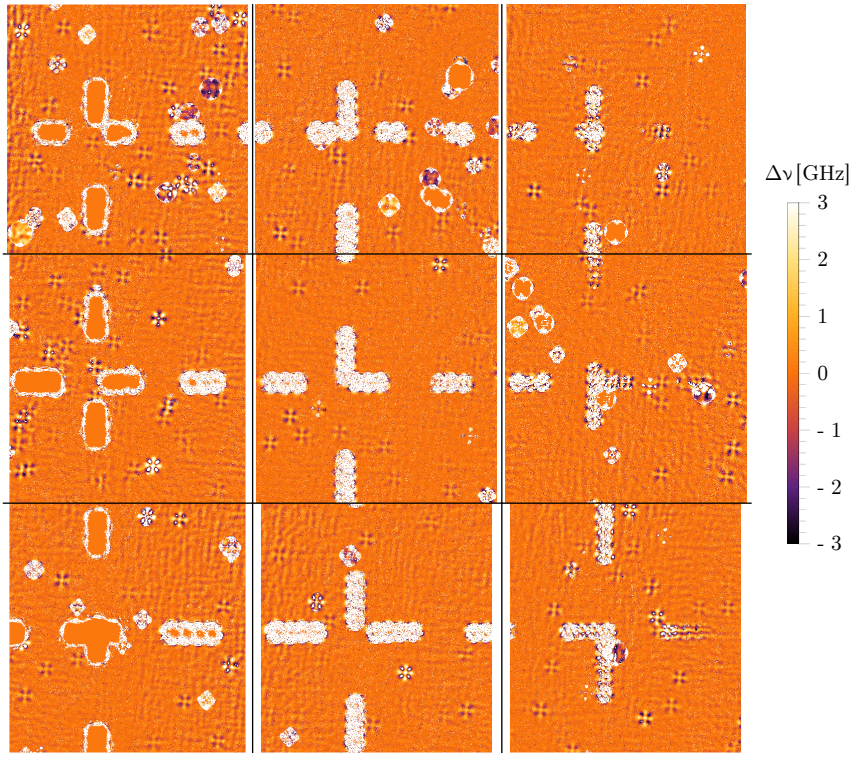

Figure 4.34: Frequency spacing map of the sample carrying gold nanospheres of a diameter of 50 nm used for polarizability measurements. The white space comes from the background subtraction where the two measurements don't overlap. The image is composed of 9 microscope images with a size of 100 µm × 100 µm with a pixel size of 0.2 µm × 0.2 µm.

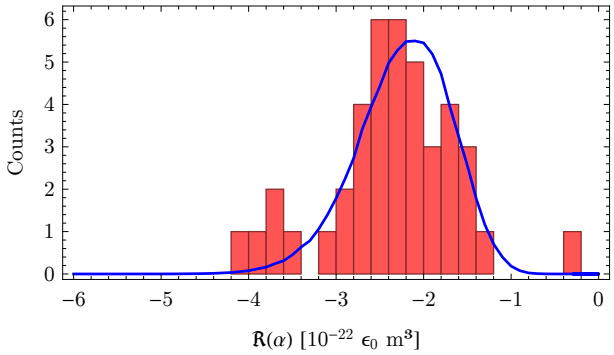

Figure 4.35: Histogram of $\Re(\alpha)$ for 50 nm gold spheres (red) and calculated distribution (blue) taking into account the size distribution of the particles, the surface it it placed to and effects due to its small size.

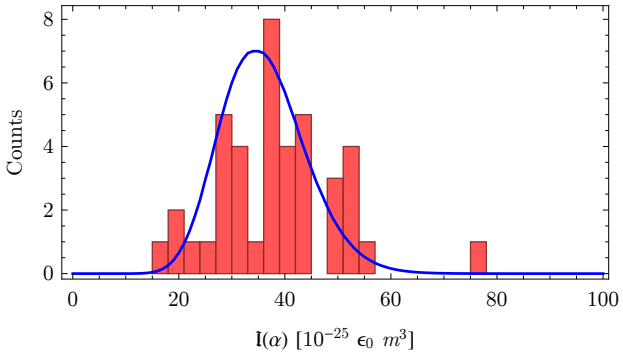

Figure 4.36: Histogram of $\Im(\alpha)$, calculated from the measured extinction cross section σ_{ext} and the measured $\Re(\alpha)$ for 50 nm gold spheres (red) and calculated distribution (blue) taking into account the size distribution of the particles, the surface it it placed to and effects due to its small size.

is noteworthy, that the presented precise dispersion measurements have been achieved without a frequency-locked cavity. This allows the implementation of this technique to applications that don't allow for robust cavity locking like the presented scanning cavity microscope.

Chapter 5

Towards an Underwater Cavity

5.1 Sensing Biological Systems in an Aqueous Environment

The scanning cavity microscope enables the spatially resolved investigation of the optical properties of nanostructures deposited on the surface of one of the cavity mirrors. Placing individual particles on a mirror at air comes with many advantages: the sample is robust and has in principle an infinite lifetime which allows for an extensive measurement time. The high contrast of the refractive indices of sample and environment ensures a high measurement signal. But this method excludes a major part of nanostructures: biological nanosystems like proteins or viruses.

Proteins are the fundamental building blocks of life. Thus it is worth to investigate them to get deeper insights in the basic processes enabling life and to learn about their structure and their dynamics.

Life is strongly related to the presence of water: without water life is not possible and thus proteins show only in aqueous environment a behaviour like in living beings [145]. Thus it is necessary to study them in water.

Individual native biological molecules can in general not be detected with standard light microscopy or comparable techniques. Therefore an immense bunch of methods to detect and to investigate biological nanosystems has been developed over the last decades. Most of these methods either rely on labelling the particle with fluorophores and detecting them with methods of fluorescence microscopy and spectroscopy [78, 79, 146] or on binding the particle to some functionalized transducer that converts the binding of the molecule of interest to the sensor into a measurable optical [147, 148] or electrical signal [149].

Within the optical sensors, whispering gallery mode resonators have found wide interest [29, 150]. Optical whispering gallery mode resonators are based on an optical mode circulating on the circumference of a spherical, cylindrical, toroidal or planar ring-like micro structure of glass or any other optically transparent material. By observing the shift of the resonator's resonance frequency, the binding of single molecules to its surface can be monitored with

very high sensitivity [151]. By enhancing the electrical field of the whispering gallery mode locally using plasmonic nanostructures like a metal nanorod, single binding events of DNA [152] or the passage of an individual atomic ion can be detected [31].

Particle sensors based on whispering gallery mode resonators rely on binding of particles to the resonator's surface which eventually influences the particle properties or on a stochastic passage of particles in the close vicinity of the resonator. Thus studies on the dynamics of the particles like diffusion or motional and rotational dynamics are barely possible.

A method to access this information is fluorescence correlation microscopy [153]. Here, a confocal microscope, focused to a dilute solution of the nanostructures of interest, marked with suitable fluorophores, is used. While the particle diffuses through the focus, its fluorescence signal is recorded. From the autocorrelation of the signal, the hydrodynamical properties of the particle, especially the hydrodynamic radius can be measured. This number quantifies the size of the particle by comparing it to the diffusion properties of a solid sphere. The radius of a sphere with equivalent properties than the particle under investigation is called hydrodynamic radius of the object. Furthermore, chemical processes inferring with the fluorescence rate of the particle, that are slower or faster than the diffusion rate can be characterized using advanced mathematical models fitted to the autocorrelation of the fluorescence signal.

To combine the sensitivity of optical resonators with the ability of detecting molecular dynamics of fluorescence correlation microscopy, fibre-based micro Fabry-Pérot resonators can be used. Figure 5.1 illustrates the basic scheme of such a Fabry-Pérot cavity combined with a microfluidic environment for characterisation of biological particles in an aqueous environment. In the following section, the actual implementation is presented.

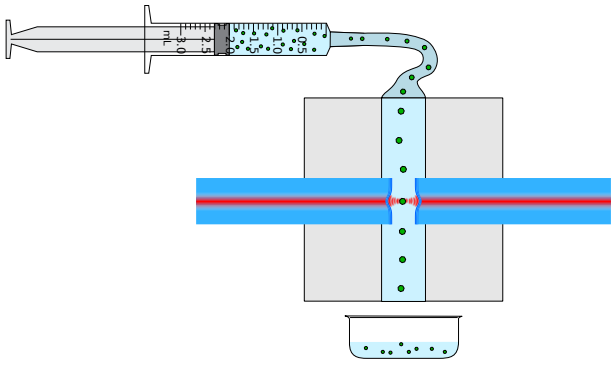

Figure 5.1: Concept of Fabry-Pérot micro resonator based sensing of nanostructures in an aqueous environment. The cavity set up of two micro machined optical fibres with mirrors on the opposing end facets embedded to a fluid channel in the size of the fibres. By injecting a dilute solution (or dispersion) of nanoparticles (depicted in green) to this channel e.g. with a syringe pump, the particles are brought to the cavity.

In contrast to whispering gallery mode resonators, where only an evanescent field of the resonator mode at the surface of the resonator structure can interact

with the nanoobject, the mode volume of a Fabry-Pérot resonator is fully accessible for the particle. On the one hand, the direct access to the cavity mode allows for a stronger interaction of the cavity mode with the particle and opens on the other hand the possibility for novel measurement schemes [154].

Biological nanoparticles are small (diameter around 10 nm [10]) and only weakly absorbing in the visible and near infrared [155]. Furthermore, the dielectric constants for biomolecules are only roughly known [156], thus particle detection methods sensitive to the real part of its polarizability are demanded. In the following a selection of possible measurement schemes to detect the dispersion and scattering, both dependent on the real part of the particle's polarizability, using a Fabry-Pérot cavity are proposed.

Frequency Shift of the Cavity A particle inside the cavity shifts its resonance frequency. By locking the cavity to a laser of fixed frequency[1] [158], the servo signal of the lock can be used as an indicator for particles. The detection sensitivity can be further increased by detecting the phase shift of the cavity due to the particle by an homodyne detection scheme. A realisation of the locking method is presented in the next section.

Elastic Scattering When a nanoparticle crosses the mode of a robustly locked cavity as described above, light gets scattered our of the resonator. On the one hand, this light reduces the transmission of the cavity which allows for a direct measurement of the extinction cross section of the particle. On the other hand, the light scattered out of the cavity can be detected. An observation of scattered light orthogonal to the cavity axis allows for an in principle background free measurement and thus a very high sensitivity to the single photon level. This makes the detection of extremely small objects possible. A simple example of this method is shown within this chapter.

By illuminating the cavity from the side, the resonator can be used to enhance and efficiently collect the scattered light by a particle inside [159].

Inelastic Scattering Either the cavity mode or light sent through the resonator orthogonally to its axis can scatter at particles inside inelastically. By a suitable design of cavity length and mirror, it is possible to scatter light from one to an other longitudinal mode which are at the same time resonant. Both approaches allow Raman spectroscopy at a single particle inside the resonator [115, 116].

Using a heterodyne detection scheme for the detection of single photons can further increase the sensitivity of scattering measurements.

Trapping and Cooling Besides detecting and characterizing a particle passing the cavity, the resonator mode can also be used to catch and trap the particle. The cavity mode acts as optical tweezers or as a dipole trap and a probe for the particle at the same time. By Raman-sideband cooling it is possible to cool

[1]The other way round, locking the laser to the cavity, is in principle possible, too. Due to the short cavity, small length fluctuations are converted to relatively large frequency shifts which have to be followed by the laser. The fast tuning range of common (diode) lasers is in general not sufficiently large. This problem could be overcome by injection locking the laser to the cavity [157].

the trapped particle without using internal electronic transitions [69, 160]. The possibility to fix the particle's position allows to study internal particle dynamics like binding of further molecules, proteins ect. to the particle, conformation changes or chemical reactions, triggered by adding further particles or reactants to the fluid or by light with temporal resolution.

External optical tweezers can be used to periodically bring a particle or an extent protein strain spanned between two particles serving as handles for the tweezers to the resonator. Using a lock-in detector can increase the sensitivity and could open the possibility for force-dependent optical measurements on protein strains.

Photothermal Absorption Spectroscopy To investigate the absorption of a particle, it can be illuminated with a laser close to its absorption frequency. The absorbed light leads to heating of the local environment of the particle and thus to a slight change of the refractive index. This index change can be detected by the resonator. By sweeping the heating laser frequency, it is possible to do investigate the absorption of the particle with spectral resolution. For not inferring with the spectroscopy light, the wavelength of the cavity probe light and eventually the trapping light has to be far off the particle's absorption lines.

All these potential experiments highlight the versatility of a Fabry-Pérot micro cavity in an liquid environment. To prove, whether it is possible to combine a high-finesse optical resonator that requires extremely clean mirrors, high mechanical stability in a very well controlled environment with the world of biological nanosystems that is ruled by fluctuations and impurities, a first prove of concept experiment is shown in the following.

A microfluidc cell with integrated cavity has been set up comprising a simple laser system and cavity lock electronics. This setup is introduced in the next section. With this setup fist measurement on glass nanospheres have been done and are shown in the last section of the chapter.

5.2 Experimental Setup

5.2.1 Microfluidic Cell for the Cavity

To combine the microscopic volume of a fibre-based Fabry-Pérot micro resonator with a liquid environment, a microfluidic cell is used. This cell is on the one hand the mount for the cavity fibres, thus it has to be very robust and stable and on the other hand it contains channels guiding the liquids into the cavity in a very controlled way.

Microfluidic cells are a well established technique in many fields of life-science, chemistry and physics [161, 162]. In contrast to common cells, which are planar devices where the fluid channels are etched to glass or imprinted to plastic, here a very stable device of a more advanced and very precise three dimensional shape is needed to combine the cavity mounting with the fluidics.

The setup of the microfluidic cell is shown in figure 5.2, the circled letters in the following description refer to the labels there. The fluid channels as well as the mounting for the fibres is milled in a *MACOR*[2] block Ⓕ. To insert

[2] A machinable glass-ceramic by *Corning* that is chemically inert and mechanically very stable.

different liquids, three input channels unite in a Ψ-shaped trifurcation just before the cavity. The channels have a size of 300 µm × 300 µm. The depth is given by the diameter of the fibre including space for alignment, while the width is determined by the smallest milling tools available. The channels are covered by a lid of CO_2-laser cut fused silica Ⓐ in order to ensure optical access to the cavity.

Syringe needles are glued to the liquid inlets and the outlet (not shown in the figure). The Luer-Lock connectors of the needles allow to use standard and thus cost efficient hospital supplies for connection tubing, filters and syringes.

The liquid flow through the cell is controlled with three computer-operated syringe pumps (*World Precision Instruments Aladdin AL-1000*). As these pumps are entry-level devices, they cannot ensure a sufficiently smooth flow of the liquids at the demanded extremely low flow rates.

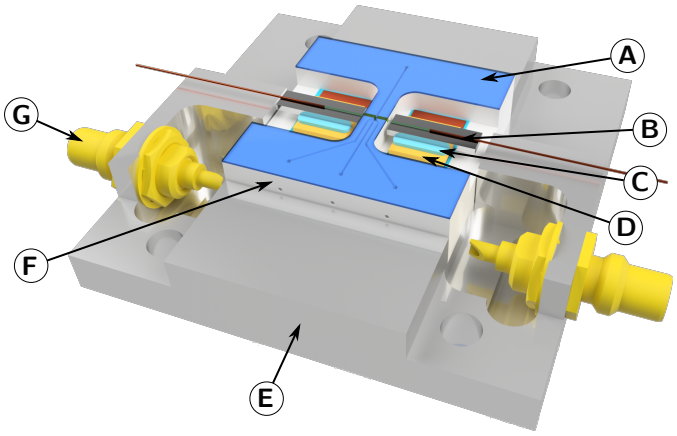

(a) Overview of the microfluidic cell

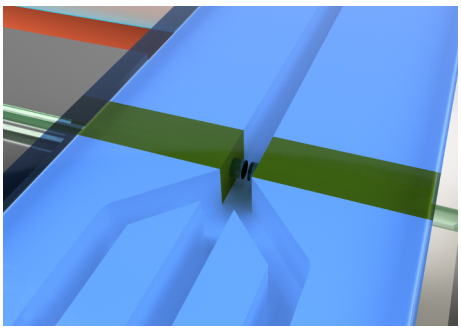

(b) Detailed view of the trifurcation of the input channels and the cavity.

Figure 5.2: Setup of a micro Fabry-Pérot cavity inside a microfluidic cell. The components are described within the text.

The cavity is set up of a single mode and a multi mode optical fibre. The concave mirrors fabricated to their end facets have radii of curvature of around 200 µm and 100 µm receptively and have a high reflective mirror coating centred

arround 780 nm by *ATF* (transmission 12 ppm, losses 12 ppm see section 3.2.6). Both fibres are glued onto silicon v-groove plates Ⓑ for easier handling at the fibre alignment. These plates are glued Ⓒ to shear piezo chips Ⓓ for cavity length adjustment.

The fibres are placed in the centre of the fluid channel. The opposing fibres are aligned to form a cavity with optimal coupling to the fundamental mode using an external 5-axis micro positioner (*Elliot Scientific MDE187*). The cavity length is chosen such, that the cavity is close to resonance when filled with air or water. Due to drifts during the curing of the glue, this goal could not be achieved.

The fibres are sealed with respect to the liquid channel with a slightly elastic glue (*EPO-TEC 113-91-5*). This glue, used for all gluing in the setup is a low shrinkage dual cure epoxy that can be pre-cured using uv-light to fix the component and it is hard cured by heat.

Due to the fibres glued to the microfluidic cells, their freedom of movement is very limited. The maximum excursion of each fibre with the maximum voltage applied to the piezos is around 10 nm. Because of the little range of tunability of the cavity length, the resonator cannot always be tuned to resonance by adjusting the cavity length. In this case, the laser wavelength has to be adjusted.

The whole cell is glued to a temperature stabilized platform Ⓕ. This platform includes SMC-connectors Ⓖ for the piezos and ensures thermalization of the liquid as the syringe needles used for supplying the cell are directly attached to this platform.

The temperature stabilized platform together with the microfluidic cell is mounted on a 3-axes positioning stage (*Newport ULTRAlign M-562*) to align the cell with respect to a microscope for observing the light scattered out of the cavity.

5.2.2 Optics and Electronics

To probe and stabilize the cavity inside the microfluidic cell, only very simple and reduced optics and electronics are needed. Figure 5.3 shows the whole optical and electronic setup.

Optics To illuminate the cavity, a tunable grating stabilized diode laser at a wavelength of 765 nm to 785 nm is used (*Toptica DLpro*). The wavelength of the laser is monitored with a fibre-coupled wavemeter (*Burleigh WA-1500*). The power of the light is controlled with a $\lambda/2$-plate and a polarizing beamsplitter. For optimal coupling of the light to a polarization maintaining fibre, the polarization state is adjusted using a $\lambda/2$-plate and $\lambda/4$-plate.

For locking the resonator, sidebands are imprinted to the laser with a fibre-coupled electro-optic modulator (*Photline*[3] *NIR-MPX800-LN-05*). The single mode fibre of the cavity is but-coupled to the output fibre of the modulator.

To control the polarization state of the light inside the cavity, the non-polarization maintaining input fibre of the resonator is built into a 3-paddle polarization controller [163, 164].

The transmitted light of the cavity is fed to an avalanche photodiode (*Thorlabs PDA110*) with a bandwith of 50 MHz.

[3] now IXblue

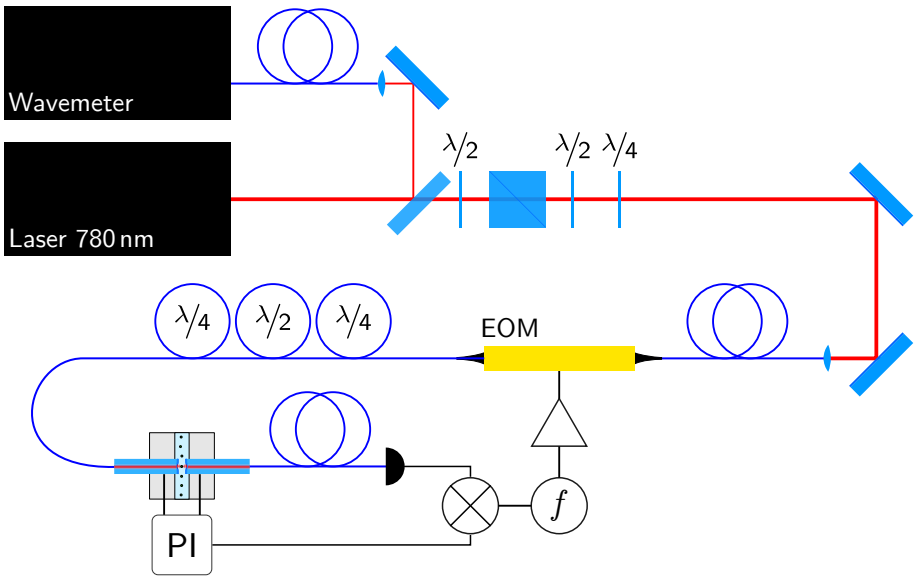

Figure 5.3: Optics and electronics to probe and stabilize the cavity attached to a microfluidic cell.

The light scattered out of the cavity is collected with an infinite corrected long working distance microscope objective (*Leitz Wetzlar*[4] $\infty/0$ *Plan L25x/0.40*) and imaged (focal length 175 mm) to a CMOS-camera (*IDS Imaging DCC1545M-GL*).

Cavity Locking Electronics The cavity is locked to resonance using a modified Pound-Drewer-Hall locking scheme [165]. In contrast to the common Pound-Drever-Hall scheme, here the modulation frequency of the probe light is smaller than the cavity line with and the error signal is generated from the transmitted light. For fibre-based cavities this scheme is advantageous, as offset drifts of the lock signal due to standing wave effects in the input fibre are avoided [158].

The locking is facilitated by the very high mechanical stiffness of the resonator. Due to the fibres fixed at the microfluidic cell, the resonance stays nearly at rest for many seconds before slowly drifting away. This makes a simple manual capture of the lock feasible. Furthermore, a photothermal bistability of the cavity [32, 158] enables a self stabilization of the cavity: the high intracavity power absorbed by the first coating layers leads to a thermal expansion of the coating counteracting a length increase of the resonator.

Due to this effect the resonance is broadened when scanning over it by increasing the cavity length and a narrowed when reducing the cavity length as illustrated in figure 5.4. In contrast to the effect reported so far, where the left flank of the resonance counteracts the increasing cavity length, here it is the right flank of the resonance, that compensates for the increasing length. While the reported behaviour is well understood, the observed effect here remains unexplained and further investigation is required.

[4] now Leica

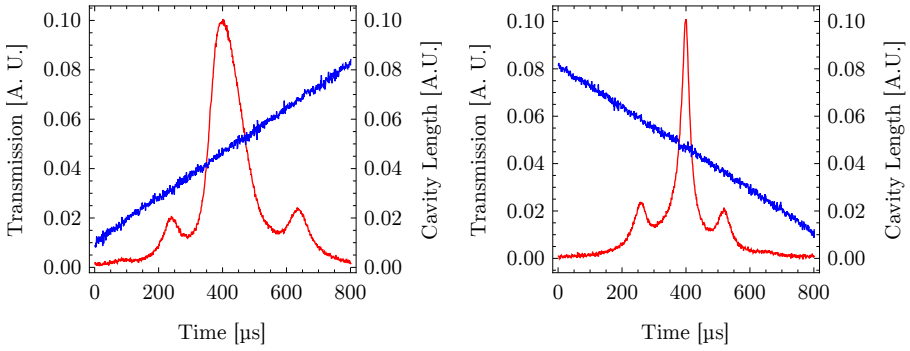

(a) Increasing cavity length.

(b) Decreasing cavity length.

Figure 5.4: Transmission of the cavity when scanning over the resonance (red) in dependence on the cavity length (blue) at constant scan rate. Due to the photothermal bistability of the resonator, the cavity resonance gets broadened or narrowed for increasing or decreasing cavity length. Besides the main peaks sidebands imprinted to the laser are visible.

Furthermore, the effect depends on the speed, the cavity is scanned over the resonance. The slower the scanning, the more pronounced is the bistability. Figure 5.5 shows the resonances of the resonator observed at different scan rates.

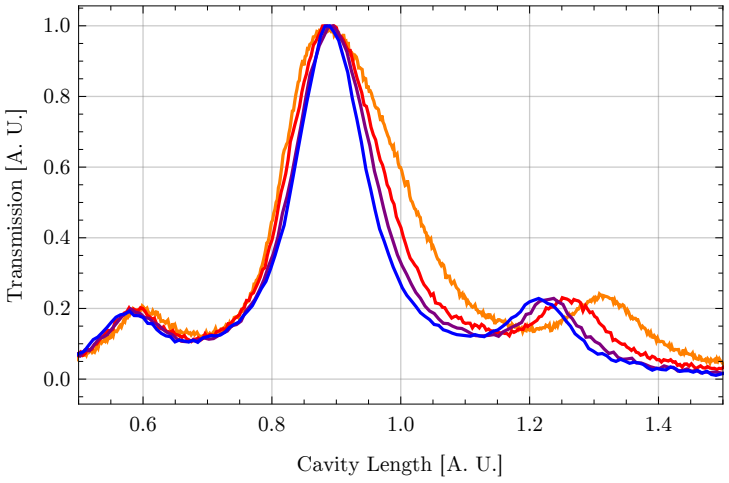

Figure 5.5: Transmission of the cavity when scanning over the resonance for scan rates of 50 Hz (orange), 100 Hz (red), 200 Hz (purple) and 500 Hz (blue). The slower the sweep over the resonance, the more pronounced is the line broadening due to the photothermal bistability.

Due to these self-stabilizing effects and the high mechanical stability, the cavity can be locked using a standard lockbox (*Anton Scheich: LB5*). The integral part of the PI loop is amplified using a high voltage operational am-

plifier (*Texas Instruments OPA454*) and fed to one piezo of the cavity. The proportional part of the PI loop is directly fed to the second piezo.

The error signal for the lock is generated using an integrated lock module (*Anton Scheich: RF-Lock*) that modulates the laser via the electro-optical modulator with a frequency of 50 MHz. The modulation signal is amplified (*Miteq AM-1299*) before it is sent to the modulator. The transmission signal recorded by the photodiode is mixed with this local oscillator and the resulting signal is fed to the lockbox.

To observe the transmission of the cavity, the dc part of the photodiode signal is branched of with a bias tee (*Mini-Circuits ZFBT-6G+*).

The contamination of the cavity mirrors with all kind of dirt turned out to be a constant companion of the experiments. To remove dirt by ultra sonic cleaning, a frequency generator with a frequency of 100 kHz has been integrated to the lock electronics allowing for a quick switching between cavity locking and cavity cleaning. While the fibres are shaked with high frequency, the channels are flushed with clean liquid.

5.3 First Results

In this section, first results of fused silica spheres with a diameter of 142 nm[5] are shown. As the experiment was intended as a prove of concept to check whether it is in principle possible to combine nanoparticles in an aqueous environment with a high finesse optical cavity, no quantitative studies were made. A rapid degradation of the cavity in combination with various experimental challenges due to the lack of experience with such a system prevented a systematic investigation.

Nevertheless it had been possible to gather some data: particles have flushed to the resonator, got possibly trapped by the cavity mode, and the scattered light and the error signal of the lock have been recorded. Furthermore, the passage of individual particles through the cavity has been observed by evaluating the transmission signal of the locked cavity.

5.3.1 Detecting Particles with the Cavity

The first try of injecting nanoparticles to the cavity was dedicated to observe light scattered by the particles out of the locked cavity. A highly diluted dispersion of fused silica spheres was injected to the central channel of the cell. The two outer channels were connected to clean water reservoirs for flushing the cavity. It turned out, that if all three channels are operated simultaneously, a laminar flow arises where the three channels barely mix. By adjusting the flow rate of the outer channels, it was possible to direct the central channel containing the nanoparticles to the centre of the cavity. By modulating the faint particle flow, it was possible to accumulate particles in the cavity and to flush them out without the cavity falling out of lock.

The scattered light has been recorded with a camera looking orthogonally to the cavity while the lock signal, counteracting the resonance frequency changes of the cavity due to the particles has been stored with an oscilloscope. Both signals have been recorded synchronized to each other.

[5] Micro Particles GmbH, Lot: SiO_2-F-L2897

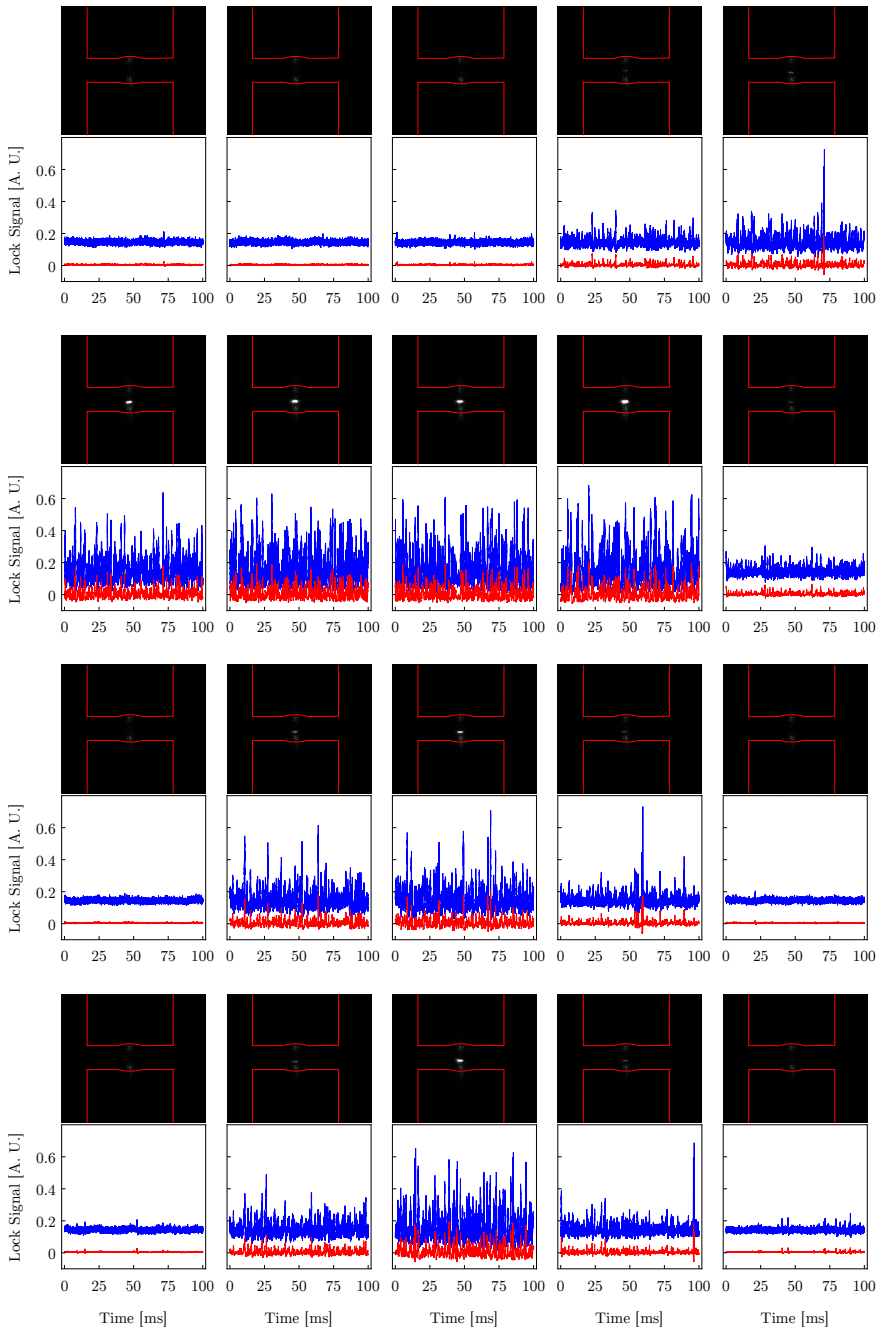

Figure 5.6: Images of the locked cavity with trapped nanoparticles and the corresponding integral (blue) and proportional (red) part of the cavity lock signal. Particles are sequentially injected. The light scattered by the particle is visible between the highlighted contours of the resonator (mirror shapes not to scale). The time spacing between two subsequent images is around 1 s.

Figure 5.6 shows the images of the scattered light out of the resonator and the corresponding integral and proportional part of the lock signal. The exposure time of each image as well as the length of the oscilloscope time trace was 100 ms. The spacing between subsequent images was around 1 s.

Particles were sequentially injected to the cavity. When particles are present in the resonator, visible by a bright spot between the cavity fibres, the lock signals show nervous and large excursions. The more particles present the brighter the spot and the higher the excursions of the lock.

The frequency components of the lock signal of the cavity without and with particles inside are shown in power spectra in figure 5.7. When particles are present, especially low frequency components show an increased amplitude. The peak at the integral signal at 2.2 kHz might be related to the lock electronics.

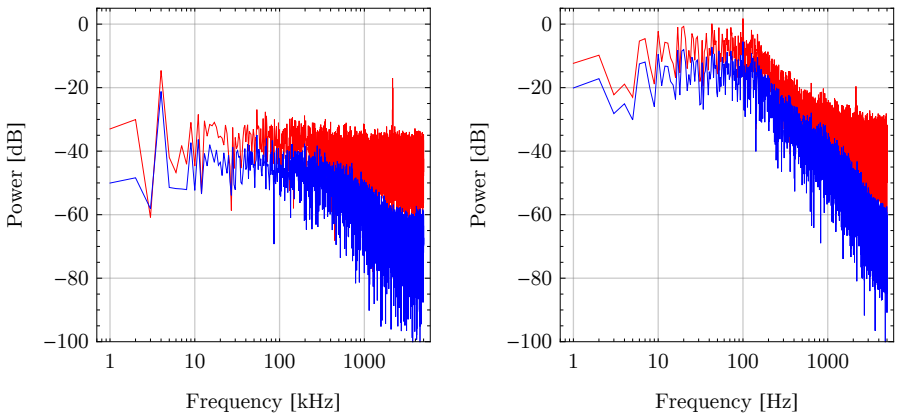

(a) Without particles.

(b) With particles.

Figure 5.7: Power spectra of the cavity lock signals without and with particles inside the resonator: integral part (red) and proportional part (blue). The data corresponds to the first graph of the first and second row in figure 5.6.

Due to degradation of the cavity, it was not possible to repeat the experiment and to measure the amount of scattered light quantitatively.

5.3.2 Dynamics of Particles Passing the Cavity

The wiggling lock signal of the cavity when particles are trapped shown in the previous section suggests, that particles inside the resonator don't stay at rest but move around. To further investigate the dynamics of individual particles, the transmission of the locked cavity when single particles pass the mode has been investigated. Therefore, an even more dilute dispersion of particles as before was injected to the resonator and events due to particles have been recorded.

Figure 5.8 shows the transmission of the resonator when a particle passes the mode. The transition time of it is measured by fitting a Gaussian to the envelope of the signal. The fit gives a time of 9.6 ms to pass the $1/e^2$ radius of the cavity mode. Compared to a transition time of 1.5 ms obtained from the flow rate of the injected liquid of 0.25 mL/h (rate set by syringe pumps), the

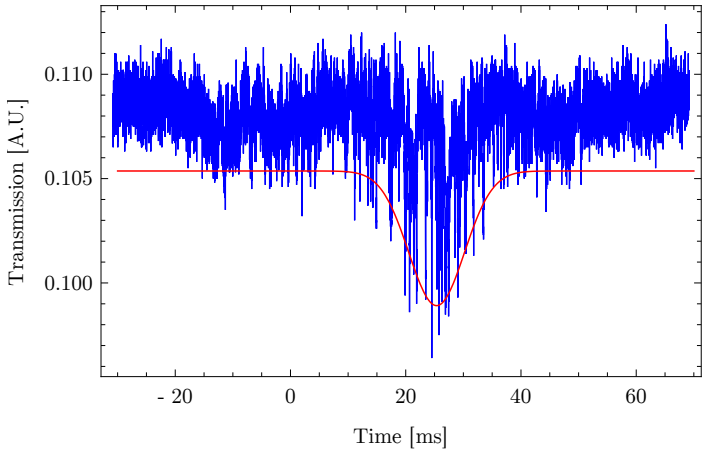

Figure 5.8: Transmission of the locked resonator while an individual particle is passing (blue) and a Gaussian fit to the envelope of the signal (red) to measure the transition time.

cross section of the fluid channel at the cavity of approximately $0.04\,\mathrm{mm}^2$ and the mode waist of $3\,\mu\mathrm{m}$, the observed transition time suggests that the cavity might decelerate and trap the particle before it is flushed out the resonator by the liquid flow.

A further hint for the trapping of the particle is the temporal structure of the extinction dips in the transmission signal.

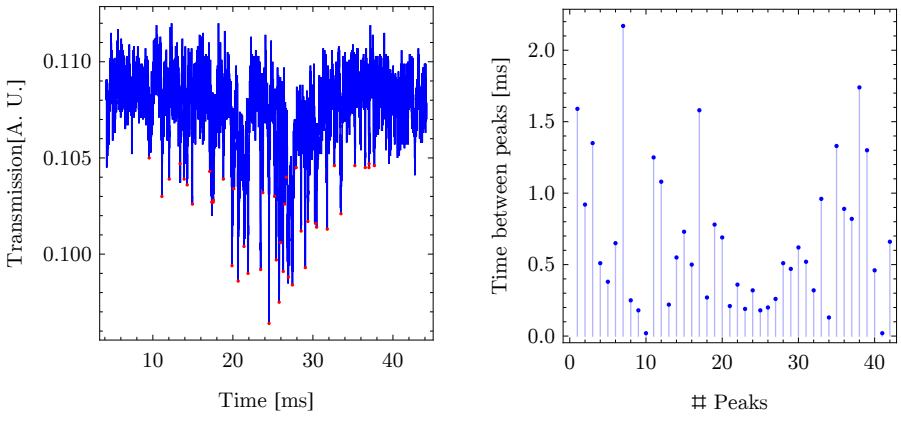

(a) Extinction dips (red dots) in the transmission signal (blue) of the cavity.

(b) Time between two subsequent peaks.

Figure 5.9: Temporal dynamics of the extinction signal of a particle passing the cavity.

Figure 5.9(a) shows again the transmission of the locked cavity when a parti-

cle passes the mode. The extinction minima are highlighted[6]. The time between two neighbouring dips is plotted in figure 5.9(b).

The spacing between two extinction dips shows roughly a bimodal distribution: large spacings and in between a larger number of smaller spacings. For the particle dynamics within the cavity, this suggests a behaviour as illustrated in figure 5.10. The particle entering the resonator mode is trapped by an antinode of the mode. The particle wiggles around, which would correspond to the small spacings between the extinction dips, before jumping to a neighbouring antinode corresponding to large spacings. The dips themselves might appear when the particle crosses the field maximum in the centre of the antinode.

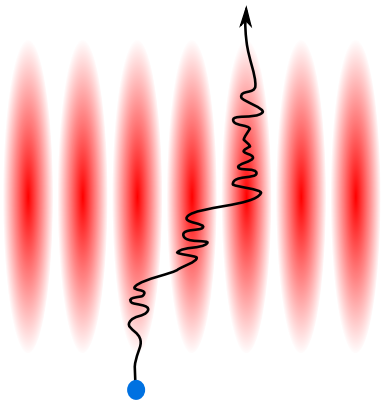

Figure 5.10: Possible path of the particle through the cavity mode: the particle is trapped by an antinode of the resonator, wiggles around within the antinode, jumps to an other one, wiggles around there and so on until the particle leaves the resonator mode driven by the flow of the surrounding liquid.

The large number of small spacings in the beginning of the second half of the signal could be a hint for the energy loss of the particle and the trapping in the centre of the mode where the field and thus the confinement is highest. The particle might flushed out of the resonator by the flow of the liquid.

For particles trapped in a cavity in vacuum, comparable signals have been observed [69].

This measurement could only be performed once before degradation of the cavity. To approve all effects described, further systematic studies using a more robust setup are necessary.

The usage of a high-NA objective to collect the scattered light due to a particle in the resonator together with advanced particle localisation could allow for studying the dynamics of the particle with antinode-site precision within the standing wave of the resonator as routinely done in cold atom physics [166–168].

Although the experiments with a Fabry-Pérot cavity within a microfluidic cell were dominated by cumbersome and futile cleaning of the resonator, the experiments have shown the potential of such a resonator in an aqueous environment.

[6]The retrieval of the minima is tricky as the noise of the lock has a comparable frequency than the extinction dips that are assumed to be due to the passing particle.

By observing the signals of the cavity lock, scattered light out of the cavity and the light transmitted through the locked resonator it has been possible to detect particles. First hints for particle trapping and on particle dynamics within the standing wave of the resonator could be found for an individual optically transparent nanoobject without the need for labelling or functionalizing it.

In a next step, the problem of contaminating the resonator has to be faced. By hydrophobic coating of the mirrors, e.g. by silanization [169], the contact with water and thus dirt could be reduced. Cavity losses due to water absorption could be reduced by a change in wavelength from 780 nm to the visible red region around 600 nm where still extraordinary low loss mirror coatings are available.

The particle flow control can be optimized by using pressurized air controlled flow controllers designed for the requirements in microfluidics. With fast and precise flow control and a optimized channel design it might get possible to use on the one hand the shown Ψ-geometry for improved positioning of the sample flow with respect to the cavity exploiting the laminar flow at low Reynolds-numbers as in a microfluidic device. On the other hand, adding additional channels with good flow control would enable novel experiments like the triggering of chemical reactions and observation of their dynamics.

Good control and understanding of the cavity in a microfluidic device opens the doors to many intriguing and novel experiments in nano- and bio-physics.

Chapter 6

Conclusion and Outlook

Scanning cavity microscopy has been introduced in this work as a versatile tool for sensitive detection and quantitative characterization of individual nanoparticles with spatial resolution. By measuring the extinction cross section as well as the dispersion due to a particle, it became possible to quantify its complex polarizability, the quantity that fully describes the optical properties of nanoparticles in the Rayleigh limit.

Within this work, such a microscope has been realized. It is based on a robust mechanical apparatus that allows for automatized wide-range raster-scanning of the plane mirror, carrying the samples with respect to the second cavity mirror applied to the micro-machined end-facet of an optical fibre.

To fabricate suitable mirror structures to end-facets of optical fibres, a CO_2 laser-based setup for efficient and precise machining and characterization of these structures has been developed within this work.

By analysing the transmission spectrum of the resonator illuminated with light at a fixed wavelength, the optical properties of the resonator and thus of the samples are measured. From the amplitude or the linewidth, the extinction of various gold nanoparticles has been analysed, achieving a sensitivity down to $1.7\,\mathrm{nm}^2$. Because of the high accuracy of the microscope, it has been possible to measure the extinction cross section distribution of gold nanospheres with diameters of 40 nm and 50 nm with very good agreement to a calculated distribution.

The ellipticity of the fibre mirrors leads to a splitting of each mode into two orthogonally polarized resonances. This splitting has been exploited for differential extinction as well as dispersion measurements of gold nanorods to retrieve a correlation between the extinction contrast and the birefringence of the particles and to investigate the influence of anisotropic particles on the cavity polarization state.

By exploiting the lifted degeneracy of higher order transverse modes, the dispersion due to a particle could be measured although the mechanical setup is not stable enough to keep the cavity on resonance while scanning the plane mirror, which would allow to observe slight length changes due to the nanoparticle's dispersion. Instead, the 2^{nd} order higher transverse modes have been used: While a particle at the centre of the TEM11 mode leaves the resonance frequency unchanged, the frequencies of the TEM02 and TEM20 mode are shifted. From the spacing between the three modes, the dispersion has been deduced.

To bring these three modes closer together in order to measure their spacing with only little influence of mechanical noise, high-frequency sidebands have been modulated to the laser. Using advanced online data evaluation made measurements of the frequency spacing with a sensitivity of 195 MHz or well below one linewidth possible while ensuring a high measurement speed.

As a strong background modulation in the order of the expected dispersion signal of gold nanospheres has been observed on the plane mirror, a differential measurement scheme has been introduced. By subtracting a dispersion measurement of the plane mirror with and without samples, aligned to each other by markers, applied with the CO_2 laser to the mirror, a more than fourfold reduction of the background could be achieved. This procedure enabled a precise measurement of the dispersion due to gold nanospheres. Together with the simultaneously performed extinction measurement, the polarizability of the nanospheres could be quantified.

Inspired from the squeezing of modes of the quantum harmonic oscillator in order to reduce the position or momentum uncertainty, a novel scheme for spatial resolution enhancement by combining higher order transverse cavity modes has been developed. By linear combination of extinction maps taken with the fundamental and subsequent higher order transverse modes, a significant improvement of spatial resolution while keeping the quantitative properties of the measurement has been demonstrated. This scheme holds the potential to beat the diffraction limit by simply combining images taken with different Laguerre- or Hermite-Gaussian modes.

All measurements have been limited by mode mixing, that disturbed especially the extinction measurements and prevented a free choice of the longitudinal mode order for microscopy. To circumvent mode mixing, suitable mode orders, with only little disturbance due to mixing have been chosen and mixing has tried to be avoided by angular alignment of the resonator. In future experiments, mode mixing could be further reduced by using fibre-mirrors with a more spherical profile, fabricated by multi-shot laser machining [99], which is facilitated by the presented CO_2 laser setup.

Measuring the Polarizability Tensor

For non-symmetrical particles the polarizability is a tensorial quantity. In a next step, this tensor, at least in in the plane of the mirror, the particle is placed to, can be measured with the scanning cavity microscope. By taking advantage of the splitting of each cavity mode into two orthogonally polarized resonances, the dispersion and extinction of a particle can be retrieved along both polarization axes. As this requires a fibre with a sufficiently elliptic mirror, a homogeneous coupling to all three modes of the 2^{nd} order of higher transverse modes and the possibility to split these three modes together with the fundamental mode into the two polarization states, this procedure is challenging, as it has been unsuccessfully tried using several fibres within this work. Furthermore, this scheme is restricted to the polarization axes defined by the geometry of the fibre mirror.

The progress in the laser machining of fibre ends allows for the fabrication of nearly perfectly rotationally symmetrical mirror profiles [99]. With such fibres, the modes of each transverse order are degenerate. Thus, a particle inside the resonator would lift the degeneracy which can be detected by observing the

line shape of the transmission signal. In addition, the polarization state of the resonator mode could be chosen freely. An anisotropic particle would change the polarization of the mode. By measuring the full polarization state of the resonator mode, smallest polarization state changes can be observed and thus the polarizability tensor of a particle can be determined with high precision.

To overcome the inhomogeneous coupling to the higher order cavity modes due to imperfect mode matching, the fibres can be equipped by further mode matching optics like a small piece of gradient index fibre [170]. Another possibility to improve mode matching can be a mirror fabricated to the tip of a microaxicon by laser machining. The geometry of the axicon would still allow for short cavities with good angular adjustability but gives the chance to use conventional mode matching optics for optimally coupling light to the resonator.

A precise measurement of the polarizability tensor of nearly any nanoparticle opens the possibility to optically investigate nanosystems whose optical properties are barely accessible, like many biomolecules, e.g. DNA.

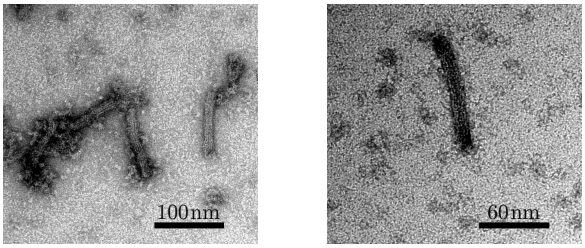

(a) 10 pmol/ml (b) 5 pmol/ml

Figure 6.1: TEM images of 24 helix bundle DNA origami structures at different concentrations and magnifications. Origami and images by Luisa Kneer.

As light can damage DNA, which can, on a long and large scale, result in cancer, it is interesting to study the optical properties of DNA strands. To investigate DNA strands with scanning cavity microscopy, it can be folded to defined structures using the technique of DNA origami [171]. Figure 6.1 shows around 100 nm long rods formed by a well defined bundle of 24 DNA helices. These bundles are large enough to be detected with the scanning cavity microscope and would allow for refractive index measurements of individual bundles.

Towards Liquid Environments

The natural environment of most biological nanosystems like proteins is water. The scanning cavity microscope as presented in this work is dedicated to study nanosystems in a dry environment.

In order to be able to investigate spatial dynamics or systems that degrade with time, the measurement speed has to be increased, which can be done by a much stiffer mechanical setup. By adding a controlled drop of fluid around fibre tip and plane mirror enables spatially resolved investigation of samples in an aqueous environment like biomembranes. It could be possible to investigate transportation processes through a cell membrane by locating and characterizing various transportation proteins. Furthermore the tracking of vesicles, that try

to attach to the membrane and the investigation of the attachment process itself could provide novel insights into cell biology.

Another concept to unite a cavity and an aqueous environment has been presented in this work: Adding a high-finesse fibre-based microcavity to a microfluidic channel makes the detection of particles passing the cavity possible. By observing the interaction of passing particles with the resonator or by trapping them either with the cavity mode itself or with optical tweezers, particle dynamics can be studied. In contrast to most other methods, the cavity approach allows for binding- and label-free measurement on nearly undisturbed nanosystems like proteins. By advanced trapping of the object, it is possible to rotate the object [172] within the cavity, which enables a polarizability tomography [173] of the particle and thus a reconstruction of the full three dimensional polarizability tensor.

Scanning cavity microscopy is a novel tool that allows to measure the full optical properties of nanosystems within a single measurement. This will make it possible to get much deeper insight in many nanosystems, that have not been accessible by optical methods so far.

Bibliography

[1] F. E. Wagner, S. Haslbeck, L. Stievano, S. Calogero, Q. A. Pankhurst, and K.-P. Martinek, "Before striking gold in gold-ruby glass", Nature **407**, 691–692 (2000).

[2] A. Ruivo, C. Gomes, A. Lima, M. L. Botelho, R. Melo, A. Belchior, and A. P. de Matos, "Gold nanoparticles in ancient and contemporary ruby glass", Journal of Cultural Heritage **9**, e134–e137 (2008).

[3] P. Colomban, "The use of metal nanoparticles to produce yellow, red and iridescent colour, from bronze age to present times in lustre pottery and glass: solid state chemistry, spectroscopy and nanostructure", Journal of Nano Research **8**, 109–132 (2009).

[4] Y. Lu, S. Sathasivam, J. Song, C. R. Crick, C. J. Carmalt, and I. P. Parkin, "Robust self-cleaning surfaces that function when exposed to either air or oil", Science **347**, 1132–1135 (2015).

[5] P.-J. Lu, S.-C. Huang, Y.-P. Chen, L.-C. Chiueh, and D. Y.-C. Shih, "Analysis of titanium dioxide and zinc oxide nanoparticles in cosmetics", Journal of Food and Drug Analysis **23**, 587–594 (2015).

[6] K. Cho, X. Wang, S. Nie, Z. Chen, and D. M. Shin, "Therapeutic nanoparticles for drug delivery in cancer", Clinical Cancer Research **14**, 1310–1316 (2008).

[7] A. L. Rogach et al., "Light-emitting diodes with semiconductor nanocrystals", Angewandte Chemie International Edition **47**, 6538–6549 (2008).

[8] J. Weickert, R. B. Dunbar, H. C. Hesse, W. Wiedemann, and L. Schmidt-Mende, "Nanostructured organic and hybrid solar cells", Advanced Materials **23**, 1810–1828 (2011).

[9] J. K. Stolarczyk, S. Bhattacharyya, L. Polavarapu, and J. Feldmann, "Challenges and prospects in solar water splitting and CO_2 reduction with inorganic and hybrid nanostructures", ACS Catalysis **8**, 3602–3635 (2018).

[10] R. Milo and R. Philips, *Cell biology by the numbers*, (2015) `http://book.bionumbers.org/how-big-is-the-average-protein/` (visited on 05/30/2018).

[11] H. Siedentopf and R. Zsigmondy, "Über Sichtbarmachung und Größenbestimmung ultramikoskopischer Teilchen, mit besonderer Anwendung auf Goldrubingläser", Annalen der Physik **315**, 1–39 (1902).

[12] P. Zijlstra and M. Orrit, "Single metal nanoparticles: optical detection, spectroscopy and applications", Reports on Progress in Physics **74**, 106401 (2011).

[13] K. Lindfors, T. Kalkbrenner, P. Stoller, and V. Sandoghdar, "Detection and spectroscopy of gold nanoparticles using supercontinuum white light confocal microscopy", Physical Review Letters **93**, 037401 (2004).

[14] P. Kukura, H. Ewers, C. Müller, A. Renn, A. Helenius, and V. Sandoghdar, "High-speed nanoscopic tracking of the position and orientation of a single virus", Nature Methods **6**, 923–927 (2009).

[15] Y.-H. Lin, W.-L. Chang, and C.-L. Hsieh, "Shot-noise limited localization of single 20 nm gold particles with nanometer spatial precision within microseconds", Optics Express **22**, 9159 (2014).

[16] M. Piliarik and V. Sandoghdar, "Direct optical sensing of single unlabelled proteins and super-resolution imaging of their binding sites", Nature Communications **5**, 4495 (2014).

[17] P. Kukura, M. Celebrano, A. Renn, and V. Sandoghdar, "Single-molecule sensitivity in optical absorption at room temperature", The Journal of Physical Chemistry Letters **1**, 3323–3327 (2010).

[18] M. Celebrano, P. Kukura, A. Renn, and V. Sandoghdar, "Single-molecule imaging by optical absorption", Nature Photonics **5**, 95–98 (2011).

[19] A. Arbouet, D. Christofilos, N. D. Fatti, F. Vallée, J. R. Huntzinger, L. Arnaud, P. Billaud, and M. Broyer, "Direct measurement of the single-metal-cluster optical absorption", Physical Review Letters **93**, 127401 (2004).

[20] O. Muskens, D. Christofilos, N. D. Fatti, and F. Vallée, "Optical response of a single noble metal nanoparticle", Journal of Optics A: Pure and Applied Optics **8**, S264–S272 (2006).

[21] O. L. Muskens, N. D. Fatti, F. Vallée, J. R. Huntzinger, P. Billaud, and M. Broyer, "Single metal nanoparticle absorption spectroscopy and optical characterization", Applied Physics Letters **88**, 063109 (2006).

[22] O. L. Muskens, G. Bachelier, N. D. Fatti, F. Vallée, A. Brioude, X. Jiang, and M.-P. Pileni, "Quantitative absorption spectroscopy of a single gold nanorod", The Journal of Physical Chemistry C **112**, 8917–8921 (2008).

[23] D. Boyer, P. Tamarat, A. Maali, B. Lounis, and M. Orrit, "Photothermal imaging of nanometer-sized metal particles among scatterers", Science **297**, 1160–1163 (2002).

[24] S. Berciaud, L. Cognet, G. A. Blab, and B. Lounis, "Photothermal heterodyne imaging of individual nonfluorescent nanoclusters and nanocrystals", Physical Review Letters **93**, 257402 (2004).

[25] S. Berciaud, D. Lasne, G. A. Blab, L. Cognet, and B. Lounis, "Photothermal heterodyne imaging of individual metallic nanoparticles: Theory versus experiment", Physical Review B **73**, 257402 (2006).

[26] T. Juffmann, B. B. Klopfer, T. L. I. Frankort, P. Haslinger, and M. A. Kasevich, "Multi-pass microscopy", Nature Communications **7**, 12858 (2016).

[27] S. Nimmrichter, C.-F. Chen, B. B. Klopfer, M. A. Kasevich, and T. Juffmann, "Full-field cavity enhanced microscopy techniques", (2017), arXiv:1704.05217v1 [quant-ph].

[28] T. Juffmann, S. A. Koppell, B. B. Klopfer, C. Ophus, R. M. Glaeser, and M. A. Kasevich, "Multi-pass transmission electron microscopy", Scientific Reports **7**, 1699 (2017).

[29] F. Vollmer and S. Arnold, "Whispering-gallery-mode biosensing: label-free detection down to single molecules", Nature Methods **5**, 591–596 (2008).

[30] F. Vollmer and L. Yang, "Review label-free detection with high-Q microcavities: a review of biosensing mechanisms for integrated devices", Nanophotonics **1**, 267–291 (2012).

[31] M. D. Baaske and F. Vollmer, "Optical observation of single atomic ions interacting with plasmonic nanorods in aqueous solution", Nature Photonics **10**, 733–739 (2016).

[32] D. Hunger, T. Steinmetz, Y. Colombe, C. Deutsch, T. W. Hänsch, and J. Reichel, "A fiber Fabry-Perot cavity with high finesse", New Journal of Physics **12**, 065038 (2010).

[33] D. Hunger, C. Deutsch, R. J. Barbour, R. J. Warburton, and J. Reichel, "Laser micro-fabrication of concave, low-roughness features in silica", AIP Advances **2**, 012119 (2012).

[34] M. Uphoff, M. Brekenfeld, G. Rempe, and S. Ritter, "Frequency splitting of polarization eigenmodes in microscopic Fabry-Perot cavities", New Journal of Physics **17**, 013053 (2015).

[35] H. Kelkar, D. Wang, D. Martín-Cano, B. Hoffmann, S. Christiansen, S. Götzinger, and V. Sandoghdar, "Sensing nanoparticles with a cantilever-based scannable optical cavity of low finesse and sub-λ^3-volume", Physical Review Applied **4**, 054010 (2015).

[36] H. C. van de Hulst, *Light scattering by small particles (dover books on physics)* (Dover Publications, 1981).

[37] M. Quinten, *Optical properties of nanoparticle systems* (Wiley VCH Verlag GmbH, Jan. 11, 2011).

[38] G. Mie, "Beiträge zur Optik trüber Medien, speziell kolloidaler Metallösungen", Annals of Physics **330**, 377–445 (1908).

[39] M. Born, *Optik* (Springer, 1932).

[40] K. L. Kelly, E. Coronado, L. L. Zhao, and G. C. Schatz, "The optical properties of metal nanoparticles: The influence of size, shape, and dielectric environment", The Journal of Physical Chemistry B **107**, 668–677 (2003).

[41] S. W. Prescott and P. Mulvaney, "Gold nanorod extinction spectra", Journal of Applied Physics **99**, 123504 (2006).

[42] P. Drude, "Zur Elektronentheorie der Metalle", Annalen der Physik **306**, 566–613 (1900).

[43] N. D. M. Neil W. Ashcroft, *Solid state physics* (Holt-Saunders International Editors, 1981).

[44] U. Kreibig, "Small silver particles in photosensitive glass: their nucleation and growth", Applied Physics **10**, 255–264 (1976).

[45] P. B. Johnson and R. W. Christy, "Optical constants of the noble metals", Physical Review B **6**, 4370–4379 (1972).

[46] O. L. Muskens, P. Billaud, M. Broyer, N. D. Fatti, and F. Vallée, "Optical extinction spectrum of a single metal nanoparticle: Quantitative characterization of a particle and of its local environment", Physical Review B **78**, 205410 (2008).

[47] M. M. Wind, J. Vlieger, and D. Bedeaux, "The polarizability of a truncated sphere on a substrate I", Physica A: Statistical Mechanics and its Applications **141**, 33–57 (1987).

[48] M. Wind, P. Bobbert, J. Vlieger, and D. Bedeaux, "The polarizability of a truncated sphere on a substrate II", Physica A: Statistical Mechanics and its Applications **143**, 164–182 (1987).

[49] L. Novotny and B. Hecht, *Principles of nano-optics* (Cambridge University Pr., Sept. 11, 2012).

[50] S. Furman and A. Tikhonravov, *Basics of optics of multilayer systems* (World Scientific Publishing Co Pte Ltd, 1996).

[51] F. Métivier, "Pérot ou Perot?", Photoniques **25** (2006).

[52] M. Mader, "A cavity nanoscope", MA thesis (Ludwig-Maximilians Universität München, 2012).

[53] B. E. A. Saleh and M. C. Teich, *Grundlagen der Photonik* (Wiley VCH Verlag GmbH, Mar. 11, 2008).

[54] H. Kogelnik and T. Li, "Laser beams and resonators", Applied Optics **5**, 1550 (1966).

[55] J. L. Hall, J. Ye, and L.-S. Ma, "Measurement of mirror birefringence at the sub-ppm level: proposed application to a test of QED", Physical Review A **62**, 013815 (2000).

[56] B. Brandstätter et al., "Integrated fiber-mirror ion trap for strong ion-cavity coupling", Review of Scientific Instruments **84**, 123104 (2013).

[57] W. B. Joyce and B. C. DeLoach, "Alignment of gaussian beams", Applied Optics **23**, 4187 (1984).

[58] D. Z. Anderson, "Alignment of resonant optical cavities", Applied Optics **23**, 2944 (1984).

[59] J. Gallego, S. Ghosh, S. K. Alavi, W. Alt, M. Martinez-Dorantes, D. Meschede, and L. Ratschbacher, "High-finesse fiber Fabry-Perot cavities: stabilization and mode matching analysis", Applied Physics B **122**, 47 (2016).

[60] J. Benedikter, "Transverse-mode coupling and diffraction loss in fibre-based optical microcavities", Master Thesis (Ludwig-Maximilians-Universität München, Sept. 30, 2014).

[61] J. Benedikter, T. Hümmer, M. Mader, B. Schlederer, J. Reichel, T. W. Hänsch, and D. Hunger, "Transverse-mode coupling and diffraction loss in tunable Fabry-Pérot microcavities", New Journal of Physics **17**, 053051 (2015).

[62] N. Podoliak, H. Takahashi, M. Keller, and P. Horak, "Harnessing the mode mixing in optical fiber-tip cavities", Journal of Physics B: Atomic, Molecular and Optical Physics **50**, 085503 (2017).

[63] S. Nimmrichter, K. Hammerer, P. Asenbaum, H. Ritsch, and M. Arndt, "Master equation for the motion of a polarizable particle in a multimode cavity", New Journal of Physics **12**, 083003 (2010).

[64] H. J. Kimble, "Strong interactions of single atoms and photons in cavity QED", Physica Scripta **T76**, 127 (1998).

[65] H. Tanji-Suzuki, I. D. Leroux, M. H. Schleier-Smith, M. Cetina, A. T. Grier, J. Simon, and V. Vuletić, "Interaction between atomic ensembles and optical resonators", in *Advances in atomic, molecular, and optical physics* (Elsevier, 2011), pp. 201–237.

[66] A. Wickenbrock, M. Hemmerling, G. R. M. Robb, C. Emary, and F. Renzoni, "Collective strong coupling in multimode cavity QED", Physical Review A **87**, 043817 (2013).

[67] P. T. Kristensen, C. V. Vlack, and S. Hughes, "Generalized effective mode volume for leaky optical cavities", Optics Letters **37**, 1649 (2012).

[68] J. Vuckovic, "Quantum optics and cavity qed with quantum dots in photonic crystals", (2014), arXiv:`1402.2541v1 [quant-ph]`.

[69] P. Asenbaum, S. Kuhn, S. Nimmrichter, U. Sezer, and M. Arndt, "Cavity cooling of free silicon nanoparticles in high vacuum", Nature Communications **4**, 2743 (2013).

[70] T. Hänsch and B. Couillaud, "Laser frequency stabilization by polarization spectroscopy of a reflecting reference cavity", Optics Communications **35**, 441–444 (1980).

[71] S. Moriwaki, H. Sakaida, T. Yuzawa, and N. Mio, "Measurement of the residual birefringence of interferential mirrors using Fabry-Perot cavity", Applied Physics B: Lasers and Optics **65**, 347–350 (1997).

[72] F. Brandi, F. D. Valle, A. D. Riva, P. Micossi, F. Perrone, C. Rizzo, G. Ruoso, and G. Zavattini, "Measurement of the phase anisotropy of very high reflectivity interferential mirrors", Applied Physics B: Lasers and Optics **65**, 351–355 (1997).

[73] H. von Helmholtz, "Die theoretische Grenze für die Leistungsfähigkeit der Mikroskope", Annalen der Physik und Chemie, 557–584 (1874).

[74] Rayleigh, "XXXI. Investigations in optics, with special reference to the spectroscope", Philosophical Magazine Series 5 **8**, 261–274 (1879).

[75] H. Volkmann, "Ernst abbe and his work", Applied Optics **5**, 1720 (1966).

[76] E. Abbe, *Die Lehre von der Bildentstehung im Mikroskop*, edited by O. Lummer (Vieweg, 1910), 108 pp.

[77] U. Z. Wolfgang Zinth, *Optik* (Gruyter, de Oldenbourg, Mar. 27, 2013), 342 pp.

[78] S. W. Hell, "Far-field optical nanoscopy", Science **316**, 1153–1158 (2007).

[79] E. Betzig, G. H. Patterson, R. Sougrat, O. W. Lindwasser, S. Olenych, J. S. Bonifacino, M. W. Davidson, J. Lippincott-Schwartz, and H. F. Hess, "Imaging intracellular fluorescent proteins at nanometer resolution", Science **313**, 1642–1645 (2006).

[80] S. Quabis, R. Dorn, M. Eberler, O. Glöckl, and G. Leuchs, "Focusing light to a tighter spot", Optics Communications **179**, 1–7 (2000).

[81] R. Dorn, S. Quabis, and G. Leuchs, "Sharper focus for a radially polarized light beam", Physical Review Letters **91**, 233901 (2003).

[82] Y. Kozawa and S. Sato, "Sharper focal spot formed by higher-order radially polarized laser beams", Journal of the Optical Society of America A **24**, 1793 (2007).

[83] C. Gerry and P. Knight, *Introductory quantum optics* (Cambridge University Press, 2004).

[84] P. Zupancic, P. M. Preiss, R. Ma, A. Lukin, M. E. Tai, M. Rispoli, R. Islam, and M. Greiner, "Ultra-precise holographic beam shaping for microscopic quantum control", Optics Express **24**, 13881 (2016).

[85] P. Horak, H. Ritsch, T. Fischer, P. Maunz, T. Puppe, P. W. H. Pinkse, and G. Rempe, "Optical kaleidoscope using a single atom", Physical Review Letters **88**, 043601 (2002).

[86] S. Gigan, L. Lopez, N. Treps, A. Maître, and C. Fabre, "Image transmission through a stable paraxial cavity", Physical Review A **72**, 023804 (2005).

[87] M. Tsang, R. Nair, and X.-M. Lu, "Quantum theory of superresolution for two incoherent optical point sources", Physical Review X **6**, 031033 (2016).

[88] F. Yang, A. Tashchilina, E. S. Moiseev, C. Simon, and A. I. Lvovsky, "Far-field linear optical superresolution via heterodyne detection in a higher-order local oscillator mode", Optica **3**, 1148 (2016).

[89] M. Paur, B. Stoklasa, Z. Hradil, L. L. Sanchez-Soto, and J. Rehacek, "Achieving quantum-limited optical resolution", (2016), arXiv:`1606.08332v1 [quant-ph]`.

[90] B. P. Abbott et al., "LIGO: The laser interferometer gravitational-wave observatory", Reports on Progress in Physics **72**, 076901 (2009).

[91] B. Abbott et al., "GW151226: Observation of gravitational waves from a 22-solar-mass binary black hole coalescence", Physical Review Letters **116**, 241103 (2016).

[92] D. G. Matei et al., "A second generation of low thermal noise cryogenic silicon resonators", Journal of Physics: Conference Series **723**, 012031 (2016).

[93] Y. Colombe, T. Steinmetz, G. Dubois, F. Linke, D. Hunger, and J. Reichel, "Strong atom-field coupling for Bose-Einstein condensates in an optical cavity on a chip", Nature **450**, 272–276 (2007).

[94] R. J. Thompson, G. Rempe, and H. J. Kimble, "Observation of normal-mode splitting for an atom in an optical cavity", Physical Review Letters **68**, 1132–1135 (1992).

[95] J. Reichel, W. Hänsel, and T. W. Hänsch, "Atomic micromanipulation with magnetic surface traps", Physical Review Letters **83**, 3398–3401 (1999).

[96] W. Hänsel, P. Hommelhoff, T. W. Hänsch, and J. Reichel, "Bose–einstein condensation on a microelectronic chip", Nature **413**, 498–501 (2001).

[97] T. Steinmetz, Y. Colombe, D. Hunger, T. W. Hänsch, A. Balocchi, R. J. Warburton, and J. Reichel, "Stable fiber-based Fabry-Pérot cavity", Applied Physics Letters **89**, 111110 (2006).

[98] H. Kaupp et al., "Purcell-enhanced single-photon emission from nitrogen-vacancy centers coupled to a tunable microcavity", Physical Review Applied **6**, 054010 (2016).

[99] K. Ott, S. Garcia, R. Kohlhaas, K. Schüppert, P. Rosenbusch, R. Long, and J. Reichel, "Millimeter-long fiber Fabry-Perot cavities", Optics Express **24**, 9839 (2016).

[100] R. Gehr, J. Volz, G. Dubois, T. Steinmetz, Y. Colombe, B. L. Lev, R. Long, J. Estève, and J. Reichel, "Cavity-based single atom preparation and high-fidelity hyperfine state readout", Physical Review Letters **104**, 203602 (2010).

[101] F. Haas, J. Volz, R. Gehr, J. Reichel, and J. Esteve, "Entangled states of more than 40 atoms in an optical fiber cavity", Science **344**, 180–183 (2014).

[102] H. Takahashi, A. Wilson, A. Riley-Watson, F. Oručević, N. Seymour-Smith, M. Keller, and W. Lange, "An integrated fiber trap for single-ion photonics", New Journal of Physics **15**, 053011 (2013).

[103] T. G. Ballance, H. M. Meyer, P. Kobel, K. Ott, J. Reichel, and M. Köhl, "Cavity-induced backaction in Purcell-enhanced photon emission of a single ion in an ultraviolet fiber cavity", Physical Review A **95**, 033812 (2017).

[104] C. Toninelli, Y. Delley, T. Stöferle, A. Renn, S. Götzinger, and V. Sandoghdar, "A scanning microcavity for in situ control of single-molecule emission", Applied Physics Letters **97**, 021107 (2010).

[105] R. Albrecht, A. Bommer, C. Deutsch, J. Reichel, and C. Becher, "Coupling of a single nitrogen-vacancy center in diamond to a fiber-based microcavity", Physical Review Letters **110**, 243602 (2013).

[106] E. Janitz, M. Ruf, M. Dimock, A. Bourassa, J. Sankey, and L. Childress, "Fabry-Perot microcavity for diamond-based photonics", Physical Review A **92**, 043844 (2015).

[107] J. Benedikter et al., "Cavity-enhanced single-photon source based on the silicon-vacancy center in diamond", Physical Review Applied **7**, 024031 (2017).

[108] S. Bogdanović, M. S. Z. Liddy, S. B. van Dam, L. C. Coenen, T. Fink, M. Lončar, and R. Hanson, "Robust nano-fabrication of an integrated platform for spin control in a tunable microcavity", APL Photonics **2**, 126101 (2017).

[109] M. Förg, L. Colombier, R. K. Patel, J. Lindlau, A. D. Mohite, H. Yamaguchi, D. Hunger, and A. Högele, "Cavity-control of bright and dark interlayer excitons in van der Waals heterostructures", (2017), arXiv:1710.00990v2 [cond-mat.mes-hall].

[110] N. E. Flowers-Jacobs, S. W. Hoch, J. C. Sankey, A. Kashkanova, A. M. Jayich, C. Deutsch, J. Reichel, and J. G. E. Harris, "Fiber-cavity-based optomechanical device", Applied Physics Letters **101**, 221109 (2012).

[111] S. Stapfner, L. Ost, D. Hunger, J. Reichel, I. Favero, and E. M. Weig, "Cavity-enhanced optical detection of carbon nanotube Brownian motion", Applied Physics Letters **102**, 151910 (2013).

[112] A. B. Shkarin, N. E. Flowers-Jacobs, S. W. Hoch, A. D. Kashkanova, C. Deutsch, J. Reichel, and J. G. E. Harris, "Optically mediated hybridization between two mechanical modes", Physical Review Letters **112**, 013602 (2014).

[113] A. D. Kashkanova et al., "Superfluid brillouin optomechanics", Nature Physics **13**, 74–79 (2016).

[114] T. F. Langerfeld, H. M. Meyer, and M. Köhl, "Correlated-photon-pair emission from a cw-pumped Fabry-Perot microcavity", Physical Review A **97**, 023822 (2018).

[115] B. Petrak, N. Djeu, and A. Muller, "Purcell-enhanced raman scattering from atmospheric gases in a high-finesse microcavity", Physical Review A **89**, 023811 (2014).

[116] T. Hümmer, J. Noe, M. S. Hofmann, T. W. Hänsch, A. Högele, and D. Hunger, "Cavity-enhanced Raman microscopy of individual carbon nanotubes", Nature Communications **7**, 12155 (2016).

[117] H. Kaupp, "Coupling nitrogen-vacancy centers in diamond to fiber-based Fabry-Pérot microcavities", PhD Thesis (Ludwig-Maximilians-Universität München, 2017).

[118] U. C. Paek and A. L. Weaver, "Formation of a spherical lens at optical fiber ends with a CO_2 laser", Applied Optics **14**, 294 (1975).

[119] L. Collot, V. Lefèvre-Seguin, M. Brune, J. M. Raimond, and S. Haroche, "Very high-Q whispering-gallery mode resonances observed on fused silica microspheres", Europhysics Letters (EPL) **23**, 327–334 (1993).

[120] C. Deutsch, "High finesse fibre Fabry-Perot resonators - Production, chracterisation and applications.", Diplomarbeit (Ludwig-Maximilians Universität München, 2008).

[121] B. Schlederer, "Development of a CO_2 laser setup for fiber end facet machining and characterization", Master Thesis (Ludwig-Maximilians Universität München, 2014).

[122] P. de Groot, "Principles of interference microscopy for the measurement of surface topography", Advances in Optics and Photonics **7**, 1 (2015).

[123] K. G. Larkin, "Efficient nonlinear algorithm for envelope detection in white light interferometry", Journal of the Optical Society of America A **13**, 832 (1996).

[124] P. Hariharan, B. F. Oreb, and T. Eiju, "Digital phase-shifting interferometry: A simple error-compensating phase calculation algorithm", Applied Optics **26**, 2504 (1987).

[125] M. A. Herráez, D. R. Burton, M. J. Lalor, and M. A. Gdeisat, "Fast two-dimensional phase-unwrapping algorithm based on sorting by reliability following a noncontinuous path", Applied Optics **41**, 7437 (2002).

[126] LASEROPTIK, *Catalog 2017*, tech. rep. (LASEROPTIK GmbH, 2017).

[127] M. Weiser, "spektroskopische Temperaturmessung an dielektrisch verspiegelten Glasfasern", Bachelor Thesis (Ludwig-Maximilians Universität München, 2016).

[128] B. Chéron, H. Gilles, J. Hamel, O. Moreau, and H. Sorel, "Laser frequency stabilization using Zeeman effect", Journal de Physique III **4**, 401–406 (1994).

[129] K. L. Corwin, Z.-T. Lu, C. F. Hand, R. J. Epstein, and C. E. Wieman, "Frequency-stabilized diode laser with the Zeeman shift in an atomic vapor", Applied Optics **37**, 3295 (1998).

[130] M. L. Harris, S. L. Cornish, A. Tripathi, and I. G. Hughes, "Optimization of sub-doppler DAVLL on the rubidium D2 line", Journal of Physics B: Atomic, Molecular and Optical Physics **41**, 085401 (2008).

[131] P. Pokrowsky, W. Zapka, F. Chu, and G. C. Bjorklund, "High frequency wavelength modulation spectroscopy with diode lasers", Optics Communications **44**, 175–179 (1983).

[132] G. C. Bjorklund, "Frequency-modulation spectroscopy: a new method for measuring weak absorptions and dispersions", Optics Letters **5**, 15 (1980).

[133] C. J. Foot, *Atomic physics*, Oxford Master Series in Physics (Oxford University Press, 2005).

[134] T. W. Hänsch, I. S. Shahin, and A. L. Schawlow, "High-resolution saturation spectroscopy of the sodium D-lines with a pulsed tunable dye laser", Physical Review Letters **27**, 707–710 (1971).

[135] L. Ricci, M. Weidemüller, T. Esslinger, A. Hemmerich, C. Zimmermann, V. Vuletic, W. König, and T. W. Hänsch, "A compact grating-stabilized diode laser system for atomic physics", Optics Communications **117**, 541–549 (1995).

[136] K. Levenberg, "A method for the solution of certain non-linear problems in least squares", Quarterly of Applied Mathematics **2**, 164–168 (1944).

[137] D. W. Marquardt, "An algorithm for least-squares estimation of nonlinear parameters", Journal of the Society for Industrial and Applied Mathematics **11**, 431–441 (1963).

[138] M.-C. Daniel and D. Astruc, "Gold nanoparticles: assembly, supramolecular chemistry, quantum-size-related properties, and applications toward biology, catalysis, and nanotechnology", Chemical Reviews **104**, 293–346 (2004), eprint: `https://doi.org/10.1021/cr030698+`.

[139] H. E. Toma, V. M. Zamarion, S. H. Toma, and K. Araki, "The coordination chemistry at gold nanoparticles", Journal of the Brazilian Chemical Society **21**, 1158–1176 (2010).

[140] MicroChemicals GmbH, *Ätzen von Gold*, (Nov. 7, 2013) `http://www.microchemicals.de/technische_infos/gold_aetzen.pdf` (visited on 04/11/2018).

[141] D. A. Rosen and A. R. Tao, "Modeling the optical properties of bowtie antenna generated by self-assembled ag triangular nanoprisms", ACS Applied Materials & Interfaces **6**, 4134–4142 (2014).

[142] A. M. Funston, C. Novo, T. J. Davis, and P. Mulvaney, "Plasmon coupling of gold nanorods at short distances and in different geometries", Nano Letters **9**, 1651–1658 (2009).

[143] P. K. Jain and M. A. El-Sayed, "Plasmonic coupling in noble metal nanostructures", Chemical Physics Letters **487**, 153–164 (2010).

[144] A. F. Stewart, S. M. Lu, M. M. Tehrani, and C. Volk, "Ion beam sputtering of optical coatings", in Laser-induced damage in optical materials: 1993, edited by H. E. Bennett, L. L. Chase, A. H. Guenther, B. E. Newnam, and M. J. Soileau (July 1994).

[145] P. L. Privalov and C. Crane-Robinson, "Role of water in the formation of macromolecular structures", European Biophysics Journal **46**, 203–224 (2016).

[146] T. Ha and P. Tinnefeld, "Photophysics of fluorescent probes for single-molecule biophysics and super-resolution imaging", Annual Review of Physical Chemistry **63**, 595–617 (2012).

[147] S. M. Borisov and O. S. Wolfbeis, "Optical biosensors", Chemical Reviews **108**, 423–461 (2008).

[148] P. Damborský, J. Švitel, and J. Katrlík, "Optical biosensors", Essays In Biochemistry **60**, 91–100 (2016).

[149] D. Grieshaber, R. MacKenzie, J. Vörös, and E. Reimhult, "Electrochemical biosensors - Sensor principles and architectures", Sensors **8**, 1400–1458 (2008).

[150] M. R. Foreman, J. D. Swaim, and F. Vollmer, "Whispering gallery mode sensors", Advances in Optics and Photonics **7**, 168 (2015).

[151] J. Zhu, S. K. Ozdemir, Y.-F. Xiao, L. Li, L. He, D.-R. Chen, and L. Yang, "On-chip single nanoparticle detection and sizing by mode splitting in an ultrahigh-Q microresonator", Nature Photonics **4**, 46–49 (2009).

[152] M. D. Baaske, M. R. Foreman, and F. Vollmer, "Single-molecule nucleic acid interactions monitored on a label-free microcavity biosensor platform", Nature Nanotechnology **9**, 933–939 (2014).

[153] S. T. Hess, S. Huang, A. A. Heikal, and W. W. Webb, "Biological and chemical applications of fluorescence correlation spectroscopy: A review", Biochemistry **41**, 697–705 (2002).

[154] A. A. P. Trichet, J. Foster, N. E. Omori, D. James, P. R. Dolan, G. M. Hughes, C. Vallance, and J. M. Smith, "Open-access optical microcavities for lab-on-a-chip refractive index sensing", Lab Chip **14**, 4244–4249 (2014).

[155] J. C. Sutherland and K. P. Griffin, "Absorption spectrum of dna for wavelengths greater than 300 nm", Radiation Research **86**, 399–410 (1981).

[156] L. Li, C. Li, Z. Zhang, and E. Alexov, "On the dielectric constant of proteins: smooth dielectric function for macromolecular modeling and its implementation in DelPhi", Journal of Chemical Theory and Computation **9**, 2126–2136 (2013).

[157] B. Dahmani, L. Hollberg, and R. Drullinger, "Frequency stabilization of semiconductor lasers by resonant optical feedback", Optics Letters **12**, 876 (1987).

[158] J. F. S. Brachmann, H. Kaupp, T. W. Hänsch, and D. Hunger, "Photothermal effects in ultra-precisely stabilized tunable microcavities", Optics Express **24**, 21205 (2016).

[159] M. Motsch, M. Zeppenfeld, P. W. H. Pinkse, and G. Rempe, "Cavity-enhanced rayleigh scattering", New Journal of Physics **12**, 063022 (2010).

[160] N. Kiesel, F. Blaser, U. Delic, D. Grass, R. Kaltenbaek, and M. Aspelmeyer, "Cavity cooling of an optically levitated submicron particle", Proceedings of the National Academy of Sciences **110**, 14180–14185 (2013).

[161] T. M. Squires and S. R. Quake, "Microfluidics: fluid physics at the nanoliter scale", Reviews of Modern Physics **77**, 977–1026 (2005).

[162] G. M. Whitesides, "The origins and the future of microfluidics", Nature **442**, 368–373 (2006).

[163] R. Ulrich, S. C. Rashleigh, and W. Eickhoff, "Bending-induced birefringence in single-mode fibers", Optics Letters **5**, 273 (1980).

[164] H. C. Lefevre, "Single-mode fibre fractional wave devices and polarisation controllers", Electronics Letters **16**, 778 (1980).

[165] E. D. Black, "An introduction to pound–drever–hall laser frequency stabilization", American Journal of Physics **69**, 79–87 (2001).

[166] W. S. Bakr, J. I. Gillen, A. Peng, S. Fölling, and M. Greiner, "A quantum gas microscope for detecting single atoms in a hubbard-regime optical lattice", Nature **462**, 74–77 (2009).

[167] P. Würtz, T. Langen, T. Gericke, A. Koglbauer, and H. Ott, "Experimental demonstration of single-site addressability in a two-dimensional optical lattice", Physical Review Letters **103**, 080404 (2009).

[168] J. F. Sherson, C. Weitenberg, M. Endres, M. Cheneau, I. Bloch, and S. Kuhr, "Single-atom-resolved fluorescence imaging of an atomic mott insulator", Nature **467**, 68–72 (2010).

[169] B. Seed, "Silanizing glassware", Current Protocols in Cell Biology **8**, A.3E.1–A.3E.2 (2000).

[170] G. K. Gulati, H. Takahashi, N. Podoliak, P. Horak, and M. Keller, "Fiber cavities with integrated mode matching optics", Scientific Reports **7**, 5556 (2017).

[171] S. M. Douglas, H. Dietz, T. Liedl, B. Högberg, F. Graf, and W. M. Shih, "Self-assembly of DNA into nanoscale three-dimensional shapes", Nature **459**, 414–418 (2009).

[172] L. Paterson, "Controlled rotation of optically trapped microscopic particles", Science **292**, 912–914 (2001).

[173] M. Habaza, B. Gilboa, Y. Roichman, and N. T. Shaked, "Tomographic phase microscopy with 180° rotation of live cells in suspension by holographic optical tweezers", Optics Letters **40**, 1881 (2015).

Publications and Conference Contributions

Publications

- M. Mader, J. Reichel, T. W. Hänsch, D. Hunger, "A scanning cavity microscope." Nature Communications **6** 7249 (2015)
- J. Benedikter, T. Hümmer, M. Mader, B. Schlederer, J. Reichel, T. W. Hänsch, D. Hunger, "Transverse-mode coupling and diffraction lass in tunable Fabry-Pérot microcavities", New Journal of Physics **17** 053051 (2015)
- H. Kaupp, T. Hümmer, M. Mader, B. Schlederer, J. Benedikter, P. Haeusser, Huan-Cheng Chang, Helmut Fedder, T. W. Hänsch, D. Hunger, "Purcell-Enhanced Single-Photon Emission from Nitrogen-Vacancy Centers Coupled to a Tunable Microcavity", Physical Review Applied **6** 054010 (2016)

Conference Contributions

Talks

- DPG Frühjahrstagung Sektion AMOP 2014, Berlin: *A Scanning Cavity Microscope*
- DPG Frühjahrstagung Sektion SKM 2015, Berlin: *A Scanning Cavity Microscope*
- DPG Frühjahrstagung Sektion AMOP 2015, Heidelberg: *A Scanning Cavity Microscope*
- CLEO Europe 2015, München: *A Scanning Cavity Microscope*
- DPG Frühjahrstagung Sektion AMOP 2017, Mainz: *Measuring the Polarizability of Individual Nanoparticles*

Posters

- DPG Frühjahrstagung Sektion AMOP 2013, Hannover: *A Cavity Nanoscope*
- Conference on Resonator QED 2013, München: *A Scanning Cavity Microscope*

- NIM Workshop Young Ideas in Nanoscience 2013, München: *A Scanning Cavity Microscope*
- DPG Frühjahrstagung Sektion AMOP 2014, Berlin: *A Scanning Cavity Microscope*
- DPG Frühjahrstagung Sektion AMOP 2015, Heidelberg: *A Scanning Cavity Microscope*
- DPG Frühjahrstagung Sektion AMOP 2016, Hannover: *A Scanning Cavity Microscope*
- NIM Workshop Young Ideas in Nanoscience 2017, München: *Microcavity-based Spectroscopy of Individual Nanoparticles*

Further Outreach

Out of the underwater cavity project, a science slam[1] talk entitled *Seeing the invisible. – How to detect transparent nanoparticles* (*Unsichtbares sehen. – Wie man durchsichtige Nanoteilchen detektiert*) arose. Amongst other science slams, this talk won the science slam in the international year of light by the Max-Planck Society in Berlin 2015 and the southern German pre-selection in Ravensburg of the German science slam championship in Darmstadt 2016. It took part at the European science slam championship in Brno (Czech Republic) 2017.

[1] A scientific talk competition, where scienctists present their research to a wide audience within a limited time (mainly 10 min).

Danksagung

Am Ende dieser Arbeit bleibt der Blick zurück auf viele Ergebnisse, der Nährboden aber, dem sie entsprungen sind, bleibt verborgen. Dieser Boden war entscheidend und Voraussetzung für das Gelingen dieser Arbeit. Ich bin froh und dankbar zugleich, dass ich diese Arbeit in einem besonders fruchtbaren und inspirierenden Umfeld anfertigen konnte.

Was dieses Umfeld ausmacht, sind die Menschen. Ihnen allen bin ich dankbar.

Zuerst danke ich Herrn Prof. Hänsch für die fast unbesehene Aufnahme in seine Abteilung als Doktorand. Ich danke für das damit verbundene Vertrauen, die Freiheit Neues auszuprobieren und auch Nebenwege beschreiten zu können. Das offene, hilfsbereite, immer diskussionsfreudige und kreative Klima in der Abteilung war Ansporn und Grundlage für viele Ideen.

Der grenzenlose Optimismus und die unbändige Begeisterung meines Betreuers Prof. David Hunger mögen mich manchmal herausgefordert haben, dennoch haben sie vielen gescheitert geglaubten Ideen neuen Auftrieb gegeben und sie damit zum Erfolg geführt. In intensiven Diskussionen haben wir nicht nur das Visionäre vom Machbaren geschieden, sie haben auch mein Physikverständnis geschärft und viele neue Ideen geboren. Für diese vielen Diskussionen und vor allem für den freundschaftlichen Umgang miteinander bin ich sehr dankbar.

Mein Büro- und Laborgenosse Hanno Kaupp hat mich über viele Jahre durch alle Höhen und Tiefen der Doktorarbeit und des Lebens begleitet. Seine unerklärlich dauerhaft gute Laune hat mir die schweren Zeiten leicht und die guten besonders schön gemacht. Seine Liebe zum Deutschlandfunk hat mir im Labor viele spannende Diskussionen über Gott und die Welt beschert. Es war mir eine große Ehre, Büro und Labor mit Hanno geteilt zu haben.

Meine Kollegin Julia Benedikter und mein Kollege Thomas Hümmer haben mich über all die Jahre begleitet, sind mir mit Rat und Tat sowie guten Ideen zur Seite gestanden, haben mich ertragen und waren immer da, wenn ich sie brauchte.

Zum Ende dieser Arbeit ist Larissa Kohler zur Arbeitsgruppe gestoßen. Sie hat nie ihre gute Laune verloren und hat souverän ertragen, dass es für mich schwierig war, lieb gewonnene Projekte loszulassen. Mit großem Engagement führt sie nun das Wasserexperiment mit vielen neuen Ideen in Karlsruhe fort und ich bin froh, das Experiment bei ihr in guten Händen zu wissen.

Mit meinem Masteranden Benedikt Schlederer habe ich das CO_2 Laser Setup aufgebaut. Auch wenn manchmal zwei Sturköpfe aufeinander geprallt sind, so haben wir aus der dabei frei werdende Energie viele wegweisende Ideen entwickelt und es war eine Freude, Benedikt beim Bau des Experiments zu begleiten.

All den ehemaligen Mitarbeiterinnen und Mitarbeitern der AG Hunger, Postdocs, Masteranden und Bacheloranden danke ich für die gute Zusammenarbeit und die vielfältige Unterstützung. Jede und jeder von ihnen hat die Arbeitsgruppe auf ihre bzw. seine Art bereichert und hat mir eine spannende Zeit beschert.

Den (ehemaligen) Kolleginnen und Kollegen aus der Garchinger Abteilung danke ich für die große Hilfsbereitschaft und für die vielen Diskussionen über Physik und die Welt im Seminar, auf Ringberg oder bei Doktorfeiern.

Ohne die großartigen Nachbarn der Gruppe von Prof. Harald Weinfurter wäre es in der Schellingstraße recht einsam gewesen. Sie waren Nachbarn, wie man sie sich wünscht: hilfsbereit und immer für ein gutes Gespräch zu haben.

Wer neue Experimente machen will, braucht gelegentlich neuartiges Gerät. Ohne den Technikern der Abteilung, Charly Linner, Wolfgang Simon, Helmut Brückner, Toni Scheich und Nicole Schmidt wäre so manches mechanische, elektronische oder chemische Problem ungelöst und manches Experiment unmöglich geblieben. Für ihre großartige Unterstützung bin ich sehr dankbar.

Die Mechanische Werkstatt am Stammgelände hat unzählige Bauteile für die Experimente dieser Arbeit gefertigt, kleine und große, einfache und schwierige, Einzelstücke und Großserien. Dem Werkstatt-Team von Herrn Aust gilt hierfür großer Dank.

Forschung muss organisiert werden. Ohne der tatkräftigen Unterstützung von Ingrid Hermann und vor allem Gabriele Gschwendtner wäre manche Rechnung unbezahlt, mancher Arbeitsvertrag unverlängert und manche Reise unabgerechnet geblieben. Für diese großartige Hilfsbereitschaft und Unterstützung danke ich ganz besonders.

Ohne die Unterstützung meiner Familie, Freundinnen und Freunden wäre ich mit dieser Arbeit nicht bis zu dieser Stelle gekommen. Sie haben mir Mut gemacht, meinen Magen gepflegt und Fortschritte mit mir gefeiert.

Zu guter Letzt gilt ein ganz besonderer Dank meinen Eltern. Sie haben mich stets dabei begleitet und gefördert den Weg zu beschreiten, den ich für gut befunden habe und sie haben mir Neugierde und ein großes Interesse an der Welt, das ich als Wissenschaftler für unabdingbar halte, vorgelebt und mir auf den Weg mit gegeben.